



ALMA Observations of Molecular Complexity in the Large Magellanic Cloud: The N 105 Star-forming Region

Marta Sewilo^{1,2,3} , Martin Cordiner^{4,5} , Steven B. Charnley⁴ , Joana M. Oliveira⁶ , Emmanuel Garcia-Berrios^{4,5} , Peter Schilke⁷ , Jacob L. Ward⁸ , Jennifer Wiseman¹ , Remy Indebetouw^{9,10} , Kazuki Tokuda^{11,12,13} , Jacco Th. van Loon⁶ , Álvaro Sánchez-Monge⁷ , Veronica Allen¹⁴ , C.-H. Rosie Chen¹⁵ , Roya Hamedani Golshan⁷ , Agata Karska¹⁶ , Lars E. Kristensen¹⁷ , Stan E. Kurtz¹⁸ , Thomas Möller⁷ , Toshikazu Onishi¹¹ , and Sarolta Zahorecz^{11,12}

¹ Exoplanets and Stellar Astrophysics Laboratory, NASA Goddard Space Flight Center, Greenbelt, MD 20771, USA; marta.m.sewilo@nasa.gov

² Department of Astronomy, University of Maryland, College Park, MD 20742, USA

³ Center for Research and Exploration in Space Science and Technology, NASA Goddard Space Flight Center, Greenbelt, MD 20771, USA

⁴ Astrochemistry Laboratory, NASA Goddard Space Flight Center, Greenbelt, MD 20771, USA

⁵ Institute for Astrophysics and Computational Sciences, The Catholic University of America, Washington, DC 20064, USA

⁶ Lennard-Jones Laboratories, Keele University, ST5 5BG, UK

⁷ I. Physikalisches Institut der Universität zu Köln, Zùlpicher Str. 77, D-50937, Köln, Germany

⁸ Astronomisches Rechen-Institut, Zentrum für Astronomie der Universität Heidelberg, Mönchhofstr. 12-14, D-69120 Heidelberg, Germany

⁹ Department of Astronomy, University of Virginia, PO Box 400325, Charlottesville, VA 22904, USA

¹⁰ National Radio Astronomy Observatory, 520 Edgemont Rd, Charlottesville, VA 22903, USA

¹¹ Department of Physics, Graduate School of Science, Osaka Metropolitan University, 1-1 Gakuen-cho, Naka-ku, Sakai, Osaka 599-8531, Japan

¹² National Astronomical Observatory of Japan, National Institutes of Natural Science, 2-21-1 Osawa, Mitaka, Tokyo 181-8588, Japan

¹³ Department of Earth and Planetary Sciences, Faculty of Sciences, Kyushu University, Nishi-ku, Fukuoka 819-0395, Japan

¹⁴ Kapteyn Astronomical Institute, University of Groningen, P.O. Box 800, 9700 AV Groningen, The Netherlands

¹⁵ Max-Planck-Institut für Radioastronomie, Auf dem Hügel 69, D-53121 Bonn, Germany

¹⁶ Institute of Astronomy, Faculty of Physics, Astronomy and Informatics, Nicolaus Copernicus University, ul. Grudziądzka 5, 87-100 Toruń, Poland

¹⁷ Niels Bohr Institute, Centre for Star & Planet Formation, University of Copenhagen, Øster Voldgade 5-7, DK-1350 Copenhagen K, Denmark

¹⁸ Instituto de Radioastronomía y Astrofísica, Universidad Nacional Autónoma de México, Apdo. Postal 3-72, 58090 Morelia, Michoacán, Mexico

Received 2021 August 28; revised 2022 January 22; accepted 2022 January 23; published 2022 May 27

Abstract

The Large Magellanic Cloud (LMC) is the nearest laboratory for detailed studies on the formation and survival of complex organic molecules (COMs), including biologically important ones, in low-metallicity environments—typical of earlier cosmological epochs. We report the results of 1.2 mm continuum and molecular line observations of three fields in the star-forming region N 105 with the Atacama Large Millimeter/submillimeter Array. N 105 lies at the western edge of the LMC bar with ongoing star formation traced by H₂O, OH, and CH₃OH masers, ultracompact H II regions, and young stellar objects. Based on the spectral line modeling, we estimated rotational temperatures, column densities, and fractional molecular abundances for 12 1.2 mm continuum sources. We identified sources with a range of chemical makeups, including two bona fide hot cores and four hot core candidates. The CH₃OH emission is widespread and associated with all the continuum sources. COMs CH₃CN and CH₃OCH₃ are detected toward two hot cores in N 105 together with smaller molecules typically found in Galactic hot cores (e.g., SO₂, SO, and HNCO) with the molecular abundances roughly scaling with metallicity. We report a tentative detection of the astrobiologically relevant formamide molecule (NH₂CHO) toward one of the hot cores; if confirmed, this would be the first detection of NH₂CHO in an extragalactic subsolar metallicity environment. We suggest that metallicity inhomogeneities resulting from the tidal interactions between the LMC and the Small Magellanic Cloud might have led to the observed large variations in COM abundances in LMC hot cores.

Unified Astronomy Thesaurus concepts: [Star formation \(1569\)](#); [Astrochemistry \(75\)](#); [Magellanic Clouds \(990\)](#); [Chemical abundances \(224\)](#); [Star forming regions \(1565\)](#); [Protostars \(1302\)](#)

1. Introduction

The Large Magellanic Cloud (LMC), a gas-rich companion of the Milky Way, is the nearest laboratory for detailed studies on the formation and survival of complex organic molecules (COMs; ≥ 6 atoms including C; Herbst & van Dishoeck 2009), including those of astrobiological importance, in a low-metallicity environment ($Z_{\text{LMC}} \sim 0.3\text{--}0.5 Z_{\odot}$; Russell & Dopita 1992; Westerlund 1997; Rolleston et al. 2002). Both simple and complex molecules are present during each phase of

star and planet formation. Following their incorporation into comets, interstellar COMs might have been delivered to early Earth providing important ingredients for the origin of life (e.g., Ehrenfreund & Charnley 2000; Mumma & Charnley 2011; Caselli & Ceccarelli 2012). The metallicity of the LMC is similar to galaxies around the peak of star formation in the universe ($z \sim 1.5$; e.g., Pei et al. 1999; Mehlert et al. 2002; Madau & Dickinson 2014), making it an ideal template for studying star formation and complex chemistry in low-metallicity systems at earlier cosmological epochs where direct observations are impossible.

The LMC provides a unique opportunity to study the physics and chemistry of star formation in an environment that is profoundly different than that in the Galaxy. The elemental



Original content from this work may be used under the terms of the [Creative Commons Attribution 4.0 licence](#). Any further distribution of this work must maintain attribution to the author(s) and the title of the work, journal citation and DOI.

abundances of gaseous C, O, and N atoms and the dust-to-gas ratio are lower (e.g., Dufour 1975, 1984; Koornneef 1984; Roman-Duval et al. 2014), and the intensity of the UV radiation field is higher (10–100 times, but with large variations; e.g., Browning et al. 2003; Welty et al. 2006) when compared with the Galactic values. The deficiency of dust (and consequently less shielding) and strong UV radiation field lead to warmer dust temperatures in the LMC (e.g., van Loon et al. 2010). Gamma-ray observations indicate that the cosmic-ray density in the LMC is a factor of 4 lower than that measured in the solar neighborhood (e.g., Abdo et al. 2010a; Knödlseder 2013). All of these characteristics of the LMC’s environment may have direct consequences (with unclear relative importance) on the formation efficiency and survival of COMs. The formation of COMs requires dust surface chemistry on cold grains and cosmic-ray processing of grain mantles (e.g., Herbst & van Dishoeck 2009; Oberg 2016).

The LMC is sufficiently close (50.0 ± 1.1 kpc; Pietrzyński et al. 2013) to enable detailed studies on individual stars and protostars. The entire star-forming regions can be imaged relatively easily. Not plagued by distance ambiguities, line-of-sight confusion, and extinction that hamper Galactic studies, the LMC has been the subject of varied star formation studies (both photometric and spectroscopic) and has been surveyed at a wide wavelength range offering a rich context for interpreting new observations. The LMC has a history of interacting with both its neighbor—the Small Magellanic Cloud (SMC), another dwarf irregular galaxy with an even lower metallicity than the LMC ($Z_{\text{SMC}} \sim 0.1\text{--}0.2 Z_{\odot}$; Russell & Dopita 1992; Rolleston et al. 2002), and the Milky Way. The tidal interactions between the LMC and SMC influence the star formation history in each galaxy (e.g., Fujimoto & Noguchi 1990; Bekki & Chiba 2007a; Fukui et al. 2017; Tsuge et al. 2019).

1.1. Hot Molecular Cores in the LMC

Methanol (CH_3OH), methyl cyanide (CH_3CN), and larger COMs have been found in the LMC toward hot cores (Sewilo et al. 2018; Shimonishi et al. 2020): small ($D \lesssim 0.1$ pc), hot ($T_{\text{kin}} \gtrsim 100$ K), and dense ($n_{\text{H}} \gtrsim 10^{6\text{--}7} \text{ cm}^{-3}$) regions around forming massive stars where ice mantles have recently been removed from dust grains as a result of thermal evaporation and/or sputtering in shock waves (e.g., Garay & Lizano 1999; Kurtz et al. 2000; Cesaroni 2005; Palau et al. 2011). A typical Galactic hot core has a very rich spectrum at submillimeter wavelengths including lines from many complex organics—the products of interstellar grain-surface chemistry or postdesorption gas chemistry (e.g., Herbst & van Dishoeck 2009; Oberg 2016; Jørgensen et al. 2020). Methanol has also been detected toward a handful of other locations in the LMC but outside hot cores (“cold methanol”; see e.g., Sewilo et al. 2019).

Observational, theoretical, and laboratory studies indicate that COMs are mainly formed on dust grains through ice chemistry in the young stellar object’s (YSO’s) envelope, which has an inward temperature gradient due to heating from the central protostar (e.g., Herbst & van Dishoeck 2009; van Dishoeck 2014, 2018; Oberg 2016). During the YSO accretion phase, the composition of the icy grain mantles change as they approach the protostar and eventually sublime when the grains reach the inner hot core region in its immediate surroundings. (1) Initially, they only contain simple ices that are formed in the molecular cloud phase by a condensation of atoms and molecules from the gas phase and by subsequent

grain surface chemistry (e.g., H_2O , CH_4 , NH_3 , CO_2 , H_2CO , CH_3OH). First, the ices on the grain surface are formed through hydrogenation (adding H atoms that are the most mobile ice constituents at $T \sim 10$ K), and then also through chemical reactions involving CO. (2) When exposed to UV radiation (e.g., cosmic-ray interactions with H_2), simple ices can partially dissociate into radicals. (3) The radicals become mobile when the temperature increases with decreasing distance from the protostar, and they combine to form new species, including more complex molecules. (4) As the dust grain approaches the central protostar, the temperature becomes high enough for ice mantles to sublime ($T \sim 100\text{--}150$ K). The molecules released to the gas phase include simple ices from the original ice mantles, as well as newly formed complex organics. Gas-phase chemistry following ice sublimation can also contribute to the formation of some COMs (Taquet et al. 2016).

YSOs are also associated with jets and outflows at a range of velocities, which interact with the envelope and cloud material and produce shocks, enabling shock and hot-gas chemistry. Shocks can sublime or sputter icy grain mantles, releasing ice chemistry products (molecules such as CH_3OH and other COMs) into the gas (e.g., Arce et al. 2008). At high velocities, shocks can also sputter the grain cores, releasing the Si and S atoms and as a consequence, enhancing the production of Si- and S-bearing species such as SiO , SO_2 , and SO (e.g., Schilke et al. 1997; Gusdorf et al. 2008; van Dishoeck 2018 and references therein). In addition to jets and outflows, low-velocity shocks can be produced in YSOs at the envelope-disk interface where sublimation and sputtering of ices can occur (e.g., Aota et al. 2015; Miura et al. 2017). In summary, the formation of COMs is mainly a result of the chemical processes taking place in icy grain mantles in the protostellar envelope. The ice chemistry products (including COMs) become observable after icy grain mantles are sublimated close to the protostar or sublimated and sputtered in shocks in the jets/outflows or at the envelope-disk interface. Some COMs may be the result of the gas-phase chemistry following ice sublimation.

Prior to the present study, COMs with more than six atoms had only been detected toward two hot cores in the LMC: A1 and B3 in star-forming region N 113 (N 113 A1 and N 113 B3; Sewilo et al. 2018, 2019). Sewilo et al. (2018) reported the detection of methyl formate (HCOOCH_3) and dimethyl ether (CH_3OCH_3), together with their likely parent species CH_3OH , with fractional abundances with respect to H_2 (corrected for a reduced metallicity in the LMC with respect to the Milky Way) at the lower end, but within the range measured toward Galactic hot cores.

This was a surprising result, because the previous theoretical and observational studies indicated a deficiency of CH_3OH in the LMC (e.g., Acharyya & Herbst 2015; Nishimura et al. 2016; Shimonishi et al. 2016a, 2016b). For example, Shimonishi et al. (2016b) claimed a detection of a hot core toward the massive YSO ST11 in the LMC based on the derived physical conditions and the presence of simple molecules connected to the gas chemistry (e.g., SO_2), but no CH_3OH or other COMs were detected. They concluded that CH_3OH is depleted by 2–3 orders of magnitude as compared with Galactic hot cores. The underabundance of the CH_3OH ice and a low detection rate of CH_3OH masers were also reported in the LMC (e.g., Sinclair et al. 1992; Green et al. 2008; Shimonishi et al. 2016a).

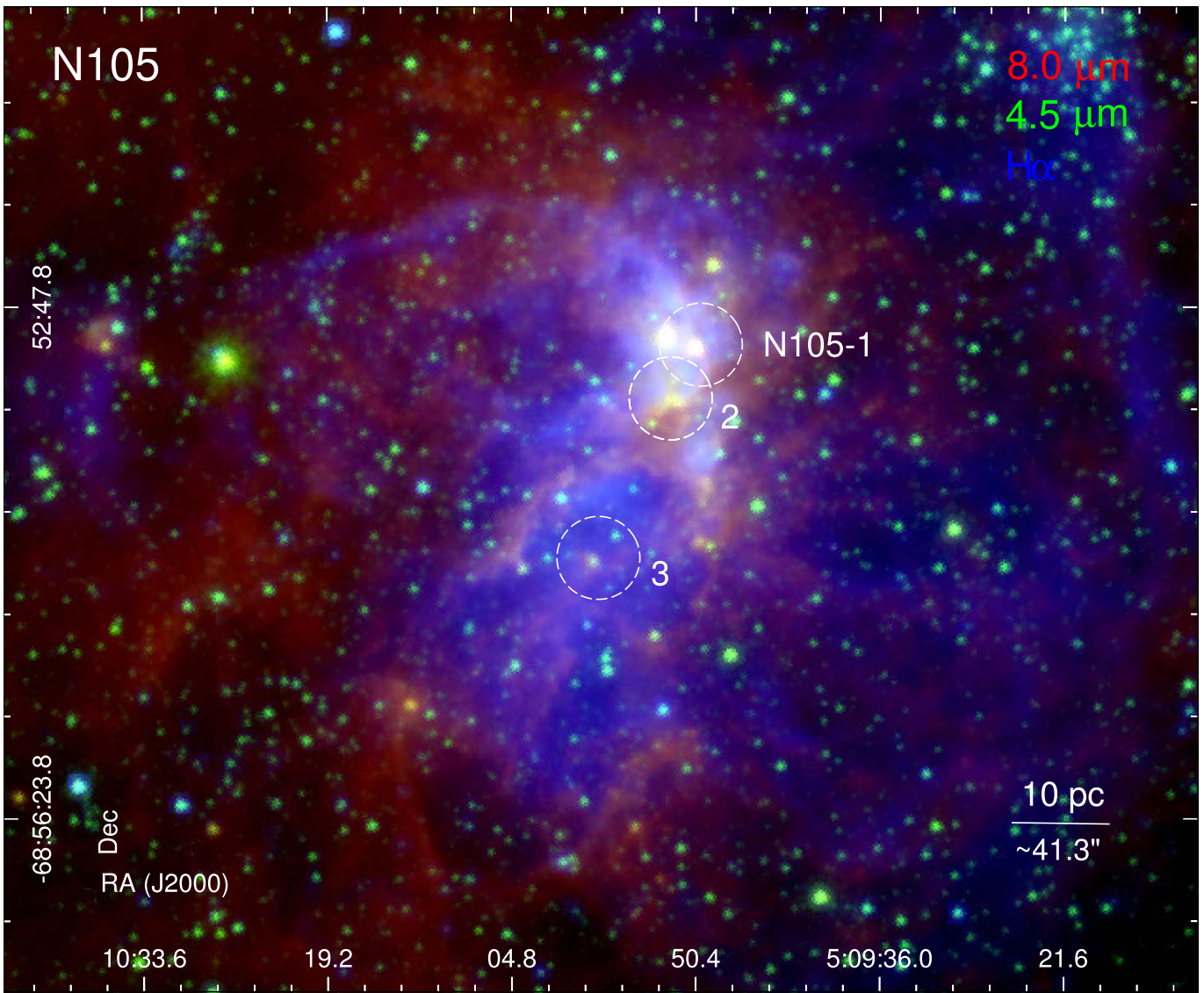


Figure 1. Three color-composite image of the N 105 star-forming region combining the SAGE/IRAC 8.0 μm (red), 4.5 μm (green; Meixner et al. 2006), and MCELS H α (blue; Smith & MCELS Team 1998) images. The ALMA fields are indicated with dashed circles and labeled.

The fact that molecules whose formation requires the hydrogenation of CO on grain surfaces were not detected (e.g., CH₃OH, HNCO) or were underabundant (e.g., H₂CO) in ST11 and that the CH₃OH ice is underabundant in the LMC YSOs led Shimonishi et al. (2016a) to propose a “warm ice chemistry” model in which the observed differences between the chemistry of the LMC and Galactic sources are a consequence of the dust being warmer in the LMC due to the strong interstellar radiation field. High dust temperatures in the LMC ($T \gtrsim 20$ K) suppress the hydrogenation of CO on grain surfaces due to the decrease in available hydrogen atoms, leading to inefficient production of CH₃OH. At the same time, the model also predicts an enhancement in CO₂ production due to the increased mobility of the parent species, which explains the increased CO₂/H₂O ice column density ratio observed toward LMC YSOs (e.g., Shimonishi et al. 2008; Oliveira et al. 2009, 2011); alternatively, this increased ratio can be explained by the underabundance of H₂O (e.g., Oliveira et al. 2011). The predictions of the warm ice chemistry model are consistent with astrochemical simulations for the appropriate elemental depletions (Acharyya & Herbst 2015, 2018;

Pauly & Garrod 2018). There is evidence that CH₃OH and other complex organics observed toward YSOs (hot cores and outflow shocks) might have formed in the cold (~ 10 K) molecular cloud phase preceding the onset of star formation (see discussion in Section 7.2).

A picture of a chemically diverse hot core population in the LMC has recently started emerging with the detection of hot core ST16 exhibiting CH₃OH and CH₃CN emission, but no larger COMs, and a general underabundance of organic species compared with Galactic hot cores (Shimonishi et al. 2020). Shimonishi et al. (2020) suggested that LMC hot cores can be divided into “organic-poor” and “organic-rich.” This classification, however, is based on only a handful of objects and needs verification.

If confirmed based on a larger sample of LMC hot cores, organic-rich hot cores would be those sources that are associated with larger COMs and have molecular abundances roughly scaled with metallicity (as in N 113 A1 and B3). In the organic-poor hot cores, the low abundances of organic molecules cannot be explained by the decreased abundance of C and O. No COMs (ST11) or only CH₃OH and CH₃CN

(ST16) are detected. In ST11 and ST16, H_2CO , CH_3OH , HNCO , CS , H_2CS , and SiO are significantly less abundant, while HCO^+ , SO , SO_2 , and NO are comparable with or more abundant than Galactic hot cores, after being corrected for metallicity. The organic-poor hot cores are unique to the low-metallicity environment of the LMC. Shimonishi et al. (2020) argue that a large chemical diversity of organic molecules seen in the LMC hot cores can be a consequence of the different grain temperature at the initial (ice-forming) stage of star formation. They support their conclusions with astrochemical simulations. The analysis of a larger sample of hot cores in the LMC is required to verify the hot core classification scheme suggested by Shimonishi et al. (2020) and get a better understanding of the complex chemistry in the metal-poor environment.

1.2. The N 105 Star-forming Region

In this paper, we report the results of our observations of three fields in star-forming region N 105 in the LMC with the Atacama Large Millimeter/submillimeter Array (ALMA), which include a detection of two hot cores that increase a previously known very small sample of four hot cores in the LMC. The LHA 120–N 105 (hereafter N 105, Henize 1956; or DEM L86, Davies et al. 1976) nebula is the star-forming region located at the western edge of the LMC bar (e.g., Ambrocio-Cruz et al. 1998). The $\text{H}\alpha$ image of N 105 reveals a bright central region (referred to in literature as N 105A) surrounded by a faint extended emission (see Figures 1 and 2). A sparse cluster NGC 1858 (e.g., Bica et al. 1996) with age estimates in a range 8–17 Myr (Vallenari et al. 1994; Alcaino & Liller 1986) and an associated OB association LH 31 (e.g., Lucke & Hodge 1970) are embedded within N 105A. LH 31 contains 18 OB stars and two Wolf–Rayet stars, and coincides with the strongest X-ray emission in the region (e.g., Vallenari et al. 1994; Dunne et al. 2001). Despite the presence of the OB association, the dense cloud N 105A shows little evidence for feedback from massive stars (e.g., Ambrocio-Cruz et al. 1998; Oliveira et al. 2006). The N 105 optical nebula is associated with the thermal radio continuum source MC 23 or B0510–6857 (e.g., McGee et al. 1972; Ellingsen et al. 1994; Filipovic et al. 1998).

Ongoing star formation in N 105A is traced by H_2O (e.g., Scalise & Braz 1982; Whiteoak et al. 1983; Lazendic et al. 2002; Oliveira et al. 2006; Ellingsen et al. 2010), OH (e.g., Haynes & Caswell 1981; Brooks & Whiteoak 1997), and CH_3OH masers (e.g., Green et al. 2008; Ellingsen et al. 2010), ultracompact (UC) H II regions (Indebetouw et al. 2004), and YSOs. About 40 YSOs have been identified based on the Spitzer Space Telescope (3.6–70 μm ; Carlson et al. 2012 and references therein) and the Herschel Space Observatory (100–500 μm ; Sewilo et al. 2010; Seale et al. 2014) data within the $\text{H}\alpha$ nebula. The Spitzer images shown in Figure 1 reveal a complex structure of the dust and polycyclic aromatic hydrocarbon (PAH) emission in N 105, with the brightest emission coinciding with the position of the most massive YSOs in N 105A.

Active star-forming sites in N 105 coincide with the position of the molecular cloud detected in single-dish observations of ^{12}CO and ^{13}CO (1–0), tracing gas densities of $\sim 10^2\text{--}10^3\text{ cm}^{-3}$ (e.g., Israel et al. 1993, HPBW $\sim 45''$ at 115 GHz; Chin et al. 1997, $45''$; Fukui et al. 1999 and Fukui et al. 2008, $2.6''$; Wong et al. 2011, $45''$ —see Figure 2). High-resolution ($\sim 6.7''$)

interferometric observations of HCN and HCO^+ (1–0) toward the peak of the CO emission with the Australia Telescope Compact Array (ATCA) revealed the densest gas in N 105 (Seale et al. 2012; see Figure 2). Two of the three fields we observed with ALMA are located in this region and are associated with H_2O and OH masers, while the third field covers a lower density region to the south and is associated with a CH_3OH maser.

The paper is organized as follows. In Section 2, we describe the observations and the archival data used in the paper. In Sections 3–5, we present the analysis of the 1.2 mm continuum and spectral line data. In Section 6, we investigate the physical characteristics of the observed fields and chemical properties of selected sources in the N 105 star-forming region based on the data ranging from the optical to radio wavelengths. The discussion is presented in Section 7, while in Section 8 we provide the summary and conclusions of our study.

2. The Data

The analysis presented in this paper is primarily based on the ALMA Cycle 7 Band 6 observations (Section 2.1). However, we also present the results of near-infrared (near-IR) spectroscopic observations with the Very Large Telescope/*K*-band Multi Object Spectrograph (VLT/KMOS) for three sources located in the ALMA Cycle 7 fields (Section 2.2).

2.1. Source Selection and ALMA Observations

We selected six fields in the LMC for Cycle 7 observations that have common characteristics with those hosting N 113 A1 and B3, at that time, the only known LMC hot cores with COMs: they are associated with massive Spitzer YSOs, $\text{H}_2\text{O}/\text{OH}$ masers, and SO emission, a well-known hot core and shock tracer (e.g., Chernin et al. 1994; Mookerjea et al. 2007). We also observed an additional field centered on a Stage 0/I protostar (e.g., Sewilo et al. 2010) associated with one of four 6.67 GHz and the only 12.2 GHz CH_3OH maser known in the LMC (Sinclair et al. 1992), making it a good hot core candidate. In total, seven fields were observed with the ALMA 12 m Array in Band 6 (with a single pointing each) as part of the Cycle 7 project 2019.1.01720.S (PI M. Sewilo).

The SO $3_2\text{--}2_1$ line emission toward N 113 A1 and B3 hot cores was serendipitously detected in our ALMA Cycle 3 observations (2015.1.01388.S, PI M. Sewilo; see also Sewilo et al. 2018). Enhanced SO emission can occur in hot cores following reactions $\text{S} + \text{OH}$ and $\text{O} + \text{SH}$ where the radicals and atoms are produced from the gas-phase destruction of H_2O and H_2S molecules evaporated/sputtered from ices (e.g., Charnley 1997).

A similar Band 3 correlator setup as for N 113 that covered the SO line was used in an unrelated project targeting massive YSOs in the LMC (2017.1.00093.S, PI T. Onishi), providing us with an opportunity to search for sources with a serendipitous SO detection. We have identified four Band 3 fields with SO detections and associated with masers (three with H_2O masers and one with an OH maser; e.g., Ellingsen et al. 2010; J. Ott 2022, private communication), resembling the A1 and B3 hot cores in N 113, which are also associated with masers. All the Band 3 fields were observed with the same setup, resulting in an ALMA synthesized beam of $\sim 2.13'' \times 1.57''$ and a channel width of 2.96 km s^{-1} . These observations also include the (1–0) transitions of ^{13}CO and

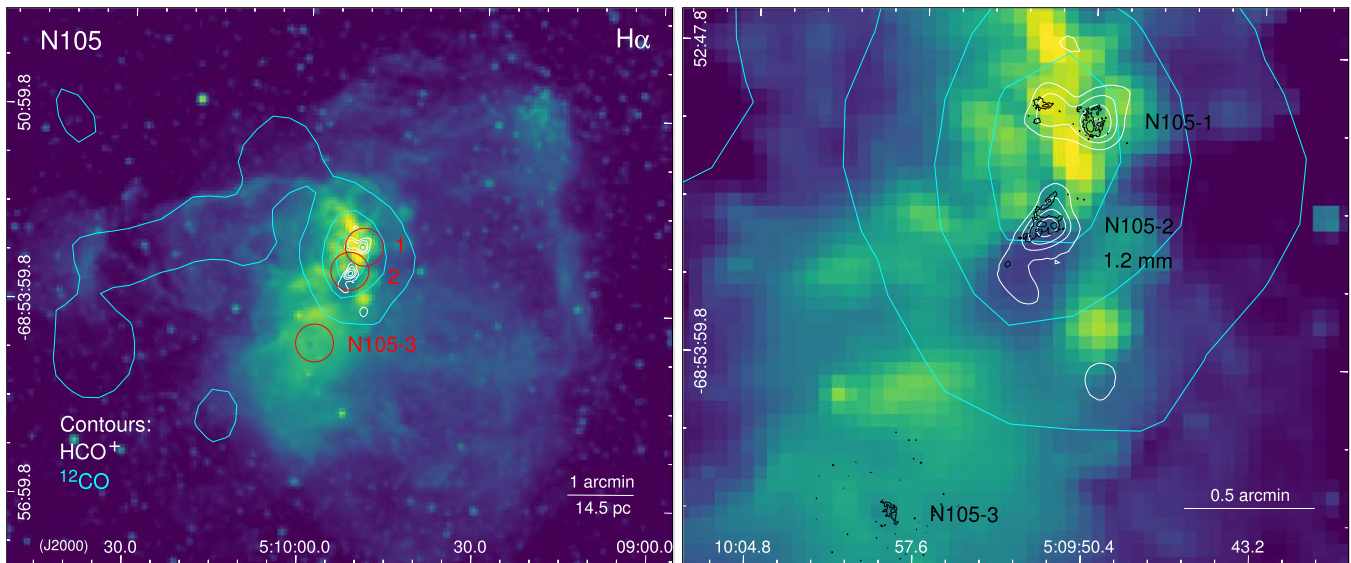


Figure 2. The MCELS $H\alpha$ image showing the N 105 optical nebula (left) and a zoom-in on the central region of N 105, referred to in literature as N 105A (right). In both images, the cyan contours correspond to the single-dish ^{12}CO ($J = 1 - 0$) emission from the Magellanic Mopra Assessment (MAGMA) survey with an effective angular resolution of $\sim 45''$, with contour levels of (20, 50, 80)% of the ^{12}CO integrated intensity peak of 17.3 K km s^{-1} (Mopra Telescope; Wong et al. 2011). The white contours correspond to the HCO^+ ($J = 1 - 0$) emission with contour levels of (10, 30, 50, 80)% of the HCO^+ integrated intensity peak of $4.1 \text{ Jy beam}^{-1} \text{ km s}^{-1}$ (ATCA synthesized beam of $6''3 \times 7''1$; Seale et al. 2012). The HCO^+ observations only covered the molecular cloud traced by the MAGMA survey, i.e., the N 105-3 field was not observed with ATCA. The three ALMA fields are indicated in red in the left panel, while the ALMA 1.2 mm continuum emission contours are shown in black in the right panel (see Figures 3).

C^{18}O , CS (2–1), and the 3 mm continuum; all four Cycle 5 Band 3 fields are associated with dense gas tracers (C^{18}O and CS). Six out of seven fields included in our Cycle 7 Band 6 observations are centered on regions with SO emission and $\text{H}_2\text{O}/\text{OH}$ masers within these four Cycle 5 Band 3 fields and thus are most likely to host hot cores.

Here, we present the results for three fields observed in Cycle 7, all located in the N 105 star-forming region. Two of the fields are associated with SO emission and $\text{H}_2\text{O}/\text{OH}$ masers; we have dubbed them “N 105–1” and “N 105–2”. The third field is associated with methanol masers, and we will refer to it as “N 105–3”; no prior ALMA observations are available for N 105–3. All three ALMA fields in N 105 hosting hot core candidates are shown in Figure 1, and their positions are listed in Table 2.

The observations of all fields were executed twice on 2019 October 21 with 43 antennas and baselines from 15 to 783 m. The (bandpass, flux, phase) calibrators were (J0519–4546, J0519–4546, J0440–6952) and (J0538–4405, J0538–4405, J0511–6806) for the first and second run, respectively. The targets were observed again on 2019 October 23, with 43 antennas and baselines from 15 to 782 m. The calibrators were the same as for the first run on October 21. The total on-source integration time for all seven fields was 91.8 minutes. for all three executions. The maximum recoverable scale calculated from the 5th percentile baseline length for the final data set combining all executions varied between $5''6$ and $5''2$ for a sky frequency range covered by our observations (~ 241.3 – 260.4 GHz). The spectral setup included four 1875 MHz spectral windows centered on frequencies of 242.4, 244.8, 257.85, and 259.7 GHz, each with 3840 channels, providing a spectral resolution of 1.21 – 1.13 km s^{-1} . Henceforth, we will refer to the spectral windows as the “242 GHz/245 GHz/258 GHz/260 GHz spectral window.”

The data were calibrated and imaged with version 5.6.1–8 of the ALMA pipeline in Common Astronomy Software

Applications (CASA; McMullin et al. 2007). The continuum in each spectral window was identified and subtracted before cube imaging. The CASA task `tclean` was used for imaging using the Hogbom deconvolver, standard gridded, Briggs weighting with a robust parameter of 0.5, and masking using the “auto-multithresh” algorithm. The spectral cubes have a cell size of $0''.092 \times 0''.092 \times 0.56 \text{ km s}^{-1}$. Additional information on the data cubes is included in Table 1. The 242.4 GHz (1.2 mm) continuum image parameters are listed in Table 2. All the images have been corrected for primary beam attenuation.

2.2. VLT/KMOS Near-IR Spectroscopy

Three near-IR sources in the ALMA Cycle 7 fields in N 105 were observed with the VLT/KMOS (Sharples et al. 2013) as part of a survey of YSO candidates under program 0101.C-0856(A) (PI J. L. Ward) using the $H + K$ grating with a spectral resolving power of 2000 and a spatial pixel scale of $0''.2$. The observations took place on the night of 2018 August 28–29, with seeing ranging from $0''.55$ to $1''.66$. The measured FWHM of one of the sources in N 105 (ID 558354728325) in the K band is 8.2 pixels, corresponding to approximately $1''.6$. KMOS is able to perform integral field spectroscopy in the near-IR bands for 24 targets simultaneously using 24 configurable arms. The KMOS observations were carried out using a standard nod-to-sky procedure with an integration time of 150 s, four detector integration times (DITs) and three dither positions, yielding a total on-source integration time of 1800 s. Telluric absorption correction, response curve correction, and absolute flux calibration were carried out using observations of telluric standard stars using three integral-field units (IFUs). The data were reduced with the standard VLT/KMOS pipeline using the ESOREFLEX data reduction package (Davies et al. 2013).

The K -band continuum image is produced by integrating over a third-order polynomial fit to the data for every spatial

Table 1
Spectral Cube Parameters

Field	R.A. (^h ^m ^s)	Decl. ([°] ['] ["])	Spectral Window	Frequency Range (GHz)	Synth. Beam: (Θ_B , PA) (["] × ["] , deg)	Data Cube rms ^a	
						(mJy beam ⁻¹)	(K)
N 105–1	05:09:50.47	–68:53:04.9	242 GHz	241.27653–243.14971	0.538 × 0.497, 36.8	1.97	0.15
			245 GHz	243.66769–245.54088	0.533 × 0.492, 35.0	1.88	0.15
			258 GHz	256.71495–258.58814	0.511 × 0.470, 38.5	2.05	0.16
			260 GHz	258.54806–260.42125	0.506 × 0.467, 36.7	2.28	0.18
N 105–2	05:09:52.37	–68:53:26.6	242 GHz	241.27653–243.14971	0.539 × 0.497, 37.8	1.97	0.15
			245 GHz	243.66769–245.54088	0.534 × 0.492, 35.5	1.87	0.15
			258 GHz	256.71495–258.58814	0.510 × 0.471, 38.7	2.05	0.16
			260 GHz	258.54806–260.42125	0.507 × 0.467, 37.0	2.25	0.17
N 105–3	05:09:58.66	–68:54:34.1	242 GHz	241.27653–243.14971	0.540 × 0.496, 39.1	1.97	0.15
			245 GHz	243.66769–245.54088	0.534 × 0.492, 36.1	1.88	0.15
			258 GHz	256.71495–258.58814	0.510 × 0.471, 39.0	2.05	0.16
			260 GHz	258.54806–260.42125	0.507 × 0.467, 36.8	2.28	0.17

Note.

^a The rms noise per 0.56 km s⁻¹ channel estimated with the CASA task IMSTAT in line-free channels.

Table 2
ALMA Pointings and 242.4 GHz/1.2 mm continuum Image Parameters

Field	R.A. (^h ^m ^s)	Decl. ([°] ['] ["])	Synth. Beam: (Θ_B , PA) (["] × ["] , deg)	Image rms	
				(μ Jy beam ⁻¹)	(mK)
N 105–1	05:09:50.47	–68:53:04.9	0.506 × 0.471, 37.2	69	6.0
N 105–2	05:09:52.37	–68:53:26.6	0.510 × 0.473, 37.4	51	4.4
N 105–3	05:09:58.66	–68:54:34.1	0.507 × 0.470, 38.1	27	2.4

pixel (spaxel) over the spectral range 2.028–2.290 μ m. The Br γ and H $_2$ line emission images are produced by fitting a Gaussian profile to the emission lines at every position in the image. Each IFU has a square field of view of 2["]8 × 2["]8.

The measured KMOS *H*- and *K*-band fluxes are found to be significantly lower than those determined by the near-IR surveys covering this region, the Two Micron All Sky Survey (2MASS) *JHK_S*, and the Visible and Infrared Survey Telescope for Astronomy (VISTA) *YJK_S* survey of the Magellanic Clouds system (VMC; Cioni et al. 2011), on average by a factor of 24. Thus, the KMOS fluxes are not reliable enough to be used directly. Instead, for the subsequent analysis, we have scaled the extracted spectra so that the sum of the spectral region from 2.028–2.295 μ m is consistent with the *K*-band magnitude of the corresponding point source from the VMC survey catalog. The publicly available VMC catalog was queried using the VISTA Science Archive (VSA;¹⁹ Cross et al. 2012) to obtain aperture photometry in *YJK_S* (VMCDR4). For reference, N 105 is located in VMC tile LMC 6_4.

To improve astrometry of the KMOS images, we computed the cross-correlation functions for all the KMOS fields with the VMC survey and calculated the R.A. and decl. values that the KMOS data should be shifted by to match the VMC data. First, the KMOS *K*-band continuum images were flipped, rotated by 4.9918 degrees, and rescaled to match the orientation and pixel scale of the VMC data using the WCSTOOLS package. The CORREL_IMAGES function in IDL was then used to compute the 2D cross-correlation function between the KMOS and VMC images. The 2D Gaussian profiles were fitted to the cross-correlation functions giving the most probable offsets (the centroid position of the Gaussian) in the VMC survey

coordinate frame. Flipping and rotating the offsets between the KMOS and VMC images then converts them from the VMC coordinate system into R.A. and decl. There is still a small shift between the KMOS and VMC data; however, this shift is subpixel and thus not significant, and the association between the VMC and KMOS sources can be established reliably. The precision of the KMOS astrometry is limited by the relatively poor resolution of the KMOS data due to seeing. The results of the VLT/KMOS observations are discussed in Section 6.2.

3. 1.2 mm Continuum Emission and Source Identification

Figure 3 shows the 1.2 mm continuum images of N 105–1, N 105–2, and N 105–3. Each field contains multiple continuum components. We have assigned identification letters (A, B, C, etc.) to all the 1.2 mm continuum sources associated with the molecular or ionized gas emission peaks in order of decreasing continuum peak intensity. We will refer to individual sources by providing the field name followed by the letter indicating the source name within this field (e.g., N 105–2 A is referred to as 2 A). We have identified an additional continuum peak, which likely is a separate source, but it is blended with N 105–2 B in our images; we dubbed it 2 F. The continuum signal-to-noise ratio is larger than 10 for all but one source; 3 C is an 8 σ detection.

We have inspected the ATCA 4.8 GHz (6 cm; synthesized beam: 2["]19 × 1["]70) and 8.6 GHz (3 cm; 1["]82 × 1["]24) images of N 105 presented in Indebetouw et al. (2004) covering N 105–1 and N 105–2 to check if any of the ALMA 1.2 mm continuum sources in these fields are associated with the radio emission and thus might need a correction for a contribution from the free-free emission to the millimeter-wave continuum emission. Three of the four ATCA radio sources detected by Indebetouw et al. (2004) in N 105 are located in regions observed with ALMA (see Figure C3). B0510–6857 W, the

¹⁹ <http://horus.roe.ac.uk/vsa>

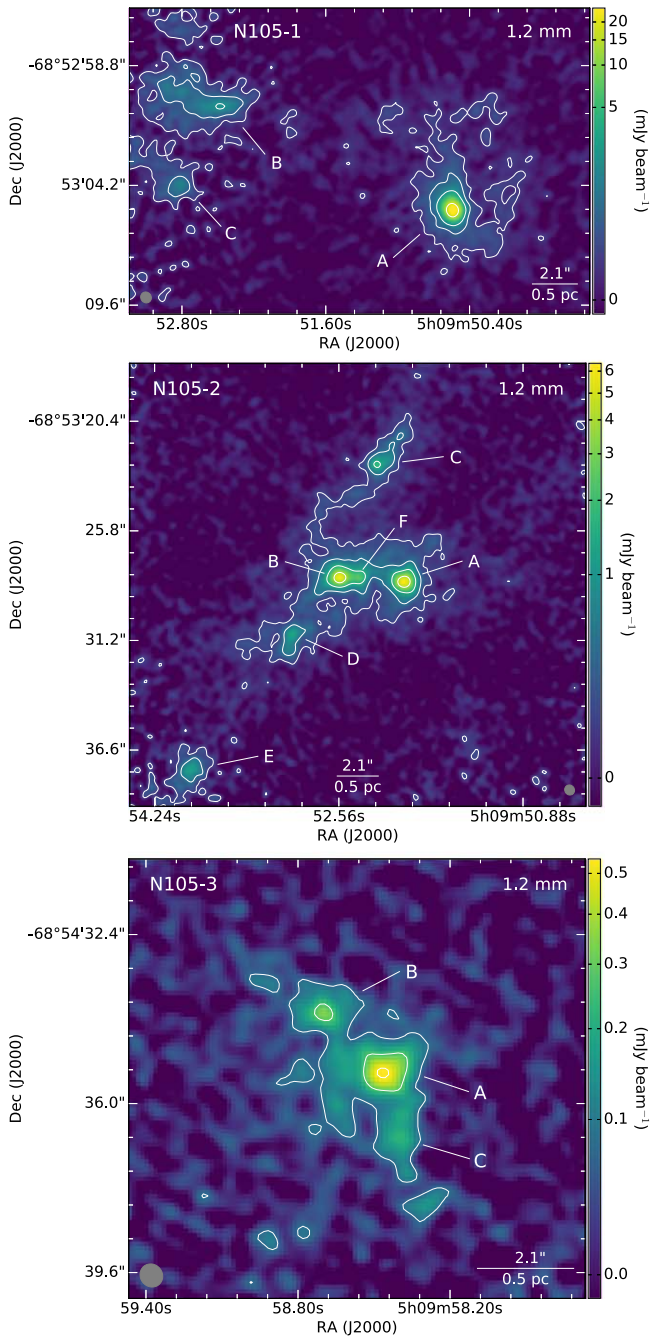


Figure 3. The 1.2 mm continuum images of N 105–1 (top), N 105–2 (center), and N 105–3 (bottom). The 1.2 mm continuum contour levels are $(3, 10, 30, 250) \times$ the image rms noise (σ) of 6.9×10^{-5} Jy beam $^{-1}$ for N 105–1, $(3, 10, 30, 80) \times 5.1 \times 10^{-5}$ Jy beam $^{-1}$ for N 105–2, and $(3, 10, 20) \times 2.7 \times 10^{-5}$ Jy beam $^{-1}$ for N 105–3. The 1.2 mm continuum sources identified in this paper are labeled. Sources N 105–1 B, N 105–1 C, and N 105–2 E are located at the edge of the corresponding beam field (the ALMA field of view). The size of the ALMA synthesized beam is shown in the lower left (top and bottom) or lower right (center) corner.

brightest radio source with 4.8 GHz/6 cm and 8.6 GHz/3 cm flux densities of 26 ± 1 mJy and 39 ± 1 mJy, respectively, corresponds to N 105–1 A (Indebetouw et al. 2004). The ATCA source B0510–6857 E lies just to the east of N 105–1 B, while B0510–6857 S is located between N 105–2 A, 2 B, and 2 C (see also Section 6).

N 105–1 A requires a correction for the contribution from the free–free emission to its Band 6 continuum emission. We

assume that the dust thermal emission and the free–free emission from ionized gas are the dominant sources of the 242.4 GHz continuum emission and estimate their relative contributions in two ways: by extrapolating the 4.8 and 8.6 GHz flux densities to higher frequencies and by analyzing the data from two millimeter-wave bands following the method described in Brunetti & Wilson (2019). We have estimated that $\sim 35\%$ of the 242.4 GHz continuum emission is free–free using the first method under the assumption that the free–free emission becomes optically thin at frequencies higher than 8.6 GHz. Flux densities were measured on the images with common beam and pixel sizes.

To estimate the relative contributions of the dust and free–free emission to the 242.4 GHz continuum emission using the method outlined in Brunetti & Wilson (2019), we have utilized the 111.5 GHz continuum image from the Cycle 5 project 2017.1.00093.S (see Section 2). The 111.5 GHz continuum image was made using the 12 m data only and has a synthesized beam and sensitivity of $2''.27 \times 1''.66$ and 2.7×10^{-4} Jy beam $^{-1}$, respectively. We have combined the 111.5 and 242.4 GHz flux densities using Equation (4) in Brunetti & Wilson (2019) assuming a dust opacity spectral index β of 1.7 for N 105 (Gordon et al. 2014; the mean value is calculated from pixels in the dust opacity spectral index map covering N 105, using the expectation values (“exp”) from the Broken Emissivity Law Model (BEMBB)) to estimate the dust-only flux density in Band 6. The resulting dust and free–free emission contributions to the 242.4 GHz continuum emission are $\sim 45\%$ and $\sim 55\%$, respectively. For $\beta = 1/\beta = 2$, the free–free contribution would be $\sim 54\%/\sim 56\%$.

The estimated contribution of the free–free to the 242.4 GHz continuum emission for 1 A ranges from $\sim 35\%$ to $\sim 55\%$. The lower value calculated by extrapolating the centimeter-wave flux densities to higher frequencies may be underestimated if the turnover frequency (the frequency where the free–free emission becomes optically thin) is higher than 8.6 GHz for N 105–1 A. N 105–1 A is likely at the early UC H II stage, if not at an earlier hypercompact (HC) H II region stage (e.g., Kurtz 2002, 2005; Sewilo et al. 2004), and has a rising spectrum from 4.8 to 8.6 GHz with a spectral index $\alpha = +0.6$ ($S_\nu \propto \nu^\alpha$, where S_ν is a flux density at a frequency ν). It would not be unexpected if its spectrum continues to rise to higher frequencies (Yang et al. 2019, 2021 and references therein). Considering these uncertainties, we assume that half of the continuum emission at 242.4 GHz is free–free. The correction is applied to the continuum data to calculate H₂ column densities and masses as described in Section 5.

While there is no radio emission peak coinciding with 1 B and 1 C, the ATCA images reveal the presence of the faint extended emission at the location of these sources, thus a small contamination of the 1.2 mm continuum emission with the free–free emission is possible.

No high-resolution centimeter-wave image covering N 105–3 is available; however, there is no indication of the presence of the significant ionized gas emission (no H recombination lines have been detected and similarly to N 105–2, the field lies in the H α -dark region). Therefore, we expect the 1.2 mm emission detected toward N 105–3 to be the thermal emission from dust.

3.1. Association with YSOs and Masers

Each of our ALMA fields contains high-mass YSO candidates identified based on the Spitzer 3.6–70 μm data from the LMC-wide Spitzer Surveying the Agents of Galaxy Evolution (SAGE; Meixner et al. 2006; SAGE Team 2006) survey (e.g., Whitney et al. 2008; Gruendl & Chu 2009; Carlson et al. 2012). Spitzer is mostly sensitive to Stage I YSOs with disks and envelopes and some more evolved Stage II YSOs with disks and remnant or no envelopes. Subsets of YSO candidates were followed up with near- to far-IR spectroscopic observations, which confirmed their nature and allowed for investigating their physical and chemical characteristics (e.g., Oliveira et al. 2009; Seale et al. 2009; Ward et al. 2016; Jones et al. 2017; and Oliveira et al. 2019).

Four out of six YSO candidates in the ALMA fields of view in N 105 were confirmed spectroscopically as bona fide YSOs by Seale et al. (2009) using the Spitzer Infrared Spectrograph (IRS) observations (5–37 μm). Two sources were classified as “Group P” and another two as “Group PE” YSOs. Both Group P and PE sources show strong PAH emission features. More evolved Group PE sources also show strong fine-structure lines such as [S IV] 10.5 μm , [Ne II] 12.8 μm , [Ne III] 15.5 μm , [S III] 18.7 μm and 33.5 μm , and [S III] 34.8 μm . The sources from both groups may show some absorption from silicates, particularly at 10 μm ; the silicate absorption features are difficult to identify unambiguously in the presence of strong PAH emission features at 6.2, 7.7, 8.6, and 11.3 μm . Group P and PE sources can also exhibit the CO₂ 15.2 μm ice absorption feature in the Spitzer/IRS spectra (Seale et al. 2011; see also Section 6.1).

Below we provide a more detailed discussion on YSO candidates, spectroscopically confirmed YSOs, and masers (H₂O, OH, CH₃OH) in individual ALMA fields in N 105.

N 105-1: N 105-1 hosts two spectroscopically confirmed YSOs from Seale et al. (2009): 050950.53–685305.5 (source #318 or SSTISAGE1C J050950.53–685305.4 from Whitney et al. 2008) and 050952.73–685300.7 (see Figure 4). Source 050950.53–685305.5 is associated with the bright 1.2 mm continuum source N 105-1 A, while 050952.73–685300.7 coincides with N 105-1 B and an extended emission to the east (see Section 6). YSO 050950.53–685305.5 was classified by Seale et al. (2009) as a Group P and 050952.73–685300.7 as a Group PE source.

No maser detection has been reported in literature toward N 105-1.

N 105-2: Three Spitzer YSO candidates from Gruendl & Chu (2009) are in the N 105-2 field (050952.26–685327.3, 050953.89–685336.7, and 050951.31–685335.6; Figure 4), two of which were spectroscopically confirmed as YSOs by Seale et al. (2009) and are associated with the 1.2 mm continuum emission. The YSO 050953.89–685336.7 (Group P source in Seale et al. 2009) coincides with N 105-2 E, while the Gruendl & Chu (2009)’s catalog position of 050952.26–685327.3 (Group PE) lies between the 2 A and 2 B continuum peaks. The inspection of the Spitzer images shows that no source in the image is visible at this position, but there are two Spitzer sources in the vicinity. The Spitzer Infrared Array Camera (IRAC) resolution is just about resolving these two sources corresponding to the 1.2 mm continuum peaks 2 A and 2 B, separated by only ~ 1.5 pixels. It is likely that the

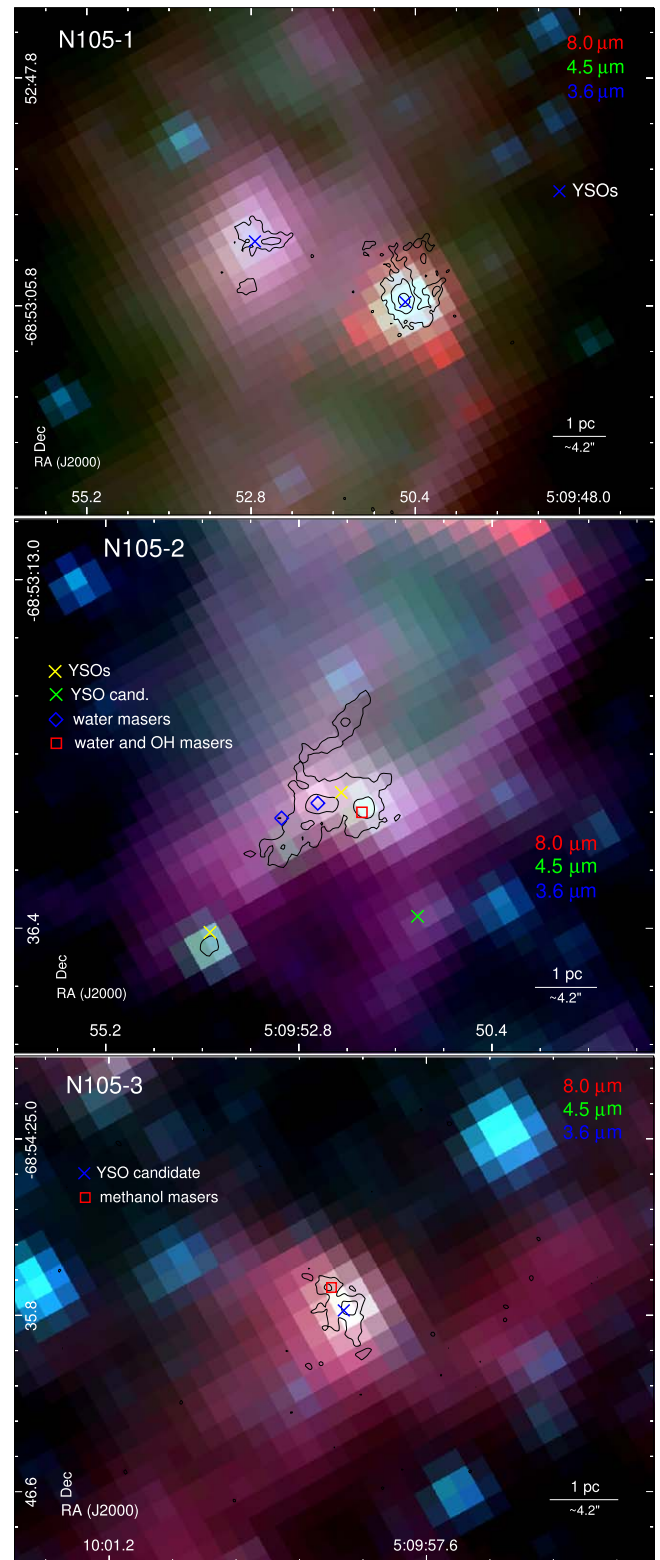


Figure 4. Three-color mosaic of N 105-1 (top), N 105-2 (center), and N 105-3 (bottom) combining the Spitzer/SAGE IRAC 8.0 μm (red), 4.5 μm (green), and 3.6 μm (blue) images. The positions of YSOs, YSO candidates, and masers are marked as indicated in the legends. The 1.2 mm continuum contour levels correspond to $(3, 10, 100)\sigma_1$ for N 105-1, $(3, 20)\sigma_2$ for N 105-2, and $(3, 10)\sigma_3$ for N 105-3, where σ_1 , σ_2 , and σ_3 are rms noise levels in the corresponding 1.2 mm continuum images not corrected for the primary beam attenuation for clarity: $(6.8, 5.0, 2.5) \times 10^{-5}$ Jy beam⁻¹.

source-finding routine used by Gruendl & Chu (2009) found only 2 A (the brighter peak at $4.5 \mu\text{m}$) but not 2 B in the shorter IRAC bands, and only 2 B (the brighter peak at $8.0 \mu\text{m}$) but not 2 A in the longer IRAC bands. The sources are close enough to be identified as a single object during the band-merging process, resulting in a catalog photometry and position (a weighted mean of the positions found in individual bands) being a combination of these two sources. The catalog position roughly in between the two Spitzer sources supports this interpretation. The Spitzer/IRS spectrum of 050952.26–685327.3 analyzed by Seale et al. (2009) most likely includes contributions from both nearby sources as well. The SAGE IRAC point-source catalog does not include any sources in the central part of the ALMA field.

No 1.2 mm continuum emission has been detected toward the position of the YSO candidate 050951.31–685335.6 in N 105–2 located to the southwest from 2 A and 2 B (Figure 4).

Two sources in N 105–2 are associated with masers. N 105–2 A and 2 B coincide with the 22 GHz H_2O masers (Whiteoak et al. 1983; Whiteoak & Gardner 1986; Lazendic et al. 2002; Ellingsen et al. 2010; J. Ott 2022, private communication; see also Schwarz et al. 2012). Source 2 A is also associated with the 1665/1667 MHz OH maser (Haynes & Caswell 1981; Gardner & Whiteoak 1985; Brooks & Whiteoak 1997). No methanol masers have been detected toward N 105–2 (Green et al. 2008 and Ellingsen et al. 2010).

The maser positions used for investigating correlations with the ALMA and infrared emission (e.g., in Figure 4) come from Green et al. (2008) who summarize previous observations of different types of masers and provide accurate positions (within subarcsecond) obtained using the interferometric observations with ATCA.

One H_2O maser spot in N 105–2 detected with ATCA is offset toward the southeast from the 1.2 mm continuum source 2 B (J. Ott 2022, private communication; Schwarz et al. 2012; see e.g., Figure 4). Imai et al. (2013) reported a detection of another H_2O maser spot at a distance of $\sim 3''/4$ from the N 105–2 B 1.2 mm continuum peak toward north–northeast. However, they incorrectly associate this source with that reported in Oliveira et al. (2006) who was not able to estimate an accurate position of the maser spot based on their Parkes 64-m telescope observations, but argued that it is likely related to the maser detected by Lazendic et al. (2002); the accurate position of the H_2O maser provided by Lazendic et al. (2002) indicates that the maser emission originates in the vicinity of N 105–2 A. Due to this positional uncertainty, we do not show the position of the H_2O maser from Imai et al. (2013), which is not reported in other surveys, in the images.

N 105–3: One Spitzer YSO candidate lies within the N 105–3 field (050958.52–685435.5, Gruendl & Chu 2009; Carlson et al. 2012; see Figure 4), with the Spitzer catalog position corresponding to the 1.2 mm continuum peak of source N 105–3 A. No follow-up spectroscopic observations exist for 050958.52–685435.5.

In N 105–3, the 1.2 mm continuum source 3 B is associated with CH_3OH masers: 6.7 and 12.2 GHz (Green et al. 2008; Ellingsen et al. 2010). No H_2O masers have been detected toward this field (e.g., Ellingsen et al. 2010).

Three of the YSOs in N 105 have been well fit with the Robitaille et al. (2006) YSO radiation transfer models by Carlson et al. (2012): 050950.53–685305.5 (source SSTISAGEMAJ050950.53–685305.4 in Carlson et al. 2012; 1 A),

050953.89–685336.7 (SSTISAGEMA J050953.91–685337.1; 2 E), and 050958.52–685435.5 (SSTISAGEMA J050958.52–685435.2; 3 A). All sources were found to be massive with stellar masses and luminosities for the best-fit YSO models of $(31.3 \pm 2.6, 23.0 \pm 3.2, 17.9 \pm 1.4) M_\odot$ and $(14 \pm 2, 6.6 \pm 2.2, 3.6 \pm 0.5) \times 10^4 L_\odot$ for (050950.53–685305.5, 050953.89–685336.7, 050958.52–685435.5).

4. Spectral Line Analysis

For sources 1 A–C, 2 A–E, and 3 A–B, spectra were extracted as the mean within the area enclosed by the contour corresponding to the 50% of the source’s 1.2 mm continuum emission peak intensity. As a result, for these sources, the physical parameters determined based on spectral modeling provide averages over these spectral extraction areas, which are listed in Table 4 (see Section 4.3 for a discussion on spectral modeling). This spectral extraction method could not be applied to sources 2 F and 3 C, which are faint and associated with an extended continuum emission; the 50% of the 1.2 mm continuum peak intensity contour encloses other, brighter sources in N 105–2 and N 105–3. For 2 F and 3 C, we derive physical parameters at the peak of the continuum emission. Spectra of the chemically richest source 2 A, are shown in Figures 5 and 6 as examples. Spectra for all the sources are presented in Appendix B.

A selection of the spectral extraction method based on a larger area rather than a single pixel associated with a continuum peak was motivated by the fact that the peaks of the molecular line emission are not always coincident with the continuum peaks (see a discussion in Section 4.2). Moreover, the resulting spectra are less noisy than the single-pixel spectra.

4.1. Line Identification

The initial spectral line identification was carried out in the CASA task `viewer`, which uses the NRAO’s spectral line database `Splatalogue`.²⁰ The line identification was later verified by comparing the spectra to the predictions of models for the subset of molecules detected in Galactic hot cores, assuming local thermodynamic equilibrium (LTE) conditions. All the detectable lines predicted by the spectral model in the observed frequency ranges must be present in the observed spectrum with relative intensities for different transitions approximately consistent with the model predictions. The spectral analysis and modeling results are described in detail in Section 4.3. In our analysis, we use molecular data from the Cologne Database for Molecular Spectroscopy (CDMS²¹; Müller et al. 2005) where available; otherwise, we use the Jet Propulsion Laboratory (JPL) Millimeter and Submillimeter Spectral Line Catalog²² (Pickett et al. 1998; see Section 4.3 for details). We use the CDMS quantum number notation from the `Splatalogue` throughout the paper.

Table 3 lists all the molecular lines detected toward the continuum sources in N 105. We detected S-bearing species: SO , ^{33}SO , SO_2 , $^{34}\text{SO}_2$, CS , C^{33}S , OCS , H_2CS ; N-bearing species: HNCO , HC_3N , HC^{15}N , H^{13}CN ; three deuterated molecules: HDO , HDCO , and HDS ; as well as SiO , H^{13}CO^+ , and CH_2CO .

²⁰ <http://www.cv.nrao.edu/php/splat>

²¹ <http://www.astro.uni-koeln.de/cdms>

²² <http://spec.jpl.nasa.gov/>

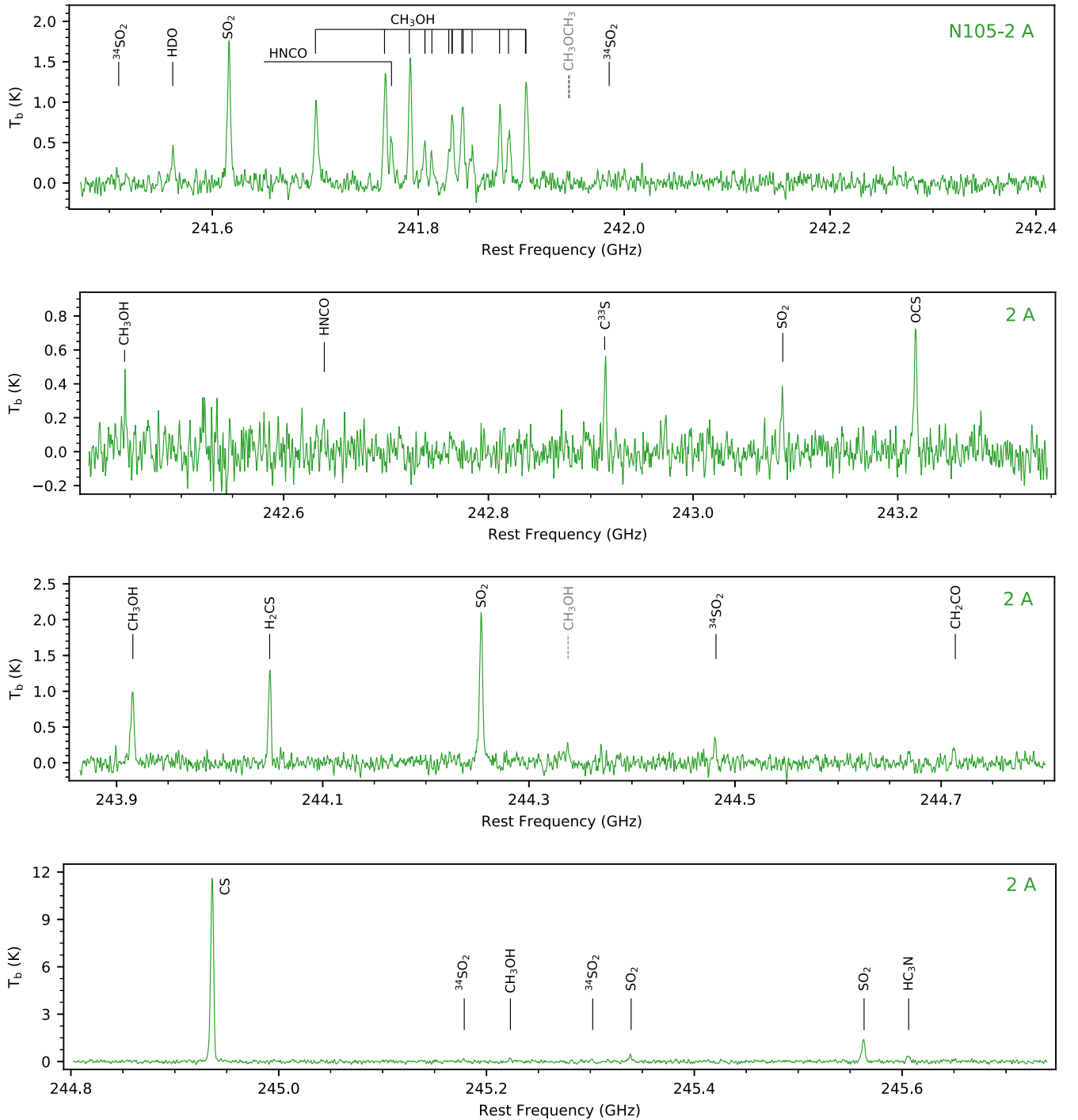


Figure 5. ALMA Band 6 spectra of the most chemically rich source detected in N 105 (N 105–2 A) in the ~ 242 GHz (top two panels) and ~ 245 GHz (bottom two panels) spectral windows. Reliable and tentative detections are indicated and labeled in black and gray, respectively. The spectra were extracted as the mean over the area enclosed by the 50% of the 1.2 mm continuum peak contour. The ~ 242 and ~ 245 GHz spectra of 2 A with the model spectra overlaid are shown in Figure B2 in Appendix B.

We detected COMs CH_3OH , CH_3CN , and CH_3OCH_3 in N 105. All three COMs are observed toward sources 2 A and 2 B. CH_3CN is also detected toward 2 C. CH_3OH is identified in the spectra of all the continuum sources, making it the most widespread COM in our observations.

We also report a tentative detection of formamide (NH_2CHO) toward N 105–2 A. We detected a single NH_2CHO transition (260.19198200 GHz): this is a $\sim 3.2\sigma$ detection of the brightest NH_2CHO transition within the

frequency range covered by our ALMA observations. The NH_2CHO line is blended with a ketene (CH_2CO) line (260.19198200 GHz); the lines are separated by ~ 2.13 MHz, which corresponds to ~ 2.45 km s $^{-1}$ or 2.19 channel widths. The significance of this detection in the low-metallicity environment is discussed in Section 7.4.

Extragalactic detection of deuterated species were first reported in the LMC star-forming regions by Chin et al. (1996) who detected DCO^+ toward three (N 113, N 44 BC,

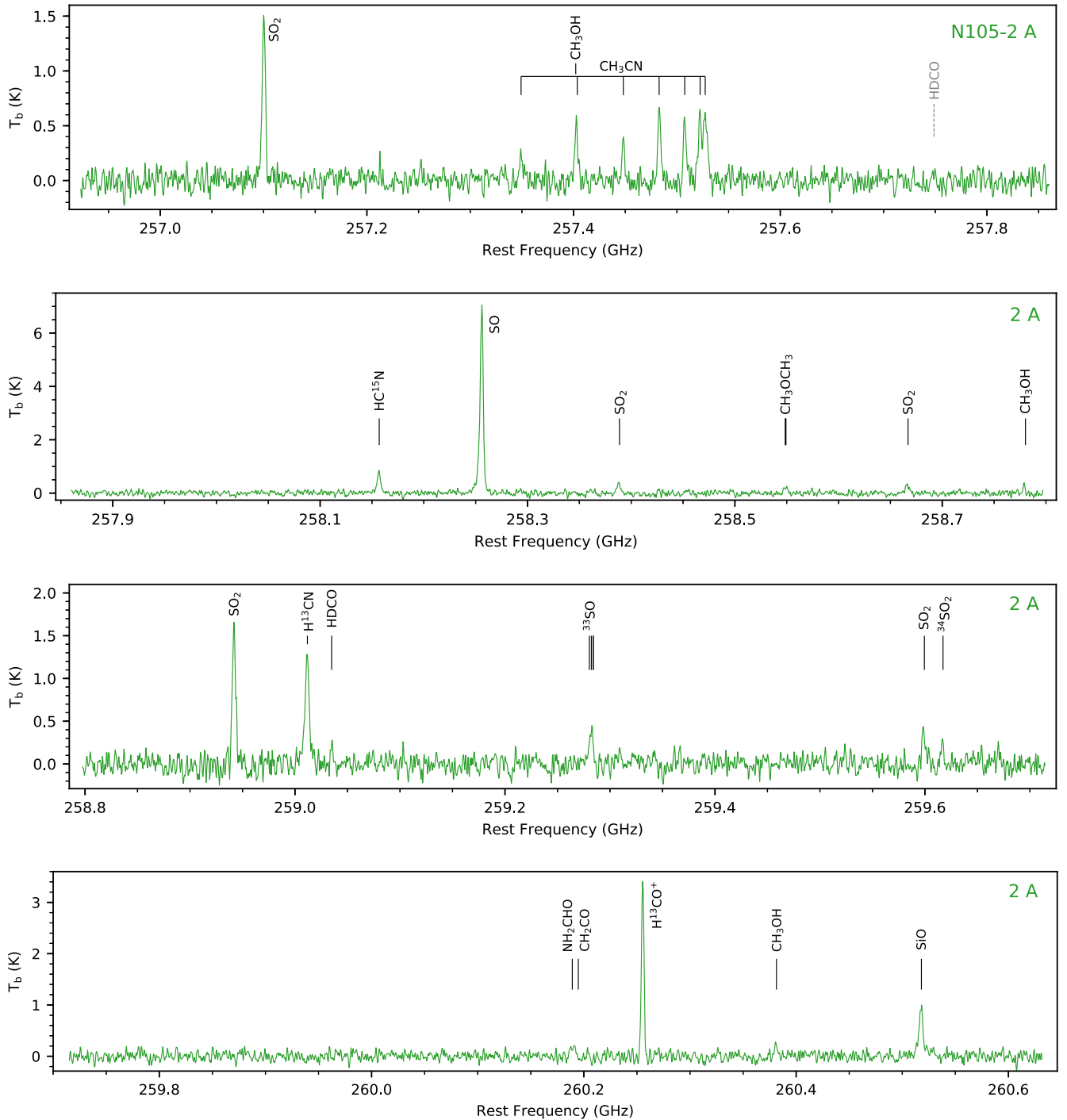


Figure 6. ALMA Band 6 spectra of the most chemically rich source detected in N 105 (N 105–2 A) in the ~ 258 GHz (top two panels) and ~ 260 GHz (bottom two panels) spectral windows. Reliable and tentative detections are indicated and labeled in black and gray, respectively. The spectra were extracted as the mean over the area enclosed by the 50% of the 1.2 mm continuum peak contour. The ~ 258 GHz and ~ 260 GHz spectra of 2 A with the model spectra overlaid are shown in Figure B3 in Appendix B.

N 159 HW) and DCN toward one star-forming region (N 113; see also Heikkilä et al. 1997 for N 159, and Sewilo et al. 2018 and Wang et al. 2009 for N 113). Martín et al. (2006) reported a tentative detection of DNC and N_2D^+ in the nucleus of the starburst galaxy NGC 253. Most recently, Muller et al. (2020) reported the detection of ND, NH_2D , and HDO with ALMA at redshift $z = 0.89$ in the spiral galaxy intercepting the line of sight to quasar PKS 1830–211. We detected deuterated

formaldehyde (HDCO), deuterated hydrogen sulfide (HDS), and deuterated water (HDO) toward hot cores 2 A (HDCO and HDO) and 2 B (HDO), and a hot core candidate 2 C (HDS). These are the first extragalactic detections of HDCO and HDS, and the first detection of HDO in an extragalactic star-forming region. A detailed discussion on the detection of HDO in the LMC will be included in a separate paper. Our observations did not cover any H_2CO , H_2O , or H_2S transitions, preventing us

Table 3
Spectral Lines Detected toward Continuum Sources in N 105–1, N 105–2, and N 105–3^a

Species	Transition	Frequency (MHz)	E_U (K)	1 A	1 B	1 C	2 A	2 B	2 C	2 D	2 E	2 F	3 A	3 B	3 C
COMs															
CH ₃ OH	5 _{-0,5} -4 _{-0,4} E, $v_t = 0$	241,700.159	47.94	✓?	✓	✓?	✓	✓	✓	✓	✓?	✓	✓?	✓?	✓?
CH ₃ OH	5 _{1,5} -4 _{1,4} E, $v_t = 0$	241,767.234	40.39	✓	✓	✓	✓	✓	✓	✓	✓	✓	✓	✓	✓
CH ₃ OH	5 _{0,5} -4 _{0,4} A, $v_t = 0$	241,791.352	34.82	✓	✓	✓	✓	✓	✓	✓	✓	✓	✓	✓	✓
CH ₃ OH	5 _{4,2} -4 _{4,1} A, $v_t = 0$	241,806.524	115.17	–	–	–	✓	✓	✓?	–	–	✓?	–	✓?	–
CH ₃ OH	5 _{4,1} -4 _{4,0} A, $v_t = 0$	241,806.525	115.17	–	–	–	✓	✓	✓?	–	–	✓?	–	✓?	–
CH ₃ OH	5 _{4,2} -4 _{4,1} E, $v_t = 0$	241,813.255	122.73	–	–	–	✓	✓	✓?	–	–	✓?	–	✓?	–
CH ₃ OH	5 _{-4,1} -4 _{-4,0} E, $v_t = 0$	241,829.629	130.82	–	–	–	✓	✓	✓	–	–	–	–	✓?	–
CH ₃ OH	5 _{3,3} -4 _{3,2} A, $v_t = 0$	241,832.718	84.62	–	–	–	✓	✓	✓	✓?	–	✓?	–	✓?	–
CH ₃ OH	5 _{3,2} -4 _{3,1} A, $v_t = 0$	241,833.106	84.62	–	✓	–	✓	✓	✓	✓?	–	✓?	–	✓?	–
CH ₃ OH	5 _{2,4} -4 _{2,3} A, $v_t = 0$	241,842.284	72.53	–	✓	✓?	✓	✓	✓	✓	–	✓?	–	✓?	–
CH ₃ OH	5 _{-3,3} -4 _{-3,2} E, $v_t = 0$	241,843.604	82.53	–	–	–	✓	✓	✓	✓	–	✓?	–	✓?	–
CH ₃ OH	5 _{3,2} -4 _{3,1} E, $v_t = 0$	241,852.299	97.53	–	–	–	✓	✓	–	–	–	✓?	–	✓?	–
CH ₃ OH	5 _{-1,4} -4 _{-1,3} E, $v_t = 0$	241,879.025	55.87	✓?	✓	✓?	✓	✓	✓	✓	✓?	✓	✓?	✓?	–
CH ₃ OH	5 _{2,3} -4 _{2,2} A, $v_t = 0$	241,887.674	72.54	–	–	–	✓	✓	✓	✓?	–	–	–	✓?	–
CH ₃ OH	5 _{2,3} -4 _{2,2} E, $v_t = 0$	241,904.147	60.73	✓?	✓	✓	✓	✓	✓	✓?	✓?	✓	–	✓?	–
CH ₃ OH	5 _{-2,4} -4 _{-2,3} E, $v_t = 0$	241,904.643	57.07	✓?	✓	✓	✓	✓	✓	✓	✓?	✓	–	✓?	–
CH ₃ OH	14 _{1,14} -13 _{2,11} E, $v_t = 0$	242,446.084	248.94	–	–	–	✓	✓?	–	–	–	–	–	–	–
CH ₃ OH	5 _{1,4} -4 _{1,3} A, $v_t = 0$	243,915.788	49.66	–	✓	–	✓	✓	✓	✓	–	✓	–	–	–
CH ₃ OH	22 _{3,19} -22 _{2,20} A, $v_t = 0$	244,330.372	636.78	✓?	–	–	–	–	–	–	–	–	–	–	–
CH ₃ OH	9 _{-1,9} -8 _{-0,8} E, $v_t = 1$	244,337.983	395.66	✓?	–	–	–	✓?	–	–	–	–	–	–	–
CH ₃ OH	21 _{3,18} -21 _{2,19} A, $v_t = 0$	245,223.019	585.76	–	–	–	✓	–	–	–	–	–	–	–	–
CH ₃ OH	18 _{3,16} -18 _{2,17} A, $v_t = 0$	257,402.086	446.55	–	–	–	✓	✓?	–	–	–	–	–	–	–
CH ₃ OH	19 _{3,17} -19 _{2,18} A, $v_t = 0$	258,780.248	490.58	–	–	–	✓	–	–	–	–	–	–	–	–
CH ₃ OH	20 _{3,18} -20 _{2,19} A, $v_t = 0$	260,381.463	536.97	–	–	–	✓	–	–	–	–	–	–	–	–
CH ₃ OCH ₃	13 _{1,13} -12 _{0,12} EA	241,946.249	81.13	–	–	–	✓?	–	–	–	–	–	–	–	–
CH ₃ OCH ₃	13 _{1,13} -12 _{0,12} AE	241,946.249	81.13	–	–	–	✓?	–	–	–	–	–	–	–	–
CH ₃ OCH ₃	13 _{1,13} -12 _{0,12} EE	241,946.542	81.13	–	–	–	✓?	–	–	–	–	–	–	–	–
CH ₃ OCH ₃	13 _{1,13} -12 _{0,12} AA	241,946.835	81.13	–	–	–	✓?	–	–	–	–	–	–	–	–
CH ₃ OCH ₃	14 _{1,14} -13 _{0,13} EA	258,548.819	93.33	–	–	–	✓	✓	–	–	–	–	–	–	–
CH ₃ OCH ₃	14 _{1,14} -13 _{0,13} AE	258,548.819	93.33	–	–	–	✓	✓	–	–	–	–	–	–	–
CH ₃ OCH ₃	14 _{1,14} -13 _{0,13} EE	258,549.063	93.33	–	–	–	✓	✓	–	–	–	–	–	–	–
CH ₃ OCH ₃	14 _{1,14} -13 _{0,13} AA	258,549.308	93.33	–	–	–	✓	✓	–	–	–	–	–	–	–
CH ₃ CN	14 ₆ -13 ₆	257,349.180	349.73	–	–	–	✓	– ^c	–	–	–	–	–	–	–
CH ₃ CN	14 ₅ -13 ₅	257,403.585	271.23	–	–	–	✓	✓?	–	–	–	–	–	–	–
CH ₃ CN	14 ₄ -13 ₄	257,448.128	206.98	–	–	–	✓	✓?	–	–	–	–	–	–	–
CH ₃ CN	14 ₃ -13 ₃	257,482.792	156.99	–	–	–	✓	✓	–	–	–	–	–	–	–
CH ₃ CN	14 ₂ -13 ₂	257,507.562	121.28	–	–	–	✓	✓	✓?	–	–	–	–	–	–
CH ₃ CN	14 ₁ -13 ₁	257,522.428	99.85	–	–	–	✓	✓	✓?	–	–	–	–	–	–
CH ₃ CN	14 ₀ -13 ₀	257,527.384	92.71	–	–	–	✓	✓	✓	–	–	–	–	–	–
NH ₂ CHO	12 _{2,10} -11 _{2,9}	260,189.090	92.36	–	–	–	✓	–	–	–	–	–	–	–	–
Other Molecules															
HNCO	11 _{0,11} -10 _{0,10}	241,774.032	69.63	–	✓	–	✓	✓	✓	–	–	–	–	–	–
HNCO	11 _{1,10} -10 _{1,9}	242,639.705	113.15	–	–	–	✓	✓	–	–	–	–	–	–	–
HC ₃ N	27–26	245,606.320	165.04	–	–	–	✓	✓	–	–	–	–	–	–	–
HC ¹⁵ N	3–2	258,156.996	24.78	–	✓	✓	✓	✓	✓	–	–	✓?	–	–	–
H ¹³ CN	3–2	259,011.798	24.86	✓	✓	✓	✓	✓	✓	–	–	✓	–	–	–
H ¹³ CO ⁺	3–2	260,255.339	24.98	✓	✓	✓	✓	✓	✓	✓	✓	✓	✓	✓	✓?
CH ₂ CO	12 _{1,11} -11 _{1,10}	244,712.269	89.40	–	–	–	✓	–	–	–	–	–	–	–	–
CH ₂ CO	13 _{1,13} -12 _{1,12}	260,191.982	100.47	–	–	–	✓	–	–	–	–	–	–	–	–
SO ^{3Σ}	6 ₆ -5 ₅	258,255.826	56.50	✓	✓	✓	✓	✓	✓	✓	✓	✓	✓	✓	✓
OCS	20–19	243,218.036	122.58	–	–	–	✓	✓	✓	–	–	–	–	–	–
H ₂ CS	7 _{1,6} -6 _{1,5}	244,048.504	60.03	✓?	✓	✓	✓	✓	✓	✓	–	✓	–	–	–
CS	5–4	244,935.557	35.27	✓	✓	✓	✓	✓	✓	✓	✓	✓	✓	✓	✓
C ³³ S	5–4	242,913.610	34.98	–	✓	✓?	✓	✓	✓	✓	–	✓	–	–	–
SO ₂	5 _{2,4} -4 _{1,3}	241,615.797	23.59	✓?	✓	–	✓	✓	✓	–	–	✓	✓	–	–
SO ₂	5 _{4,2} -6 _{3,3}	243,087.647	53.07	–	–	–	✓	✓	–	–	–	–	–	–	–
SO ₂	26 _{8,18} -27 _{7,21}	243,245.435	479.58	–	–	–	–	✓	–	–	–	–	–	–	–
SO ₂ ^f	14 _{0,14} -13 _{1,13}	244,254.218	93.90	✓	✓?	–	✓	✓	✓	–	–	✓	–	–	–
SO ₂	26 _{3,23} -25 _{4,22}	245,339.233	350.79	–	–	–	✓	✓	–	–	–	–	–	–	–
SO ₂ ^f	10 _{3,7} -10 _{2,8}	245,563.422	72.72	✓	✓	–	✓	✓	✓?	–	–	–	✓	–	–
SO ₂	7 _{3,5} -7 _{2,6}	257,099.966	47.84	✓	✓?	–	✓	✓	✓	–	–	–	–	–	–

Table 3
(Continued)

Species	Transition	Frequency (MHz)	E_U (K)	1 A	1 B	1 C	2 A	2 B	2 C	2 D	2 E	2 F	3 A	3 B	3 C
SO ₂	32 _{4,28} –32 _{3,29}	258,388.716	531.12	–	–	–	✓	✓	–	–	–	–	–	–	–
SO ₂	20 _{7,13} –21 _{6,16}	258,666.969	313.19	–	–	–	✓	✓	–	–	–	–	–	–	–
SO ₂ ^f	9 _{3,7} –9 _{2,8}	258,942.199	63.47	✓	✓	–	✓	✓	–	–	–	–	–	–	–
SO ₂	30 _{4,26} –30 _{3,27}	259,599.448	471.52	–	–	–	✓	✓	–	–	–	–	–	–	–
³⁴ SO ₂	16 _{1,15} –15 _{2,14}	241,509.046	130.31	–	–	–	✓	✓	–	–	–	–	–	–	–
³⁴ SO ₂	8 _{3,5} –8 _{2,6}	241,985.449	54.38	–	–	–	✓	✓	–	–	–	–	–	–	–
³⁴ SO ₂	18 _{1,17} –18 _{0,18}	243,936.052	162.59	–	–	–	–	✓	–	–	–	–	–	–	–
³⁴ SO ₂	14 _{0,14} –13 _{1,13}	244,481.517	93.54	–	–	–	✓	✓	–	–	–	✓?	–	–	–
³⁴ SO ₂	15 _{2,14} –15 _{1,15}	245,178.587	118.72	–	–	–	✓	✓?	–	–	–	–	–	–	–
³⁴ SO ₂	6 _{3,3} –6 _{2,4}	245,302.239	40.66	–	–	–	✓	✓?	–	–	–	✓	–	–	–
³⁴ SO ₂	13 _{3,11} –13 _{2,12}	259,617.203	104.91	–	–	–	✓	✓	–	–	–	–	–	–	–
³³ SO	6 _{7,6} –5 _{6,5}	259,280.331	47.12	–	–	–	✓	✓	–	–	–	–	–	–	–
³³ SO	6 _{7,7} –5 _{6,6}	259,282.276	47.12	–	–	–	✓	✓	–	–	–	–	–	–	–
³³ SO	6 _{7,8} –5 _{6,7}	259,284.027	47.12	–	–	–	✓	✓	–	–	–	–	–	–	–
³³ SO	6 _{7,9} –5 _{6,8}	259,284.027	47.12	–	–	–	✓	✓	–	–	–	–	–	–	–
SiO	6–5	260,518.009	43.76	–	✓?	–	✓	✓	✓	✓	–	✓	–	–	–
HDO	2 _{1,1} –2 _{1,2}	241,561.550	95.22	–	–	–	✓	✓	–	–	–	–	–	–	–
HDCO	4 _{2,3} –3 _{2,2}	257,748.701	62.78	–	–	–	✓?	–	–	–	–	–	–	–	–
HDCO	4 _{2,2} –3 _{2,1}	259,034.910	62.87	–	–	–	✓	–	–	–	–	–	–	–	–
HDS	1 _{0,1} –0 _{0,0}	244,555.580	11.74	–	–	–	–	–	✓	–	–	–	–	–	–
HDS	2 _{1,1} –2 _{0,2}	257,781.410	47.04	–	–	–	–	–	✓?	–	–	–	–	–	–

Notes.

^a Spectroscopic parameters were taken from the CDMS catalog for all species except HDO, for which the data were taken from the JPL database (see Section 4.3). The symbols “✓”, “✓?”, and “–” indicate, respectively, a detection, a tentative detection, and a nondetection of a given transition.

^b Methanol transitions likely blended with the H49 ϵ recombination line toward 1 A.

^c The 257,402.086 MHz CH₃OH and 257,403.5848 MHz CH₃CN transitions are blended in the spectrum of 2 B.

^d In the spectrum of 3 B, the $J = 5 - 4$ CH₃OH Q-branch as a whole is securely detected, even though the individual lines are not clearly visible.

^e Even though this is a $<3\sigma$ detection for 2 B, this CH₃CN transition is used in the rotational diagram analysis as it still contributes useful information (see Section 4.3 and Figure 16).

^f The SO₂ transitions likely suffering from significant opacity effects (as defined by $E_U < 100$ K and $\log(S\mu^2) > 1.0$) and thus excluded from the fitting in the rotational diagram for 2 A and 2 B (see Section 4.3 and Figure 16).

from calculating the deuterium fractionation (the abundance ratio of deuterated over hydrogenated isotopologues, D/H) toward N 105–2.

Several hydrogen recombination lines are observed toward source 1 A: H49 ϵ (241.86116 GHz), H54 η (243.94239 GHz), H53 η (257.19399 GHz), H41 γ (257.63549 GHz), and H36 β (260.03278 GHz). This is the first extragalactic detection of the ϵ , η , and γ transitions of the hydrogen recombination lines and will be reported elsewhere.

4.2. Spatial Distribution of the Molecular Line Emission

Figures 7–15 show the integrated intensity (moment 0) images for molecular species detected toward N 105 with ALMA. Methanol is detected toward all the continuum sources, with the faintest emission associated with those in N 105–3. Other species detected toward all the sources are SO, CS, and H¹³CO⁺.

4.2.1. N 105–1

Figure 7 shows the CS, H¹³CO⁺, CH₃OH, and SO integrated intensity images of the N 105–1 field centered on the continuum source A (1 A), while the distribution of the SO₂ emission for three detected transitions toward 1 A are shown in Figure 8.

Toward 1 A, none of the molecular line peaks coincide with the 1.2 mm continuum peak. The CH₃OH and CS emissions

are extended with multiple peaks throughout the region. Two of the brightest CS peaks are offset to the north from the 1 A continuum peak, with the closer one roughly coinciding with the SO₂ and SO peaks, as illustrated in the three-color image in Figure 9; only the faint extended CH₃OH emission has been detected at the position of the two CS peaks. The H recombination line emission (all transitions) tracing the ionized gas coincides with the 1.2 mm continuum peak.

The integrated intensity images for N 105–1 centered on continuum sources B and C (1 B and 1 C) are shown in Figure 10. Both 1 B and 1 C were detected at the edge of the field of view, i.e., in an area of significantly reduced sensitivity, and as a result, their spectra are noisy. In Figure 10 we show the integrated intensity images for four species detected toward these sources with the highest signal-to-noise ratio: CS, H¹³CO⁺, CH₃OH, and SO. In the three-color image in Figure 11, we compare the distribution of the CH₃OH, CS, SO, and continuum emission. Figures 10 and 11 show that toward 1 B, the brightest CH₃OH peak coincides with the 1.2 mm continuum peak. The CH₃OH emission extends to the west with another, fainter peak associated with the SO emission. Some faint SO emission is associated with the continuum peak, but two SO peaks are offset to the east and the emission gets brighter with distance from the continuum peak. The CS emission peak is located between the CH₃OH/SO peak to the west of the continuum peak. The fainter H¹³CO⁺, H¹³CN, and HNCO emission peaks are offset from the continuum peak.

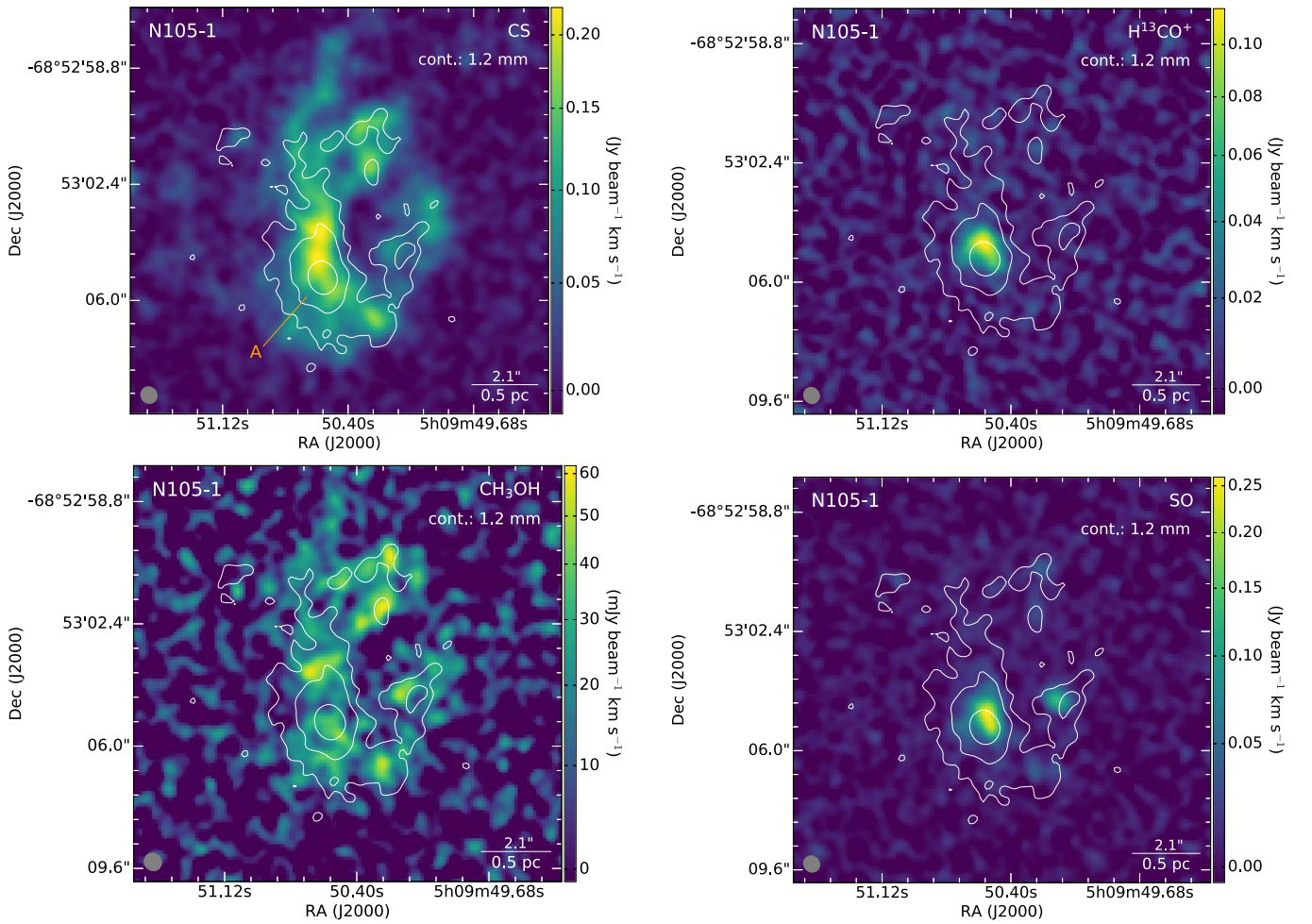


Figure 7. From left to right, top to bottom: The CS (5–4), H^{13}CO^+ (3–2), CH_3OH (combined $5_{1,5}-4_{1,4}$ E and $5_{0,5}-4_{0,4}$ A transitions), and SO 6_6-5_5 integrated intensity images of N 105–1 around the continuum source 1 A (color maps). The white contours in each image correspond to the 1.2 mm continuum emission with contour levels of (3, 10, 100) σ . The gray ellipse shown in the lower left corner of each image corresponds to the size of the ALMA synthesized beam (see Table 1).

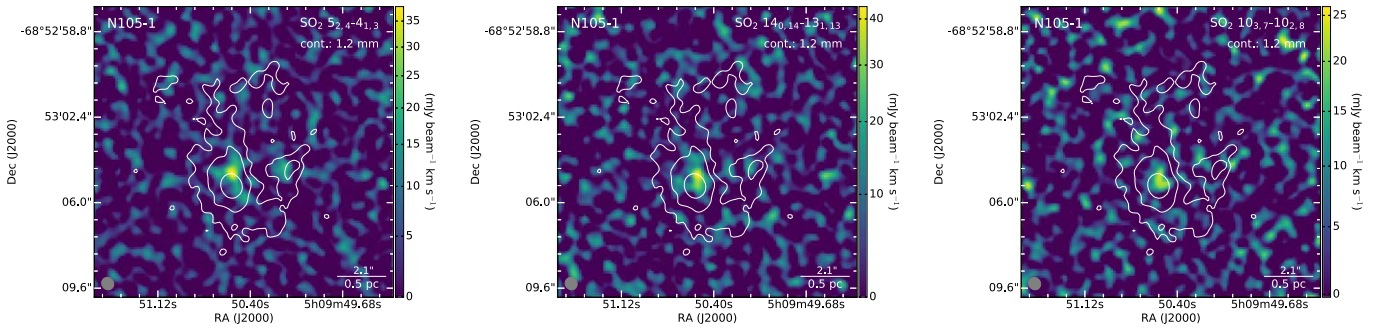


Figure 8. The SO_2 $5_{2,4}-4_{1,3}$ (left), $14_{0,14}-13_{1,13}$ (center), and $10_{3,7}-10_{2,8}$ (right) integrated intensity images of N 105–1 A. The white contours in each image correspond to the 1.2 mm continuum emission with contour levels of (3, 10, 100) σ .

Both the continuum and molecular line emission (SO , CS , and CH_3OH in particular) are elongated in the east–west direction with multiple peaks, indicating that more than one source may be present. The molecular line emission is slightly offset from the 1.2 mm continuum peak toward 1 C.

4.2.2. N 105–2

The integrated intensity images for N 105–2 are shown in Figures 12 and 13 (2 A–2 D and 2 F), and in Figure 14 (2 E). CH_3OH is widespread across the N 105–2 field with both the

compact emission associated with continuum sources and the extended emission throughout the region. Similar spatial distributions are seen for CS , H_2CS , SO , and H^{13}CO^+ . CS has its brightest, most extended component away from the continuum peaks. COMs other than CH_3OH have compact morphology and are located toward 2 A and 2 B only except CH_3CN ; faint CH_3CN emission is also detected toward 2 C. 2 C is the only source in N 105 covered by our observations with a detection of the HDS emission.

The most chemically rich continuum sources in N 105–2 are 2 A and 2 B. In general, the molecular line emission peaks

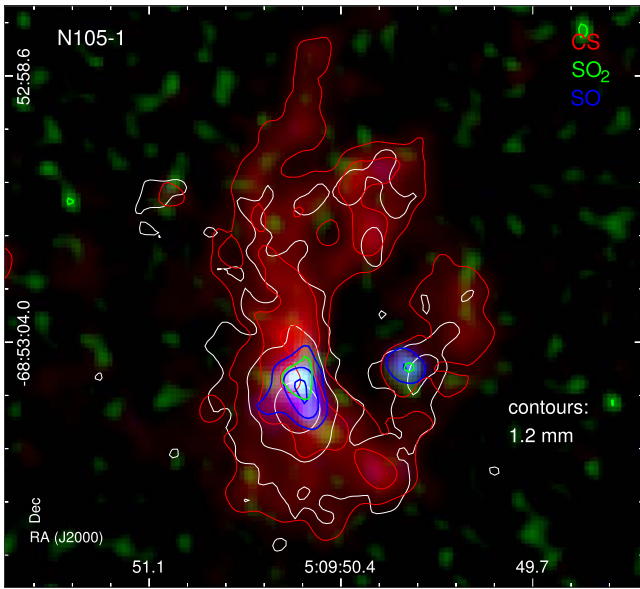


Figure 9. Three-color mosaic of the N105–1 A region, combining the CS (5–4) (red), SO₂ 5_{2,4}–4_{1,3} (green), and SO 6₆–5₅ (blue) integrated intensity images with the corresponding contours overlaid. The CS contour levels are (20, 50, 90)% of the CS emission peak of 230.8 mJy beam^{−1} km s^{−1}. The SO₂ contour level corresponds to 50% of the SO₂ emission peak of 39.4 mJy beam^{−1} km s^{−1} and the SO contour levels to the (20, 50, 90)% of the SO emission peak of 262.8 mJy beam^{−1} km s^{−1}. The white contours correspond to the 1.2 mm continuum with contour levels of (3, 10, 100).

coincide with the continuum peak toward 2 B. In 2 A, the CH₃CN peak is offset from the continuum peak by $\sim 0''.15$ – $0''.2$ and coincides with the emission peaks of other molecules such as CH₃OH, HNCO, HDO, HC¹⁵N, SO₂, OCS, and ³³SO. The emission from other species is slightly offset from both the CH₃CN/CH₃OH peak and the continuum peak, but within 1–1.5 pixels (or within $\sim 0''.2$). Such offsets are also observed toward other continuum sources in N105–2.

4.2.3. N105–3

Figure 15 shows the integrated intensity images of the four species detected toward all the continuum components in N105–3: CH₃OH, H¹³CO⁺, CS, and SO. The CH₃OH emission detected toward 3 B is the faintest out of all the continuum sources we analyzed in N105. None of the molecular line emission peaks (including SO₂ and HC¹⁵N detected toward 3 A only) are right on the 1.2 mm continuum peaks in N105–3, but within 1–2 pixels ($\sim 0''.1$ – $0''.2$).

4.3. Spectral Modeling

We performed an initial assessment of the physical conditions in N105 by using a rotational diagram analysis for CH₃CN, CH₃OH, and SO₂ for sources with multiple CH₃CN, CH₃OH, and SO₂ line detections with a range of upper state energies (E_U). This analysis assumes the gas is in LTE and the lines are optically thin (Goldsmith & Langer 1999) and not blended with lines from other species. The rotational diagrams are shown in Figure 16 for the most chemically rich sources, 2 A and 2 B. For both sources, two temperature components for CH₃OH are clearly visible in the rotational diagrams, while the SO₂ rotational diagrams shows possible non-LTE effects, i.e., an apparent discontinuity in the distribution of the low- and high- E_U data points. For the fitting in the rotational diagram,

we excluded the SO₂ lines likely suffering from significant opacity effects, as defined by $E_U < 100$ K and $\log(S\mu^2) > 1.0$ (also see Shimonishi et al. 2021).

Spectral line modeling was then performed for all the continuum sources under the assumption of LTE and taking into account line blending and opacity effects, using a least-squares approach similar to Sewilo et al. (2018) to simultaneously retrieve best-fitting column densities, rotational temperatures, Doppler shifts, and spectral line widths for each species (i): $[N^i, T_{\text{rot}}^i, v_i, dv^i]$. Simultaneously modeling all lines of every detectable species in our observed frequency range is crucial in order to resolve line blending issues and optical depth effects that might otherwise bias the retrieved parameters.

Spectral line models were generated for each source using a custom Python routine (based on the code used by Cordiner et al. 2017). Spectroscopic parameters were taken from the Cologne Database for Molecular Spectroscopy (CDMS; Müller et al. 2001), where available, and additional data for HDO were taken from the JPL Molecular Spectroscopy Database (Pickett et al. 1998). Gaussian spectral line opacity profiles were assumed, and the source was assumed to fill the aperture (unity beam filling factor). The model sums the radiative source terms (in the equation of radiative transfer) in each spectral channel for emission from overlapping lines of both the same and different species. The peak opacity of each spectral line was calculated using equation A2 of Turner (1991), and the final, synthetic T_B spectrum was generated by combining the emission from the full set of lines in our frequency range based on their individual contributions to the radiation source function.

Optimization of the individual $[N^i, T_{\text{rot}}^i, v_i, dv^i]$ parameters for each species (i) was performed using the LMFIT nonlinear least-squares package (Newville et al. 2014). The goodness of fit between the observed and synthetic spectra was monitored via the reduced chi-square statistic (χ_R^2). A good fit to the observed spectra ($\chi_R^2 \approx 1.0$) was obtained for all species in all sources using a single set of $[N^i, T_{\text{rot}}^i, v_i, dv^i]$ parameters (cloud components) for each species, apart from CH₃OH toward N105–2 A–2 D and 2 F and SO₂ for 2 A, 2 B, and 2 F, which required two cloud temperature components in order to obtain $\chi_R^2 \approx 1.0$ (the two components are hereafter designated as “hot” and “cold” due to their significantly different best-fitting temperatures).

Multiple lines of CH₃OH were detected in each source, with differing upper-state energies (in the range from 35 K up to ~ 600 K for 2 A; see Table 3), enabling robust derivations of the CH₃OH rotational temperatures. Toward sources 2 A and 2 B, multiple lines of the hot core tracer CH₃CN were also detected, resulting in a more reliable estimate of the hot core gas temperature in those sources, as the hot core CH₃OH lines are more likely to be contaminated with the ambient interstellar medium (ISM) because CH₃OH is more widespread. Temperature information was also available in some cases for SO₂ and ³⁴SO₂. For the remaining species with single-line detections (H¹³CO⁺, HCN, HC¹⁵N, HC₃N, CS, C³³S, H₂CS, OCS, SO, ³³SO, SiO, NH₂CHO, HNCO, HDCO, CH₂CO, HDO, HDS), or multiline detections of insufficient strength for robust temperature determinations (e.g., CH₃OCH₃), we fixed their rotational temperatures to the best-fitting CH₃CN rotational temperature. When CH₃CN was not detected, the other molecules were assumed to follow the temperature of the (hot) CH₃OH component. In addition, when multiple lines of SO₂

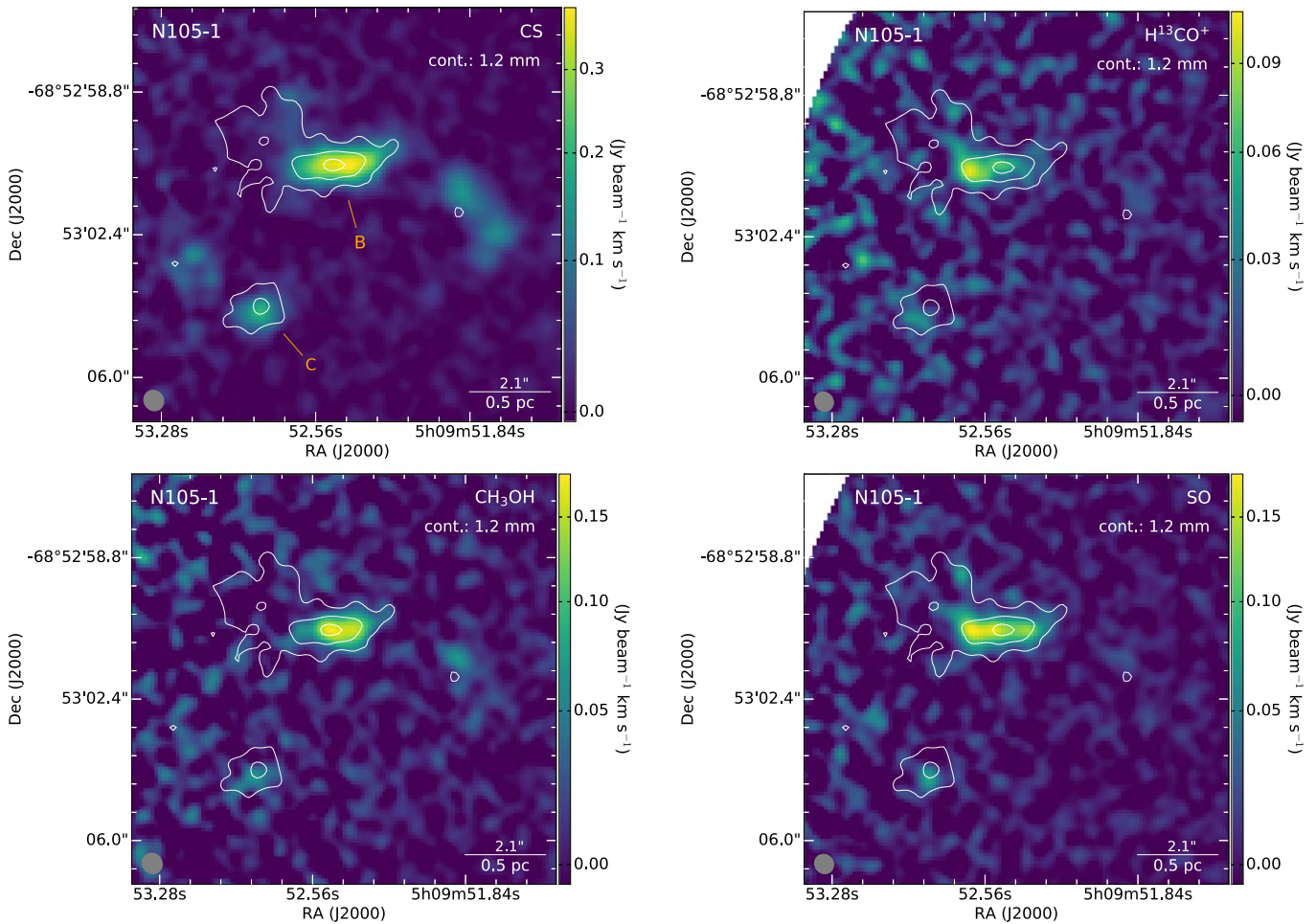


Figure 10. From left to right, top to bottom: The CS (5–4), H^{13}CO^+ (3–2), CH_3OH (combined $5_{1,5}-4_{1,4}$ E and $5_{0,5}-4_{0,4}$ A transitions), and SO 6_6-5_5 integrated intensity images of N 105–1 around the continuum sources B and C (1 B and 1 C). The white contours in each image correspond to the 1.2 mm continuum emission with contour levels of (3, 8, 15) σ .

were detected, the temperature of this species was obtained independently, and the temperatures of SO and ^{33}SO were tied to SO_2 , due to the chemical similarities between these species.

Error estimates on each free parameter were generated via Monte Carlo noise resampling. This involved the generation of 300 synthetic spectra for each source, obtained by adding random (Gaussian) noise to the best-fitting model spectra (with rms equivalent to the noise in nearby line-free spectral regions), which were subsequently refit to determine the distribution of possible model parameters. 1σ errors were determined from the $\pm 68\%$ ranges of the resulting parameter distributions, under the assumption of Gaussian statistics.

In the spectral fitting process, we used the CDMS/JPL partition functions ($Q(T_{\text{rot}})$); the CDMS data were used where available, i.e., for all species except HDO. In our experience, the CDMS catalog tends to have more complete partition functions than the JPL catalog, including information from higher-excitation states where available. In each case, we used the appropriate corresponding partition function from the respective catalog for each species, thus ensuring a consistent statistical weight scheme to that used in that catalog. Partition functions were tabulated at 0, 9.375, 18.75, 37.5, 75, 150, 225, and 300 K, and interpolated using a cubic spline.

For some molecules with noisy or tentative line detections, reliable parameter error estimates could not be obtained using

the Monte Carlo resampling method due to the tendency of the radial velocity parameter to drift into spectral regions affected by emission from nearby species, or with zero emission, leading to erroneous, or insufficient constraints on the model. In these cases, the radial velocities were held fixed at the value given by the initial least-squares fit, with the other parameters allowed to vary freely.

Our spectral modeling procedure implicitly accounts for line opacity effects in the derivation of molecular column densities and rotational temperatures. In general, the deconvolved source sizes are larger or similar in size to the ALMA beam size (see Table 4). However, there is a possibility for additional, unresolved, high-opacity interstellar cloud components within the beam of our ALMA observations, that could not be distinguished at the resolution and signal-to-noise ratio of our data. In that case, the spectral line opacities could have been underestimated, leading to a corresponding underestimate of the column densities.

The resulting rotational temperatures (T_{rot}), column densities (N), velocities (v_{LSR}), and line widths (Δv_{FWHM}) are listed in Table 6, along with the estimated abundances with respect to H_2 ($N(X)/N(\text{H}_2)$) and CH_3OH ($N(X)/N(\text{CH}_3\text{OH})$), where X represents a given species. $N(\text{H}_2)$ was estimated from the 1.2 mm continuum, as described in Section 5.

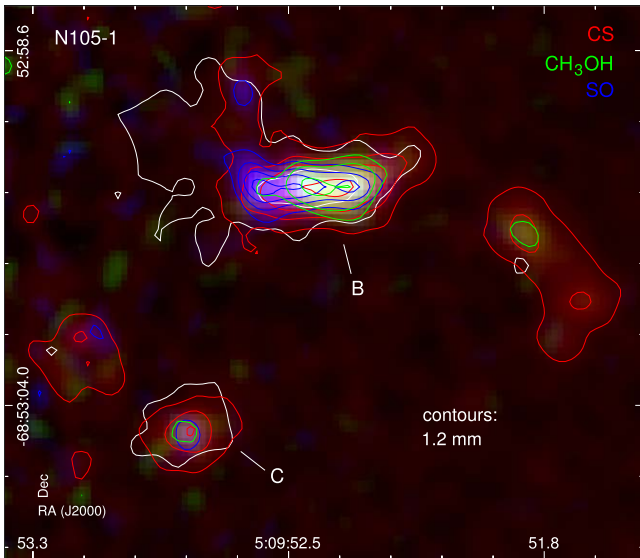


Figure 11. Three-color mosaic of the N 105-1 B/1 C region, combining the CS (5-4) (red), CH₃OH (combined 5_{1,5}-4_{1,4} E and 5_{0,5}-4_{0,4} A transitions) (green), and SO 6₆-5₅ (blue) integrated intensity images with the corresponding contours overlaid. The CS contour levels are (10, 30, 50, 90)% of the CS emission peak of 400.5 mJy beam⁻¹ km s⁻¹. The CH₃OH contour levels correspond to (30, 50, 90)% of the CH₃OH emission peak of 179.2 mJy beam⁻¹ km s⁻¹, and the SO contour levels to the (30, 50, 70, 90)% of the SO emission peak of 182.2 mJy beam⁻¹ km s⁻¹. The white contours correspond to the 1.2 mm continuum with contour levels of (3, 10)σ.

Observed spectra with overlaid model fits are presented in Appendix B.

4.3.1. SO₂ Excitation in N 105-2 A and 2 B

Since the SO₂ rotational diagrams for N 105-2 A and 2 B (Figure 16) indicate a problem with the excitation of SO₂ under the assumptions specified above, we have performed an additional analysis to investigate it. In an attempt to improve the spectral model fits, we explored the scenario with the relaxed assumption that the emission is beam filling, while still allowing for two components. These LTE fits were performed using XCLASS (Möller et al. 2017); the results are shown in Table 7. XCLASS LTE model spectra for SO₂ are overlaid on the observed spectra of 2 A and 2 B in Figures B2-B5 in Appendix B.

For 2 A, one large (approximately beam filling) and one very compact component with a size of 0''.05 (corresponding to 2500 au at the distance of N 105) are necessary to fit the data. The compact component is somewhat warmer than the extended component, representing an approximation of a centrally heated source with the temperature and steep density gradients. The very compact component could point at a disk at the center. The extended component is needed to adjust the line shapes of the otherwise flat-topped lines. Most of the line emission seems to be due to the compact component, which produces optically thick emission; this result is further constrained by the fit to three ³⁴SO₂ lines that cannot be achieved with the optically thin SO₂ emission. The corner plot of the Markov Chain Monte Carlo (MCMC) error estimate for the XCLASS LTE fit is shown in Figure A1 in Appendix A. Given the narrowness of the distribution peak for this case in Figure A1, this seems to be a robust result. The exact parameters cannot be constrained further with the current data

set and would require higher sensitivity and spatial resolution data for SO₂ and its isotopologues.

For 2 B, the results are similar to those obtained for 2 A; the spectra are best fitted by warmer, high column density and colder, more extended components. However, as can be seen in the MCMC corner plot in Figure A2, there is a large uncertainty regarding source sizes, temperatures, and column densities. Again, we cannot better constrain the parameters with the current data.

5. H₂ Column Densities, Masses, and Source Sizes

Assuming that the dust and gas are well-coupled ($T_{\text{dust}} \sim T_{\text{gas}} \sim T$), the H₂ column density can be estimated from the observed millimeter continuum flux using the formula (e.g., Hildebrand 1983; Kauffmann et al. 2008):

$$N(\text{H}_2) = \frac{S_\nu^{\text{beam}} R_{\text{gd}}}{\Omega_A \mu_{\text{H}_2} m_{\text{H}} \kappa_{\nu,d} B_\nu(T)}, \quad (1)$$

where S_ν^{beam} is the flux per synthesized beam; R_{gd} is the gas-to-dust mass ratio; Ω_A is the beam solid angle, $\Omega_A = \frac{\pi}{4 \ln 2} \theta_{\text{maj}} \theta_{\text{min}}$, where θ_{maj} and θ_{min} are the major and minor axes of the synthesized beam, respectively; μ_{H_2} is the mean molecular weight per hydrogen molecule (e.g., Cox 2000; Kauffmann et al. 2008; $\mu_{\text{H}_2} \approx 2.76$ for the LMC, Rémy-Ruyer et al. 2014); m_{H} is the mass of the hydrogen atom; $\kappa_{\nu,d}$ is the dust opacity per unit mass (e.g., Hildebrand 1983; Shirley et al. 2000); and $B_\nu(T)$ is the Planck function. The assumption of thermal equilibrium between the gas and dust holds for high-density regions ($n_{\text{H}_2} \gtrsim 10^5 \text{ cm}^{-3}$), including hot cores where the temperature exceeds 100 K (e.g., Goldsmith & Langer 1978; Ceccarelli et al. 1996; Kaufman et al. 1998).

The dust opacity for the LMC was derived by Galliano et al. (2011) for a large area of the LMC and thus is primarily relevant to the diffuse ISM. For our analysis focused on ~ 0.1 pc scales, we adopt a Galactic dust opacity from Ossenkopf & Henning (1994) for the model with an initial MRN distribution (Mathis et al. 1977) with thin ice mantles after 10^5 yr of coagulation at a hydrogen gas density of 10^6 cm^{-3} . For 1.24 mm (242.4 GHz), we adopt the opacity per unit dust mass of $\kappa_{1.24 \text{ mm,d}}$ of $0.993 \text{ cm}^2 \text{ g}^{-1}$ (Table 1 in Ossenkopf & Henning 1994).

It has been shown that the gas-to-dust mass ratio (R_{gd}) strongly depends on metallicity but shows a significant scatter (e.g., Roman-Duval et al. 2014; Rémy-Ruyer et al. 2014, 2015) attributed to differences in star formation histories of the galaxies (see, e.g., Galliano et al. 2018). We determined the LMC gas-to-dust mass ratio by scaling the Galactic value using the empirical broken-power-law relationship between gas-to-dust mass ratio and metallicity (defined as $Z_{\text{gal}}/Z_\odot = [\text{O}/\text{H}]_{\text{gal}}/[\text{O}/\text{H}]_\odot$, where $[\text{O}/\text{H}]_\odot = 4.9 \times 10^{-4}$; Asplund et al. 2009) from Rémy-Ruyer et al. (2014), which adopts the solar gas-to-dust mass ratio of 162 (Zubko et al. 2004). For the $\log[\text{O}/\text{H}]$ abundance ratio in the LMC H II regions of -3.6 (or $Z_{\text{LMC}} \sim 0.5 Z_\odot$; e.g., Pagel 2003), we estimate the gas-to-dust mass ratio of 316 for the LMC. This value is in agreement (within the uncertainties) with R_{gd} found by Roman-Duval et al. (2014) for the LMC based on the Herschel data.

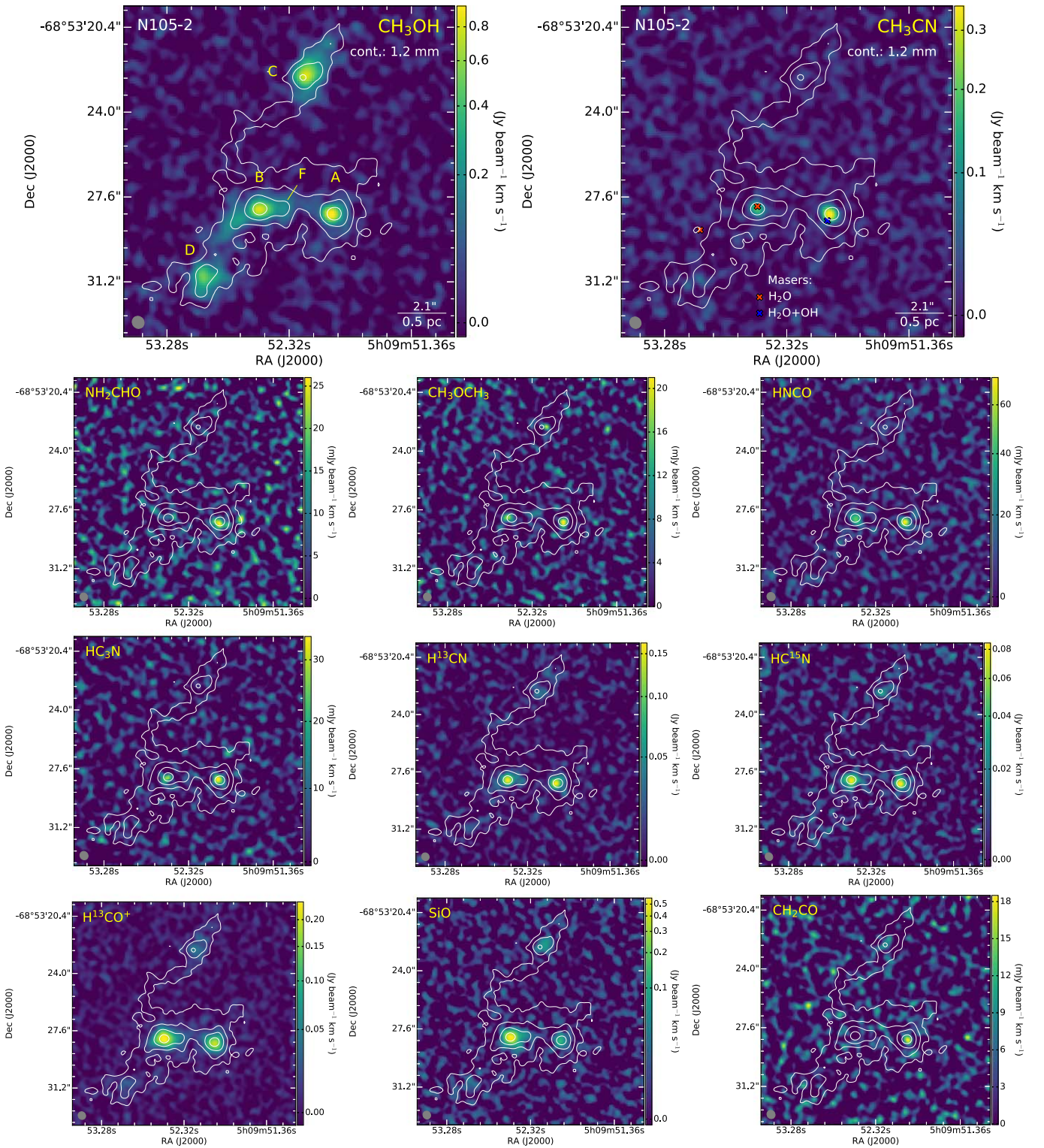


Figure 12. The integrated intensity images of the molecular species detected toward N 105–2 A–2 D and 2 F (from left to right, top to bottom): CH_3OH (integrated over all CH_3OH transitions detected in the ~ 242 GHz spectral window), CH_3CN (integrated over the $K = 0–6$ components of the CH_3CN $14_K–13_K$ ladder), NH_2CHO $12_{2,10}–11_{2,9}$, CH_3OCH_3 $14_{1,14}–13_{0,13}$, HNC (integrated over the $11_{0,11}–10_{0,10}$ and $11_{1,10}–10_{1,9}$ transitions), HC_3N $27–26$, H^{13}CN $3–2$, HC^{15}N $3–2$, H^{13}CO^+ $3–2$, SiO $6–5$, and CH_2CO $12_{1,11}–11_{1,10}$. The 1.2 mm continuum contours with contour levels of (3, 10, 30, 80) σ are overlaid in each image for reference. The positions of H_2O and OH masers are shown in the CH_3CN image. The size of the ALMA synthesized beam is indicated in the lower left corner of each image.

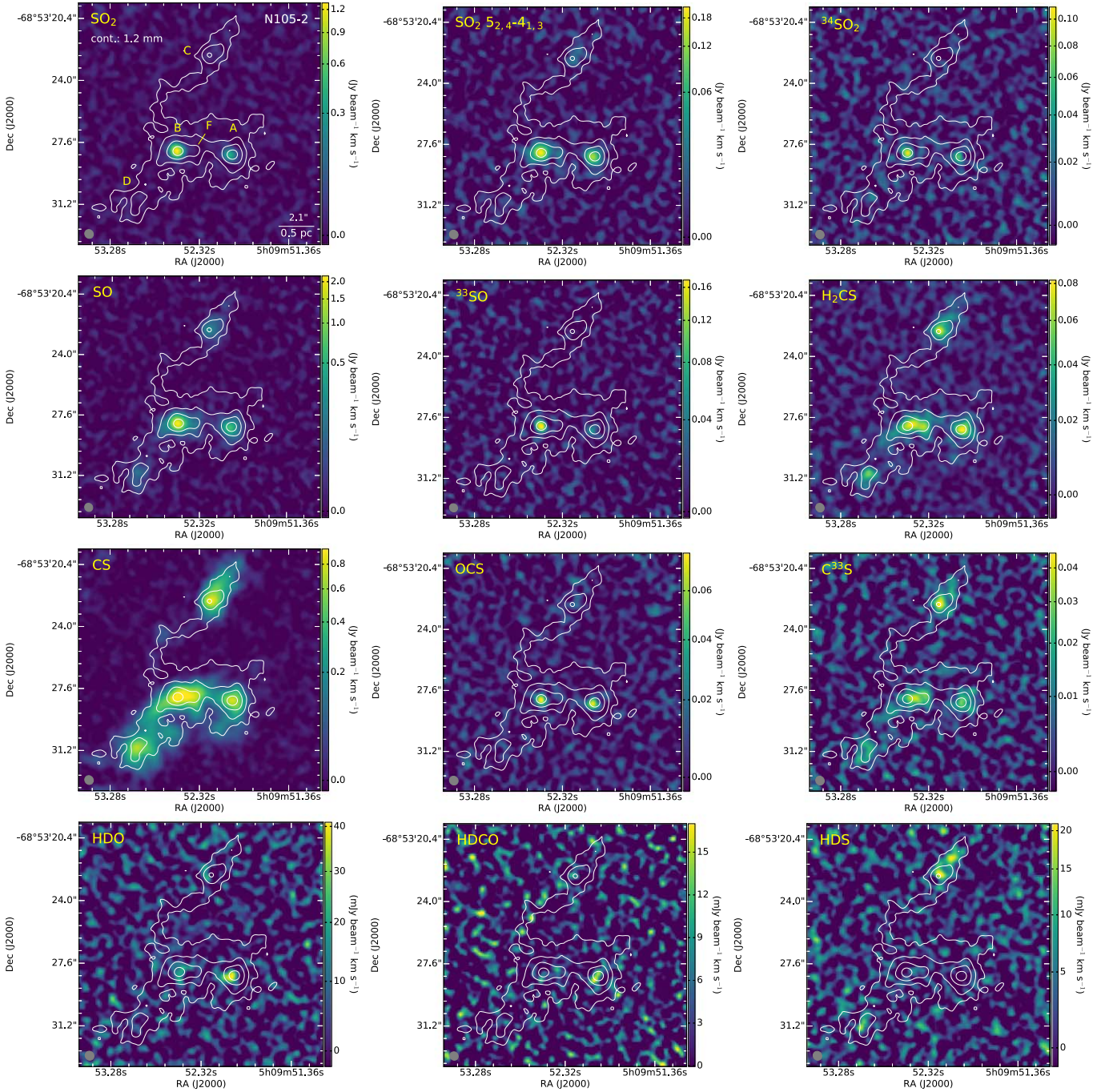


Figure 13. Same as Figure 12 but for (from left to right, top to bottom): SO_2 (integrated over all the transitions detected in the ~ 245 GHz spectral window), SO_2 $5_{2,4}-4_{1,3}$ (integrated over the channels containing the line emission from component C), $^{34}\text{SO}_2$ (integrated over all the transitions detected in the ~ 245 GHz spectral window), SO 6_6-5_5 , ^{33}SO 7_6-6_5 , H_2CS $7_{1,6}-6_{1,5}$, CS $5-4$, OCS $20-19$, C^{33}S 7_6-6_5 , HDO $2_{1,1}-2_{1,2}$, HDCO $4_{2,2}-3_{2,1}$, and HDS $1_{0,1}-0_{0,0}$.

We calculate $N(\text{H}_2)$ using Equation (1) in the form presented in Kauffmann et al. (2008):

$$\begin{aligned}
 N(\text{H}_2) = & 2.02 \cdot 10^{20} (e^{1.439(\lambda/\text{mm})^{-1}(T/10\text{K})^{-1}} - 1) \\
 & \cdot \left(\frac{\kappa_{\nu,d}/R_{\text{gd}}}{0.01 \text{ cm}^2 \text{ g}^{-1}} \right)^{-1} \left(\frac{I_{\nu}^{\text{beam}}}{\text{mJy beam}^{-1}} \right) \\
 & \cdot \left(\frac{\theta_{\text{HPBW}}}{10''} \right)^{-2} \left(\frac{\lambda}{\text{mm}} \right)^3 \text{ cm}^{-2}, \quad (2)
 \end{aligned}$$

where $\theta_{\text{HPBW}} = \sqrt{\theta_{\text{maj}} \cdot \theta_{\text{min}}}$.

For T , we adopt the temperatures determined based on CH_3CN for 2A and 2B and those based on CH_3OH for all other sources in N105. If both the hot and cold CH_3OH components are present for a given source, we used the temperature of the hot component.

I_{ν}^{beam} was measured as a mean intensity within the region used to extract spectra (I_{mean}), i.e., the area enclosed by the contour corresponding to 50% of the 1.2 mm continuum peak (see Section 4.3). We used the same areas to measure flux densities (F) and determined corresponding masses (M) for each source using the formula (Kauffmann et al. 2008):

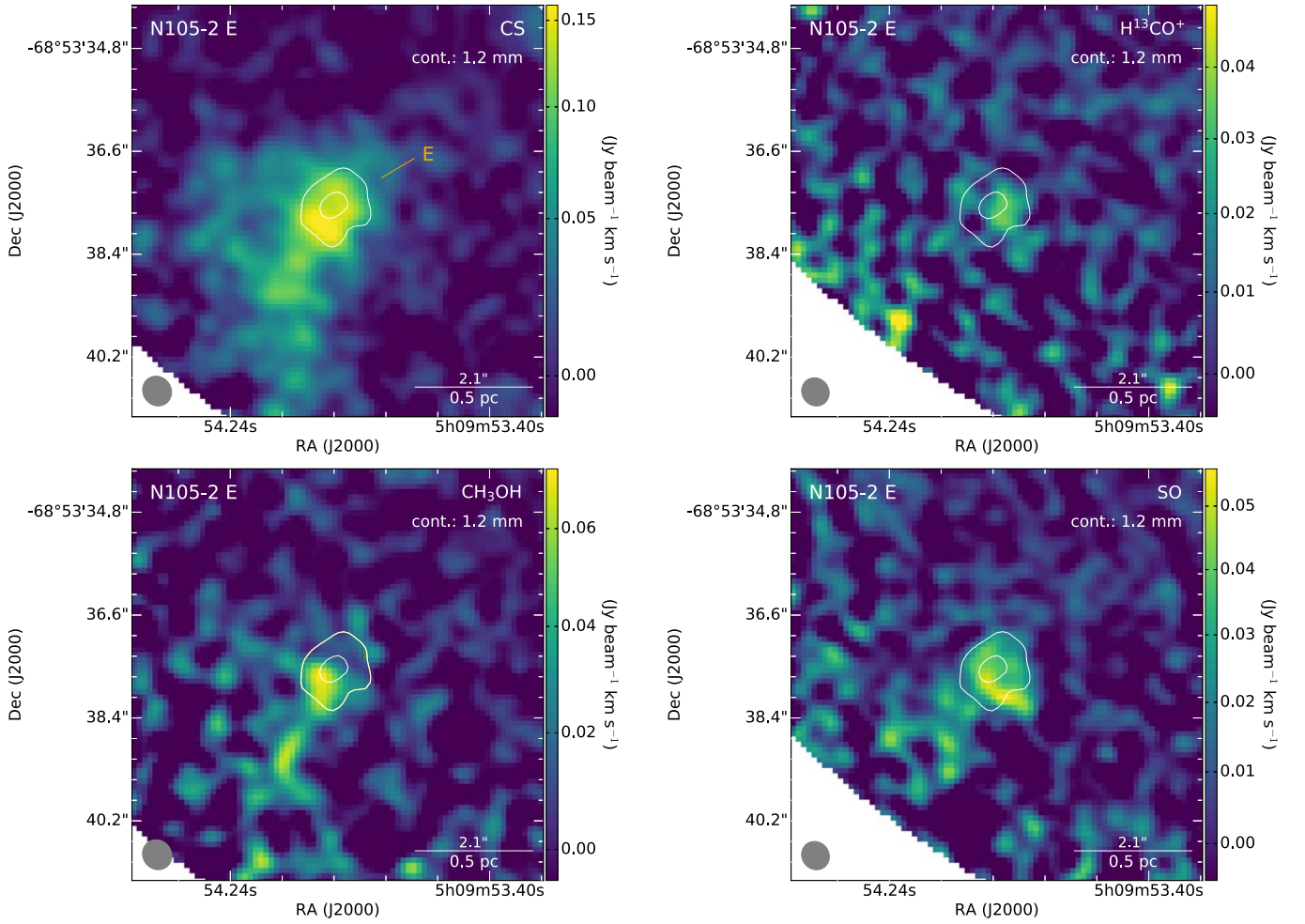


Figure 14. From left to right, top to bottom: The CS (5–4), H¹³CO⁺ (3–2), CH₃OH (combined 5_{1,5}–4_{1,4} E and 5_{0,5}–4_{0,4} A transitions), and SO 6₆–5₅ integrated intensity images of N 105–2 E. The white contours in each image correspond to the 1.2 mm continuum emission with contour levels of (3, 8)σ.

$$M = 0.12 M_{\odot} \cdot (e^{1.439(\lambda/\text{mm})^{-1}(T/10\text{ K})^{-1}} - 1) \cdot \left(\frac{\kappa_{\nu,d}/R_{\text{gd}}}{0.01\text{ cm}^2\text{ g}^{-1}} \right)^{-1} \left(\frac{F_{\nu}}{\text{Jy}} \right) \cdot \left(\frac{D}{100\text{ pc}} \right)^2 \left(\frac{\lambda}{\text{mm}} \right)^3, \quad (3)$$

where D is the distance to the LMC, and other parameters are the same as in Equations (1) and (2).

We determined the source sizes utilizing a common definition of an “effective” radius: $R_{\text{eff}} = 2\sqrt{A/\pi}$, where A is the source area. We adopted the area contained within the 50% of the continuum peak intensity contour as A and calculated the source size at the half-peak as $\text{FWHM}_{\text{eff}} = 2 \cdot R_{\text{eff}}$. Assuming the sources can be represented by Gaussian profiles, we calculated the deconvolved sizes $\text{FWHM}_{\text{eff,deconv}} = \sqrt{\text{FWHM}_{\text{eff}}^2 - \text{HPBW}^2}$, where HPBW (the half-power beamwidth) is the geometric mean of the minor and major axes of the synthesized beam.

The continuum peak intensities (I_{peak}), mean intensities (I_{mean}), observed and deconvolved source sizes (FWHM_{eff} and $\text{FWHM}_{\text{eff,deconv}}$), fluxes and masses calculated for the area above the 50% of the peak intensity (F_{50} and $M_{50,\text{gas}}$), and H₂ column densities ($N(\text{H}_2)$) are listed in Table 4.

In addition to $N(\text{H}_2)$ calculated based on the CH₃OH temperature, Table 4 also lists $N(\text{H}_2)$ determined based on

CH₃CN and/or SO₂ where available (CH₃CN: 2 A and 2 B; SO₂: 1 A, 1 B, 2 A, 2 B, 2 C, and 3 A). For 2 A, all values of $N(\text{H}_2)$ agree within the uncertainties with $N(\text{H}_2)$ calculated using $T(\text{CH}_3\text{CN})$ being ~6% higher than the average $N(\text{H}_2)$. For 2 B, the differences between $N(\text{H}_2)$ calculated using different temperatures is larger with $N(\text{H}_2)$ based on $T(\text{CH}_3\text{CN})$ being ~37% higher than the average $N(\text{H}_2)$.

The largest discrepancy between $N(\text{H}_2)$ derived based on different species exists for 1 A with $N(\text{H}_2)$ derived using $T(\text{CH}_3\text{OH}) \sim 12\text{ K}$ being one order of magnitude higher than that derived using $T(\text{SO}_2) \sim 96\text{ K}$. The former $N(\text{H}_2)$ value is 1–2 orders of magnitude larger than $N(\text{H}_2)$ for all the other continuum sources in N 105 (see Table 4). Such a large difference in temperature between CH₃OH and SO₂ can be the result of CH₃OH and SO₂ tracing different physical components (an extended cold CH₃OH emission and SO₂ produced in outflow shocks) or non-LTE effects (see Section 7.1). Considering the large uncertainties in the determination of $N(\text{H}_2)$ based on the ALMA data, we have decided to use an independent measurement of $N(\text{H}_2)$.

We follow the procedure described in Shimonishi et al. (2020) to estimate $N(\text{H}_2)$ based on the value of A_{ν} we obtained using the KMOS observations ($42 \pm 4\text{ mag}$; see Section 6), which is consistent with that previously reported in literature (~40 mag; Oliveira et al. 2006; see also Sections 6). We use

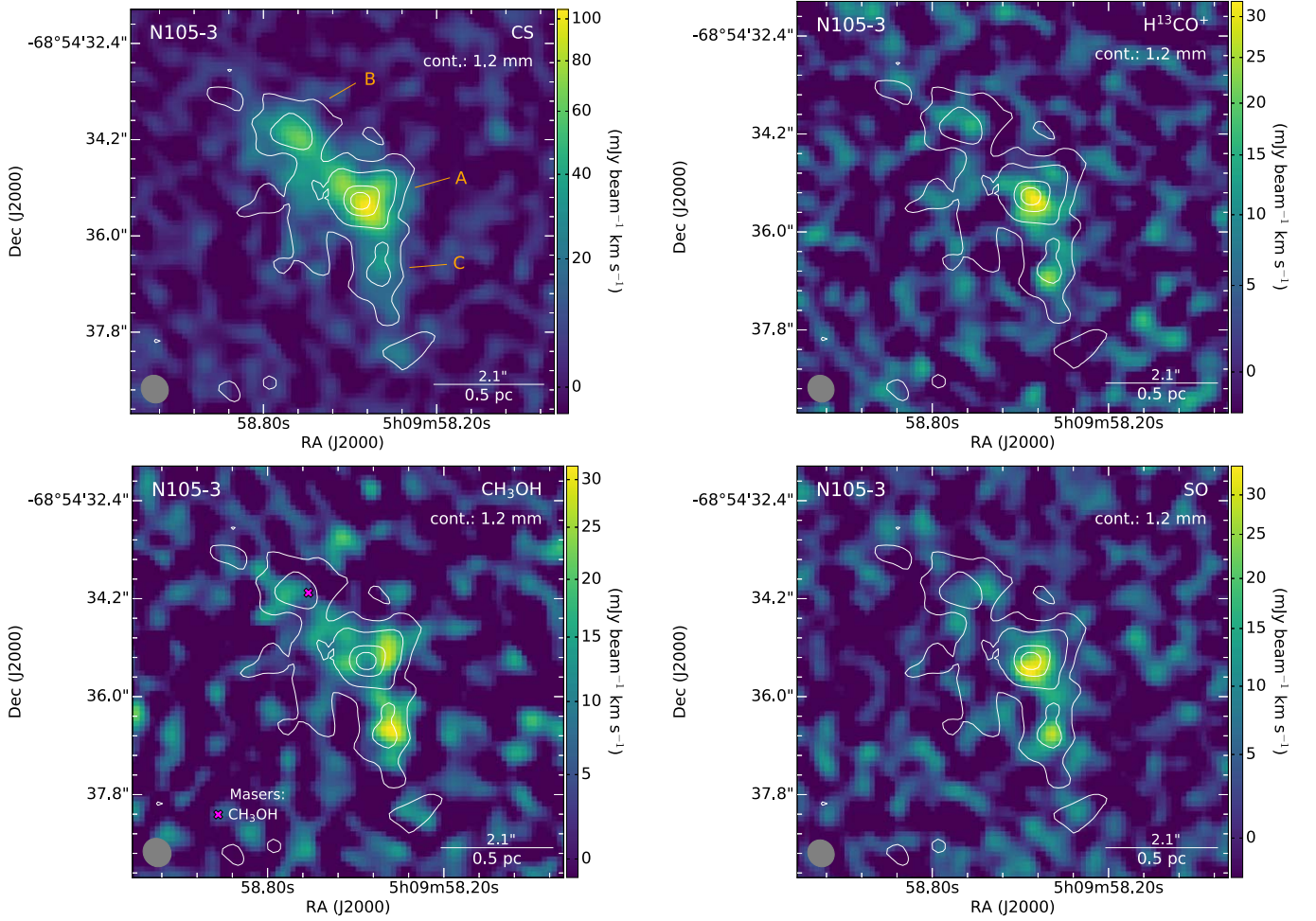


Figure 15. From left to right, top to bottom: The CS (5–4), H¹³CO⁺ (3–2), CH₃OH (combined 5_{1,5}–4_{1,4} E and 5_{0,5}–4_{0,4} A transitions), and SO 6₆–5₅ integrated intensity images of N 105–3. The white contours in each image correspond to the 1.2 mm continuum emission with contour levels of (3, 7, 10, 20)σ. The position of the CH₃OH masers (see Section 3.1) is indicated in the image at the upper left.

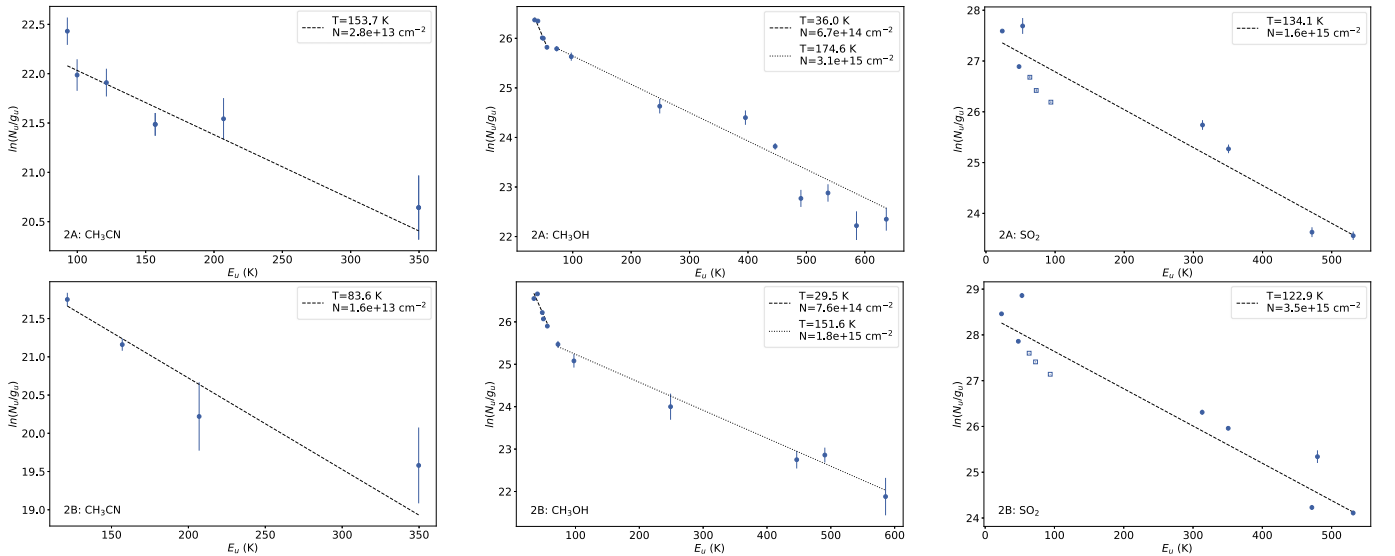


Figure 16. Rotational diagrams for sources N 105–2 A (top panel) and 2 B (bottom panel) for (from left to right): CH₃CN, CH₃OH, and SO₂. Only the transitions with the integrated flux above 2σ are included in the diagrams. For CH₃CN, the two strongest lines had to be excluded for 2 B because they are blended, and another CH₃CN transition was excluded for both 2 A and 2 B because it is blended with the CH₃OH line. Open box symbols indicate the SO₂ transitions suffering from significant opacity effects and thus are excluded from the fit (see Section 4.3 for details). The rotational temperatures and column densities derived based on the rotational diagram analysis are indicated in the upper right corner in each plot.

Table 4
Continuum Intensities and H₂ Column Densities

Source	R.A. (J2000) ^a (^h ^m ^s)	Decl. (J2000) ^a ([°] ['] ^{''})	$I_{\text{peak}}^{\text{b}}$ (mJy beam ⁻¹)	$I_{\text{mean}}^{\text{c}}$ (mJy beam ⁻¹)	Area ^c (arcsec ²)	FWHM _{eff} (^{''} /pc)	FWHM _{eff,deconv} (^{''} /pc)	F_{50}^{e} (mJy)	$M_{50,\text{gas}}^{\text{e}}$ (M_{\odot})	$N(\text{H}_2)^{\text{f}}$	$N(\text{H}_2)^{\text{g}}$ (10 ²³ cm ⁻²)	$N(\text{H}_2)^{\text{h}}$
N 105-1 A	05:09:50.54	-68:53:05.4	31.003 ^d	22.370 ^d	0.305	0.62/0.15	0.39/0.10	25.2 ^d	3706 ⁺⁵⁹⁷ ₋₄₇₅	93 ⁺¹⁵ ₋₁₂	...	7.4 ^{+1.8} _{-1.8}
1 B	05:09:52.48	-68:53:00.7	2.329	1.575	0.923	1.08/0.26	0.97/0.23	5.4	1038 ⁺¹⁰⁹ ₋₁₀₈	8.6 ^{+1.0} _{-1.0}	...	4.8 ^{+1.0} _{-1.0}
1 C	05:09:52.82	-68:53:04.3	1.437	1.008	0.601	0.87/0.21	0.73/0.18	2.2	390 ⁺⁹⁵ ₋₈₇	5.0 ^{+1.2} _{-1.2}
N 105-2 A	05:09:51.96	-68:53:28.3	6.362	4.560	0.423	0.73/0.18	0.55/0.13	7.1	102 ⁺¹² ₋₁₃	1.6 ^{+0.3} _{-0.2}	1.8 ^{+0.2} _{-0.2}	1.7 ^{+0.2} _{-0.2}
2 B	05:09:52.56	-68:53:28.1	6.181	4.382	0.415	0.73/0.18	0.54/0.13	6.7	170 ⁺²⁷ ₋₂₆	2.0 ^{+0.2} _{-0.2}	3.1 ^{+0.5} _{-0.5}	1.7 ^{+0.2} _{-0.2}
2 C	05:09:52.22	-68:53:22.6	1.799	1.217	0.474	0.78/0.19	0.60/0.15	2.1	50 ⁺¹⁶ ₋₁₂	0.8 ^{+0.3} _{-0.2}	...	2.7 ^{+0.5} _{-0.4}
2 D	05:09:52.99	-68:53:31.0	1.344	0.910	0.592	0.87/0.21	0.72/0.17	2.0	161 ⁺¹⁹ ₋₁₈	2.1 ^{+0.3} _{-0.3}
2 E	05:09:53.90	-68:53:37.6	1.269	0.896	0.618	0.89/0.22	0.74/0.18	2.0	501 ⁺⁹⁵ ₋₇₉	6.2 ^{+1.2} _{-1.0}
2 F	05:09:52.39	-68:53:28.1	2.397	1.2 ^{+0.4} _{-0.3}
N 105-3 A	05:09:58.48	-68:54:35.4	0.573	0.409	0.559	0.84/0.20	0.69/0.17	0.85	307 ⁺⁶⁹ ₋₅₇	4.2 ^{+1.0} _{-0.8}	...	1.0 ^{+0.3} _{-0.3}
3 B	05:09:58.70	-68:54:34.1	0.342	0.241	0.381	0.70/0.17	0.50/0.12	0.33	5 ⁺¹ ₋₂	0.09 ^{+0.03} _{-0.04}
3 C	05:09:58.41	-68:54:36.7	0.221	2.2 ^{+1.1} _{-0.8}
N 113 A1	05:13:25.17	-69:22:45.5	13.136	9.399	0.606	0.88/0.21	0.55/0.13	10.7	214 ⁺²⁴ ₋₂₄	2.7 ^{+0.3} _{-0.3}
B3	05:13:17.18	-69:22:21.5	6.306	4.332	1.128	1.2/0.29	0.98/0.24	9.2	184 ⁺²⁹ ₋₃₀	1.2 ^{+0.2} _{-0.2}

Notes.

^a The continuum peak positions at ~ 242.2 GHz for sources in N 105 (this paper) and ~ 224.3 GHz for N 113 A1 and B3 (Sewilo et al. 2018).

^b I_{peak} is the observed 1.2 mm continuum intensity peak.

^c I_{mean} is the 1.2 mm continuum intensity averaged over the area (Area) within the contour corresponding to the 50% of the 1.2 mm continuum peak. This is the same area used to extract spectra for the analysis (see Section 4). The beam areas for the (N 105-1, N 105-2, N 105-3, N 113) observations are (0.270, 0.273, 0.270, 0.534) arcsec².

^d The observed values, i.e., not corrected for the contribution from the free-free emission (see Section 3).

^e F_{50} and $M_{50,\text{gas}}$ are flux densities and masses, respectively, calculated for the area above the 50% of the peak intensity.

^f $N(\text{H}_2)$ calculated assuming $T = T_{\text{rot}}(\text{CH}_3\text{OH})$ (see Section 5 for details).

^g $N(\text{H}_2)$ calculated assuming $T = T_{\text{rot}}(\text{CH}_3\text{CN})$.

^h $N(\text{H}_2)$ calculated assuming $T = T_{\text{rot}}(\text{SO}_2)$.

the relation $N(\text{H}_2)/A_V = 2.8 \times 10^{21} \text{ cm}^{-2} \text{ mag}^{-1}$ for the LMC; the value of A_V is doubled before it is used in this formula to obtain the total column density along the line of sight (see Shimonishi et al. 2020 and references therein). The resulting $N(\text{H}_2)$ for 1 A is $(2.4 \pm 0.2) \times 10^{23} \text{ cm}^{-2}$.

We used $N(\text{H}_2)$ calculated using the CH_3CN temperature (2 A and 2 B), CH_3OH temperature (the remaining sources except 1 A), and derived from A_V (1 A) to determine molecular abundances with respect to H_2 listed in Table 6.

We have estimated the H_2 number density, n_{H_2} , using the relation $n_{\text{H}_2} = N(\text{H}_2)/\text{FWHM}_{\text{eff,deconv}}$. All the sources except 3 B have n_{H_2} of at least a few times 10^5 cm^{-3} ; n_{H_2} of hot cores 2 A and 2 B is $\sim 4.6 \times 10^5 \text{ cm}^{-3}$ and $\sim 7.8 \times 10^5 \text{ cm}^{-3}$, respectively.

6. ALMA Fields in N 105 from Optical to Radio Wavelengths

N 105A (overlapping with N 105–1 and N 105–2) was observed by Indebetouw et al. (2004) with ATCA at 8.6 GHz (3 cm) and 4.8 GHz (6 cm) with a resolution of $\sim 1''.5$ and $\sim 2''$. They detected four radio continuum sources, three of which are in the ALMA fields: B0510–6857 W coincides with N 105–1 A, B0510–6857 E is associated with the 1.2 mm continuum emission extending toward east from N 105–1 B, and B0510–6857 S lies between N 105–2 A, 2 B, and 2 C. Indebetouw et al. (2004) determined spectral types of ionizing stars of O6.5 V, O7.5 V, and O8.5 V for radio continuum components W, E, and S, respectively. Source B0510–6857 S is the faintest out of the three radio components at both wavelengths, while sources W and E are the brightest at 3 cm and 6 cm, respectively. Indebetouw et al. (2004) derived spectral indices of +0.6, 0, and -0.2 for B0510–6857 W, E, and S, respectively. In the lower-resolution ($\sim 10''$) 6.6 GHz image presented in Ellingsen et al. (1994), all the continuum sources from Indebetouw et al. (2004) remain unresolved and associated with an extended ionized gas emission.

Radio source B0510–6857 W/ALMA N 105–1 A is associated with the infrared source N 105A IRS1 from Oliveira et al. (2006), a candidate protostar first identified by Epchtein et al. (1984). The 3–4 μm spectrum from the Infrared Spectrometer And Array Camera (ISAAC) on the ESO-VLT presented by Oliveira et al. (2006) displays a very red continuum and strong hydrogen recombination line emission: $\text{Br}\alpha$ and $\text{Pf}\gamma$. Oliveira et al. (2006) argue that nondetection of the $\text{Pf}\delta$ line indicates a high dust column density in front of the region of the line emission; they estimate a total visual extinction A_V of ~ 40 mag. The $\text{Br}\alpha$ line detected toward IRS1 shows broad wings and is asymmetric, providing a strong evidence for the bipolar outflow. N 105A IRS1 is very bright in the L' band, and it is extremely red ($K_S-L' = 3.9$ mag). Based on the analysis of the spectral energy distribution (SED) and IR colors of IRS1, and the presence of strong recombination lines and the outflow, Oliveira et al. (2006) concluded that IRS1 is likely an embedded massive YSO ionizing its immediate surroundings.

Radio source B0510–6857 E coincides with the extended 1.2 mm continuum emission east of N 105–1 B and is associated with the infrared source N 105A “blob A” from Oliveira et al. (2006), while N 105–1 B corresponds to “blob B.” Blob A is a bright core, while blob B is part of the extended and patchy L' -band emission surrounding it. Similarly to IRS1, the spectra of blobs A and B display H recombination lines;

however, the $\text{Pf}\delta$ line is detected toward both of them, indicating that the extinction by dust is significantly lower than toward IRS1. Blob A is also not as red as IRS1 ($K_S-L' = 1.51$ mag), and the continuum emission is extremely faint. The broad $\sim 3.3 \mu\text{m}$ PAH emission is underlying the $\text{Pf}\delta$ emission in both the blob A and B spectra. The spectral lines toward blob A are broader than those detected toward IRS1, and they are double-peaked, suggesting the presence of an outflow. No signs of an outflow are present in blob B’s spectrum. Blobs A and B correspond to VMC sources 558354728344 and 558354728373, respectively; they are unresolved in Spitzer images and both contribute to the emission from the Spitzer YSO 050952.73–685300.7 (see Section 3.1).

The area where B0510–6857 E, N 105–1 B, and N 105–1 C are located is coincident with the peak of the 888 MHz emission in N 105. The 888 MHz image with the spatial resolution of $13''.9 \times 12''.1$ (FWHM) presented in Pennock et al. (2021) was obtained with Australian Square Kilometre Array Pathfinder (ASKAP) telescope as part of the Evolutionary Map of the Universe survey.

The catalog position of the 3 cm/6 cm source B0510–6857 S is concentrated between N 105–2 A/2 B (offset by $\sim 4''$ north) and 2 C; the physical association between this radio emission and N 105–2 A–C is unclear.

The source IRS2 from Oliveira et al. (2006) corresponds to ALMA N 105–2 A. IRS2 is very faint in the L' band/ $3.78 \mu\text{m}$ (14.30 ± 0.34 mag); in comparison, the L' magnitude of IRS1 is 9.88 ± 0.01 . Oliveira et al. (2006) concluded that IRS2 could be an embedded YSO based on a suggestive association with water masers.

Ambrocio-Cruz et al. (1998) identified and characterized several $\text{H}\alpha$ features in N 105, including two in the brightest part of the region that they dubbed “bright entities” (BE). The boundary between these features (north and south BE) is at the location of an apparent optically dark region that can be seen in the right panel of Figure 2. The northern BE is coincident with N 105A (around the peak of the ^{12}CO emission) and overlaps with the N 105–1 and N 105–2 ALMA fields. N 105–3 lies in the southern BE associated with the fainter $\text{H}\alpha$ emission.

The MCELS $\text{H}\alpha$ image shows a hint of a filamentary $\text{H}\alpha$ -dark feature extending from the northern boundary of the larger optically dark region between the two BEs, first toward northwest and then northeast up to the region east of N 105–1 B/1 C and farther toward northeast-east roughly to the edge of the bright $\text{H}\alpha$ emission. This dark lane is also visible in the near-IR images of N 105–2 and N 105–1 where the extended emission in all VMC bands has been detected. The ALMA 1.2 mm continuum emission in N 105–2 coincides with the optically dark regions. Sources 2 A, 2 B, 2 D, and 2 F are located at the northern edge of the larger optically dark region, while the extended emission connecting sources 2 B and 2 C, as well as source 2 C lie in the dark lane. Several near-IR sources are detected throughout the region. Two very faint K_S -band sources are associated with the 2 A and 2 B continuum peaks; however, no near-IR or mid-IR source appear to coincide with 2 C, indicating that this source may be the youngest object in N 105–2.

The brightest mid- and far-IR emission in N 105 is associated with the northern BE/N 105A (see Figures 1, 4, and C1–C2). The structure of the Spitzer 8 μm emission, tracing hot gas and PAHs, is relatively complex with filaments

and shell-like structures, the latter being particularly evident in the southern BE. The ALMA 1.2 mm continuum sources in N 105–3 lie at the rim of the bubble outlined by the mid-IR emission. Similarly, N 105–2 A/2 B appear to be located at the southern rim of the smaller bubble filled with the extended 4.5 μm emission (likely dominated by H₂ emission from outflow shocks; Cyganowski et al. 2011). The extended 4.5 μm emission is detected throughout the northern BE/N 105A.

BEs and the bubble-shaped H α nebulae extending toward east and west are highly excited, displaying bright [O III] 5007 \AA emission (e.g., Ambrocio-Cruz et al. 1998). N 105 is photoionized by massive stars from the LH 31 OB association and two Wolf–Rayet (WR) stars (Brey 16 and Brey 16a; Breysacher 1981). Ambrocio-Cruz et al. (1998) found that the excitation level of the northern BE nebula (traced by the [O III]/H β ratio) is twice as large as the excitation level measured in the southern BE nebula. The WR star Brey 16a located $\sim 10''$ northeast from the ALMA continuum source N 105–1 B (see Figure 17) is most likely responsible for ionizing the northern BE with a possible contribution from the second WR star (Brey 16) located $\sim 1'$ east from N 105–2 A.

WR stars are hot, high-luminosity evolved stars with powerful, fast, and dense stellar winds (e.g., Crowther 2007). WR stars' winds, with the highest mechanical luminosities out of all massive stars, sweep up the ambient medium forming shells structures. Surprisingly, no bubble associated with the progenitor of Brey 16a is observed in N 105A. Ambrocio-Cruz et al. (1998) suggested that the observed morphology of the gas around WR stars is a combined effect of the powerful stellar winds propagating in an inhomogeneous medium and the fact that stars formed deep in their natal molecular cloud; such a scenario would lead to the blister H II regions observed in N 105. The natal molecular cloud has not been completely disrupted by massive stars yet, and it is still being photoevaporated and ionized. The molecular material is likely confined by stellar winds of the WR stars and OB stars in LH 31, which is consistent with the location of the protostars and masers at the rim of the northern BE. The ongoing star formation in N 105 might have been triggered by the winds of the progenitors of the WR stars in the northern BE and likely by the winds of the OB stars in LH 31 in the southern BE.

6.1. The Detection of the CO₂ Ice Band toward N 105–2 A

The Spitzer/IRS spectra of four point sources in N 105 were first described in Seale et al. (2009). They classified these sources using a principal component analysis, resulting in P (i.e., PAH-dominated) classifications for 1 A and 2 E and PE (PAH-dominated with significant fine-structure emission) classifications for 1 B/blob A (see Section 6) and 2 A/2 B. As it can be seen from Figure 18, the spectra are very similar, and the PAH and fine structure emission are very conspicuous. Silicate in absorption was reported by Seale et al. (2009) for 2 A/2 B and 2 E, but this is not clear at all from the spectra. Jones et al. (2017) reclassified all IRS spectra obtained for LMC sources; they find no evidence of silicate absorption in any of the spectra in N 105. They classify 1 A, 1 B/blob A, 2 A/2 B, and 2 E as YSO3/H II (1 A, 1 B/blob A, 2 A/2 B) and H II (2 E) types, i.e., relatively evolved YSOs with emerging compact H II regions. As pointed out by Jones et al. (2017), the IRS spectra alone are in fact not sufficient to

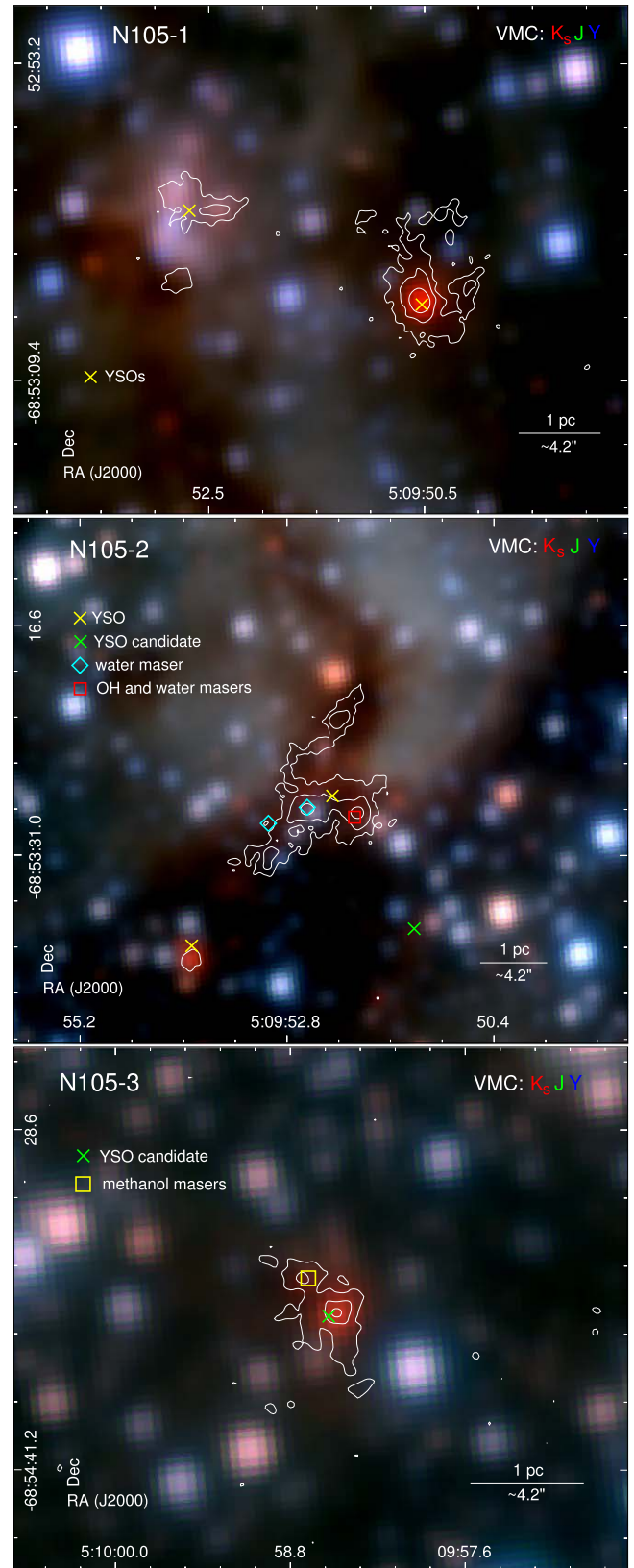


Figure 17. Three-color mosaics of N 105–1 (top), N 105–2 (center), and N 105–3 (bottom) combining the VMC K_s (red), J (green), and Y (blue) images. The positions of YSOs, YSO candidates, and masers are marked as indicated in the legends. The 1.2 mm continuum contours are $(3, 10, 60)\sigma_1$ for N 105–1, $(3, 10, 60)\sigma_2$ for N 105–2, and $(3, 10, 20)\sigma_3$ for N 105–3; σ_1 , σ_2 , and σ_3 are the same as those in Figure 4.

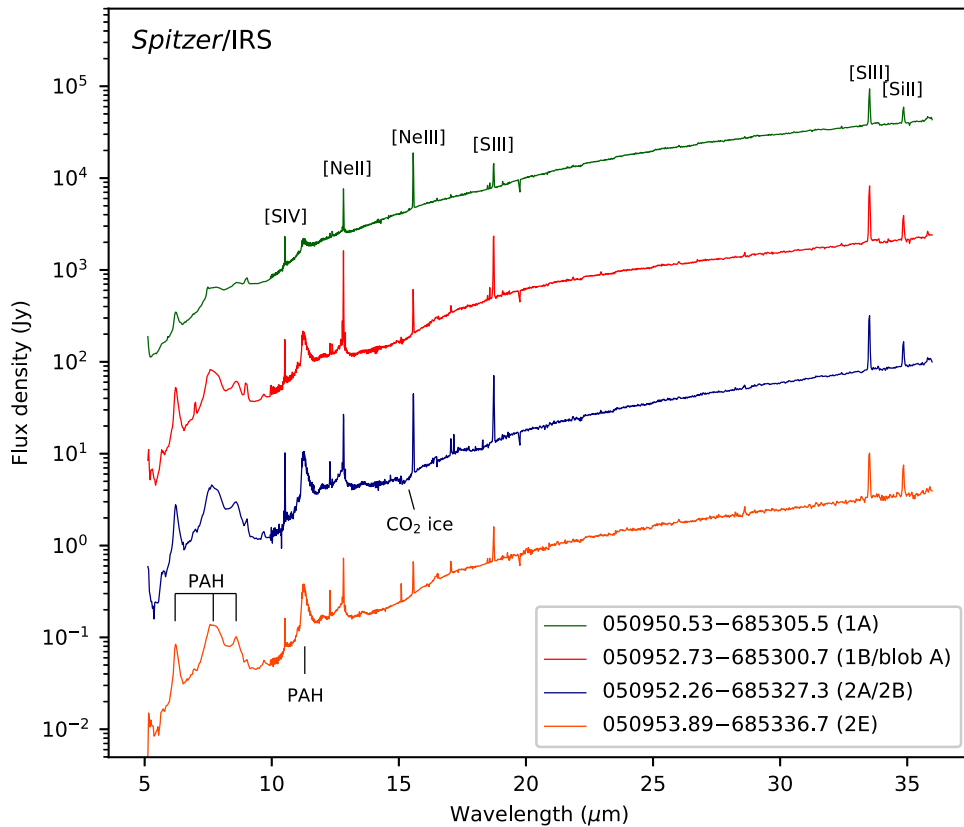


Figure 18. The Spitzer/IRS spectra of YSOs associated with ALMA continuum sources color-coded as indicated in the legend. PAH and CO₂ ice features and fine-structure lines are labeled. The spectra have been scaled by the following multiplicative factors for clarity (from bottom to top): 1, 12, 140, and 1000. All spectra were analyzed and classified in Seale et al. (2009) and Jones et al. (2017).

unambiguously classify more evolved YSOs. Furthermore, given the large and variable slit width across the IRS range (3''6/~0.9 pc at shorter to 11''1/~2.7 pc at longer wavelengths), point-source spectra can be contaminated by the ambient emission in the wider H II region, likely the case in N 105 (see Figures 1–2).

Given the new ALMA data we have obtained for N 105, we have revisited the analysis of these IRS spectra. In Figure 18, there is a hint of a broad absorption feature at ~15 μm in the spectrum of 2 A/2 B. Broad absorption features in the IRS spectra of YSOs are commonly attributed to solid-state (i.e., ice) features of abundant molecules like H₂O, CO₂, etc. (Oliveira et al. 2009, 2011; Seale et al. 2011; Oliveira et al. 2013); the feature at 15.2 μm is due to CO₂ ice.

Figure 19 shows the results of this new analysis. It closely follows that described in Oliveira et al. (2009, 2011, 2013). We first define a pseudocontinuum over the range 14–17 μm (using spectral regions free of absorption and emission lines) by fitting a low-degree polynomial (top). The spectrum and the fitted continuum are used to calculate the optical depth (bottom). The optical depth for N105–2 A/2 B is compared to that of a well-studied SMC YSO analyzed in Oliveira et al. (2013); the shape of these absorption features are very similar, except that of N 105–2 A/2 B lacks a red wing. While the shape of the CO₂ ice profile reflects composition and environmental conditions like the temperature (see the extensive discussion in Oliveira et al. 2009), in this case the presence of the strong emission line at 15.55 μm due to [Ne III] precludes any further analysis of the profile shape. For completeness, we analyzed the spectra of the

other three sources in the same way; no features attributable to CO₂ ice are detected.

The column density has been computed using the line strength $A = 1.1 \times 10^{-17} \text{ cm molecule}^{-1}$ (Gerakines et al. 1995). Column density calculations are dependent on the exact determination of the pseudocontinuum and can vary by as much as 25% (Oliveira et al. 2009); furthermore, for this particular spectrum, the relatively low signal-to-noise ratio and the aforementioned emission line make this determination difficult. We compute a CO₂ ice column density of $(2.63 \pm 0.14) \times 10^{17} \text{ cm}^{-2}$; the uncertainty is statistical only, and it does not take into account any uncertainties in the continuum determination. This column density is at the lower end of the ranges reported in Oliveira et al. (2009) and Seale et al. (2011, $\sim(1-17) \times 10^{17} \text{ cm}^{-2}$), and this is perhaps the reason why neither Seale et al. (2011) nor Jones et al. (2017) identified CO₂ ice in the spectrum of N 105–2 A/2 B.

6.2. KMOS Spectroscopic Results

The KMOS *H* + *K*-band spectra are available for three VMC sources in N 105 in the area covered by our ALMA observations. Their source catalog IDs are 558354728325, 558354728333, and 558354728291 (hereafter VMC 325, VMC 333, and VMC 291) and are located nearby ALMA 1.2 mm continuum sources N 105–1 A, N 105–2 B, and N 105–2 E, respectively. The KMOS spectra are shown in Figure 20; the detected spectral lines include the H I (with the brightest Br γ at 2.166 μm), He I (2.058 μm), and H₂ (2.122 μm) lines. No CO bandhead (2.3 μm) and fluorescent Fe II (1.688 μm) emission

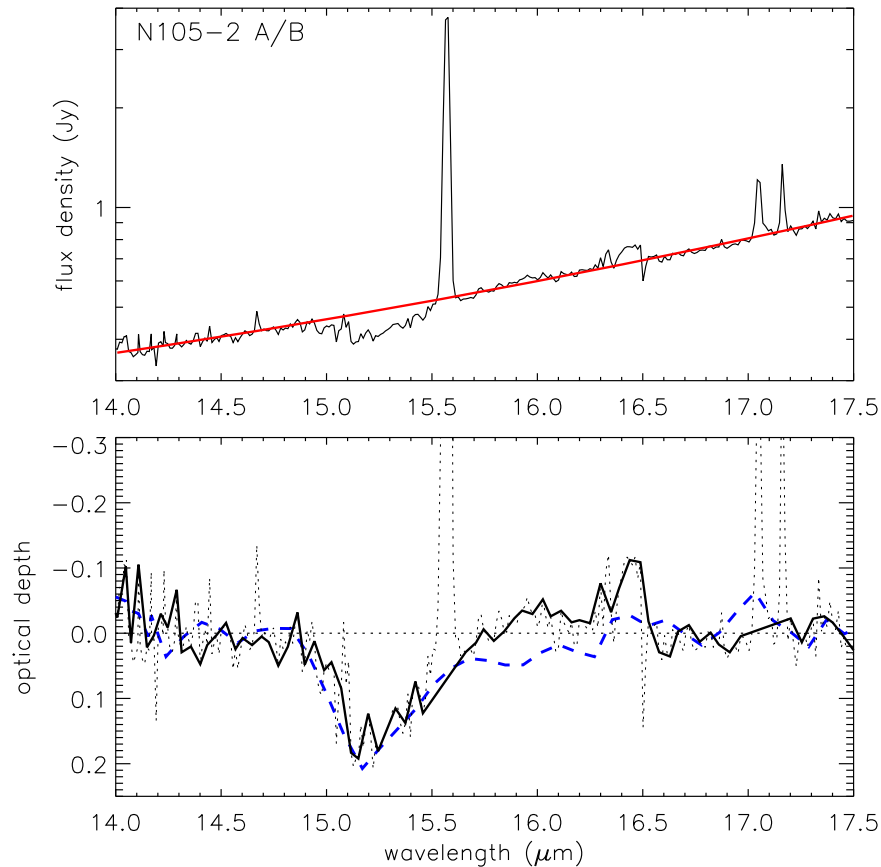


Figure 19. The top panel shows a zoom-in on the Spitzer/IRS spectrum for the YSO corresponding to the N 105–2 A/2 B continuum sources, covering the CO₂ ice band at 15.2 μm . The red solid line shows the continuum fit (a low-degree polynomial). The spectrum and the fitted continuum were used to calculate the optical depth. The dotted black line in the bottom panel shows the resulting optical depth spectrum for 2 A/2 B; the solid black line shows the same optical depth spectrum smoothed for ease of visibility. The blue dashed line shows the spectrum for a well-studied SMC YSO from Oliveira et al. (2013) roughly scaled to the same optical depth for guidance of the shape.

(tracing disks) or forbidden [Fe II] (1.644 μm) emission (tracing outflows) were detected. Figure 21 shows three color images of VMC 325, VMC 333, and VMC 291, combining the KMOS K -band continuum, Br γ , and H₂ images, with the ALMA 1.2 mm continuum contours overlaid.

To analyze the data, we followed the analysis outlined in Ward et al. (2016). Here, we include a brief summary of the data analysis methods, followed by a discussion of the results for individual sources. The extinction (A_V) values are calculated using the KMOS H - and K -band continuum measurements and are provided in Table 5. These were measured by fitting a third-order polynomial to the continuum spectrum, and the integrated flux of the polynomial was measured for the wavelength ranges 1.5365–1.7875 μm (H band) and 2.028–2.290 μm (K band; Equation (1) in Ward et al. 2016) and assuming an intrinsic $H - K$ color of -0.05 mag, corresponding to a B0 V star. We were unable to estimate A_V for VMC 333 (nearby 2 B), which has a very blue spectrum, indicating that it is not embedded. The value of A_V for VMC 325 (1 A; 42 ± 4 mag, Table 5) is in excellent agreement with that estimated by Oliveira et al. (2006) using the VLT/ISAAC spectrum (~ 40 mag; see Section 6). We applied the extinction correction to our measurements for VMC 325 (1 A) and VMC 291 (2 E) described below to constrain the physical properties of the observed sources.

The accretion luminosity (L_{acc}) was estimated from the Br γ luminosity ($L_{\text{Br}\gamma}$) assuming the relation of Calvet et al. (2004)

for intermediate-mass YSOs holds for high-mass YSOs in the LMC: $\log(L_{\text{acc}}) = -0.7 + 0.9(\log(L_{\text{Br}\gamma}) + 4)$. The accretion luminosities for VMC 325, VMC 333, and VMC 291 are listed in Table 5.

VMC 325: Figure 21 shows a good positional correlation between the VMC source VMC 325 and the ALMA N 105–1 A 1.2 mm continuum peak, indicating that the near-IR source observed with KMOS is the central protostar in 1 A. With A_V of 42 ± 4 mag, VMC 325 is the most embedded source of the three KMOS sources in the ALMA fields, with by far the reddest spectrum. The spectrum of VMC 325/1 A exhibits a full Brackett series emission in the $H + K$ bands, strong He I emission, and some considerably weaker H₂ emission.

The H₂ emission (tracing shocks) extends toward west-northwest from the continuum source (Figure 21), in agreement with the direction of the outflow reported in Oliveira et al. (2006) (see Section 6). The accretion luminosity of $(2.9_{-1.5}^{+0.9}) \times 10^5 L_{\odot}$ (see Table 5) is 2–3 orders of magnitude larger than those measured toward similar objects in the Magellanic Clouds (Ward et al. 2016, 2017; van Gelder et al. 2020). This high value of L_{acc} can be explained by a contribution from the bright UC H II region to the Br γ emission (e.g., Armand et al. 1996). This interpretation is supported by the fact that the Br γ emission is extended toward VMC 325 (see Figure 21).

VMC 333: The K -band continuum position of VMC 333 is offset by $\sim 0''.4$ (~ 0.1 pc or $\sim 20,000$ au) from the 1.2 mm

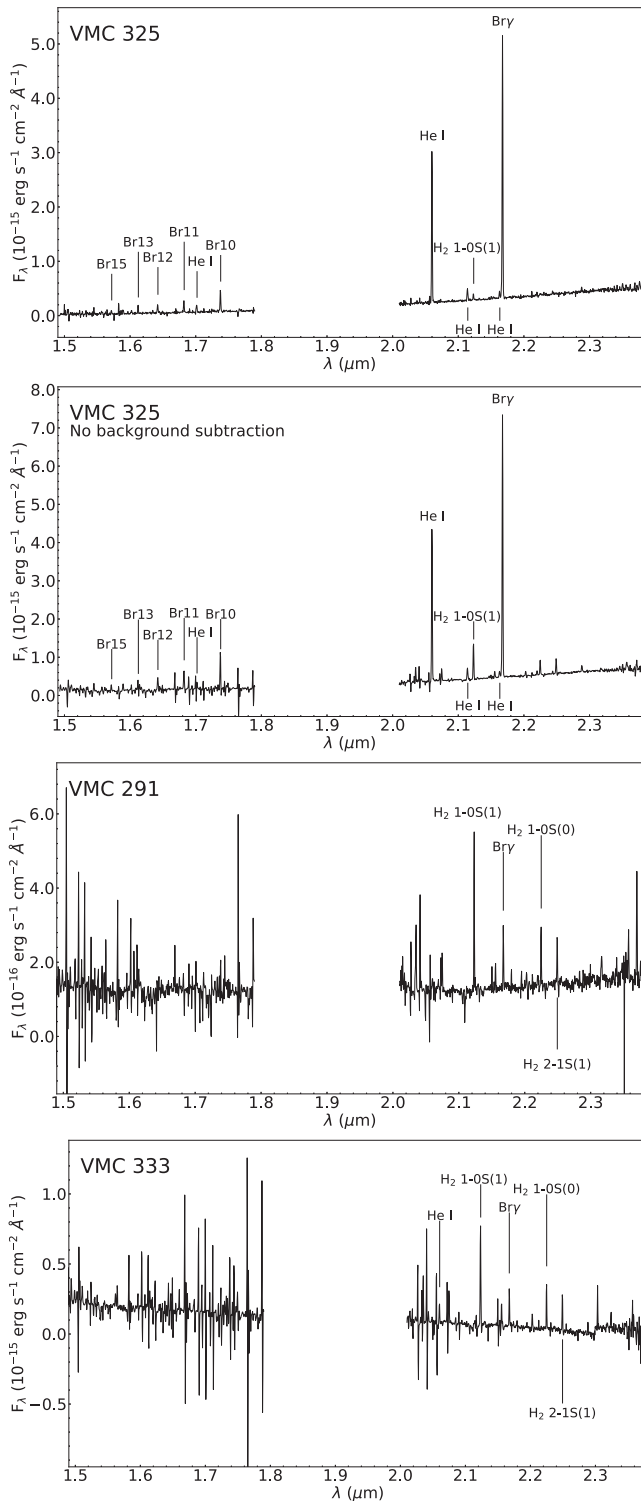


Figure 20. From top to bottom: VLT/KMOS $H + K$ spectra of the near-IR source VMC 325 (corresponding to the ALMA continuum source N 105–1 A) with and without background subtraction, and the background-subtracted spectra of VMC 333 (in the vicinity of 2 B) and VMC 291 (2 E).

continuum source N 105–2 B. VMC 333 has quite a blue spectrum and is unlikely to be deeply embedded. Figure 21 shows an extended $\text{Br}\gamma$ and H_2 emission in the region. Following background subtraction most of this emission is removed, but there is still $\text{Br}\gamma$ emission coincident with the source; thus, it seems likely that the source does contribute to

the emission, although it is unclear whether it is the dominant ionizing source. Assuming it is the dominant ionizing source, the accretion luminosity of VMC 333 is $(2.0 \pm 0.1) \times 10^2 L_\odot$.

The position of the closest Spitzer source to 2 B is offset by $\sim 0''.8$, i.e., the distance is 2 times larger than that between 2 B and VMC 333 (see Figures 4 and 17). The properties of this Spitzer source are uncertain; the Spitzer/IRS spectrum analyzed in Seale et al. (2009) and Jones et al. (2017) was obtained at a position between this source and another Spitzer source nearby 2 A seen in the images, and likely both sources contribute to the emission (see Sections 3.1 and 6.1). At longer Spitzer and Herschel wavelengths, these two sources remain unresolved with offsets between the emission peaks in different bands.

No K -band source has been detected with KMOS at the position of the 1.2 mm continuum source 2 F; the central source may be below a detection limit of the KMOS observations at the K band if it is very young. Mid- and far-IR observations matching the ALMA spatial resolution are needed to learn about the central sources in 2 B and 2 F.

The extended H_2 emission throughout the KMOS field is consistent with the ALMA data showing evidence for strong shocks toward 2 B (see Section 7.5). The brightest H_2 emission is located toward east and northeast from 2 B, but it is also present in the north and southeast. The distribution of the $\text{Br}\gamma$ emission is similar to H_2 , but it is the brightest in the north.

VMC 291: There is a very good positional correlation between VMC 291 and the 1.2 mm continuum source N 105–2 E, indicating that VMC 291 is the central protostar in 2 E (see Figure 21). VMC 291 has quite a red spectrum (not quite as red as VMC 325/1 A). The source is embedded with A_V of 12 ± 2 mag. The signal-to-noise ratio in the H -band spectrum of VMC 291/2 E is very poor; however, there is a clear detection of the $\text{Br}\gamma$ and H_2 emission lines in the K -band spectrum (see Figure 20). We have estimated the accretion luminosity for VMC 291 of $(2.3^{+0.5}_{-0.6}) \times 10^2 L_\odot$.

7. Discussion

7.1. Hot Cores and Hot Core Candidates

The physical and chemical properties of the continuum sources N 105–2 A and 2 B indicate that they are bona fide hot cores. Their rotational temperatures determined based on multiple tracers exceed 100 K (see Table 5), and their effective FWHM sizes are ~ 0.13 pc (Table 4), consistent with the definition of hot cores ($\lesssim 0.1$ pc; e.g., Kurtz et al. 2000). Slightly larger sizes of the LMC hot cores compared to Galactic hot cores are not surprising due to less dust, and as a result the radiation reaches further distances from the protostars (see also Sewilo et al. 2018). Both sources 2 A and 2 B show emission from COMs and are associated with the $\text{H}_2\text{O}/\text{OH}$ masers, as typically observed toward Galactic hot cores.

Figure 22 shows the bar histogram of rotational temperatures and column densities for bona fide hot cores 2 A and 2 B and several other sources from our sample exhibiting high temperature in at least one of the four tracers (CH_3CN , CH_3OH , SO_2 , and $^{34}\text{SO}_2$): 2 C, 2 F, 3 B, and 1 A. We consider these sources as “hot core candidates.”

Source 2 C with the high CH_3OH rotational temperature of ~ 95 K with an uncertainty of $\sim 25\%$ is likely a hot core; however, the SO_2 temperature is warm at ~ 32 K. If 2 C is indeed a hot core, the relatively low SO_2 temperature could be

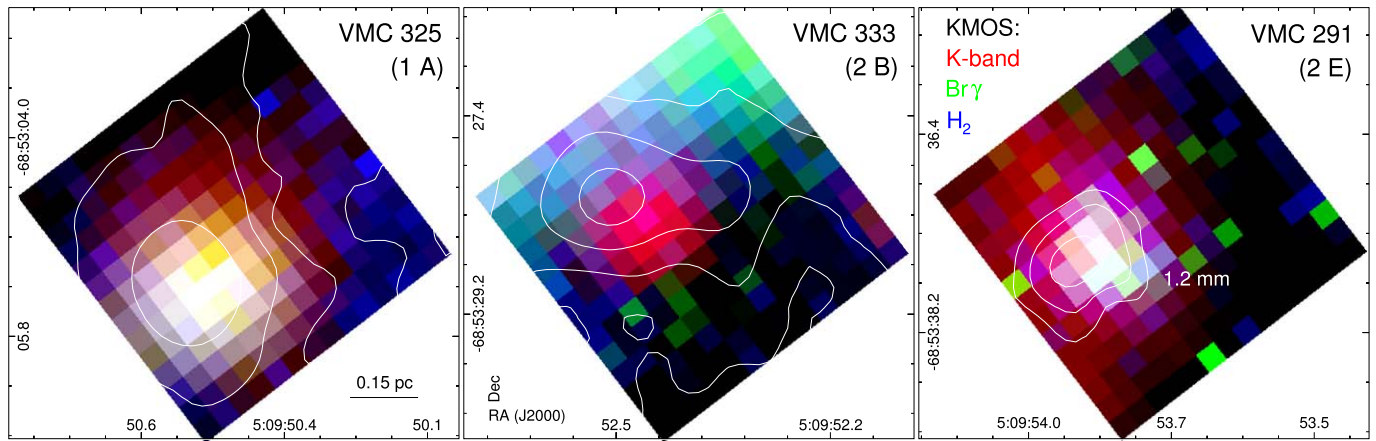


Figure 21. Three-color KMOS mosaics of VMC 325 (left), VMC 333 (center), and VMC 291 (right), combining the K -band (red), $\text{Br}\gamma$ (green), and H_2 (blue) images. The 1.2 mm continuum contours are overlaid for reference, and the name of the closest ALMA continuum source is indicated in each image; the contour levels are $(3, 10, 80)\sigma_1$, $(3, 10, 30, 80)\sigma_2$, and $(3, 5, 8)\sigma_2$ for 1 A, 2 B, and 2 E, respectively, where σ_1 (σ_2) is the rms noise in the N 105–1 (N 105–2) 1.2 mm continuum image. The size of the images is $2''.8 \times 2''.8$.

Table 5
VMC Photometry, Visual Extinction, and Accretion Luminosity for KMOS targets

Object	VMC Source ID	R.A. (J2000) (deg)	Decl. (J2000) (deg)	K_s (mag)	J (mag)	Y (mag)	A_V (mag)	L_{acc} (L_\odot)
VMC 325	558354728325	77.4605865	-68.8848206	13.837 (0.004)	42 ± 4	$(2.9_{-1.5}^{+0.9}) \times 10^5$
VMC 333	558354728333	77.4686862	-68.8912009	16.113 (0.014)	17.415 (0.026)	18.070 (0.036)	...	$(2.0_{-0.1}^{+0.1}) \times 10^2$ ^a
VMC 291	558354728291	77.4746443	-68.8937331	15.357 (0.009)	12 ± 2	$(2.3_{-0.6}^{+0.5}) \times 10^2$

Note.

^a Not corrected for extinction.

the result of blended hot and cold SO_2 components that could not be separated at the signal-to-noise ratio of our observations. Alternatively, the derived SO_2 temperature could be suppressed by non-LTE effects; however, it is unclear whether these non-LTE effects alone would explain the large difference in the rotational temperature between CH_3OH and SO_2 . CH_3CN is present toward 2 C, but only the $K=0$ component of the 14_K-13_K ladder has been reliably detected. The 2 F continuum peak located $\sim 1''$ to the west from source 2 B is likely a separate source and a hot core with the CH_3OH temperature of 127 ± 33 K. The CH_3OH temperature determination for 3 B has the highest uncertainty, 159_{-61}^{+41} K, but the source is associated with a CH_3OH maser. Multiple transitions for other species are not available to obtain an independent temperature measurement to confirm the results for 2 F and 3 B. The sizes of 2 C (~ 0.15 pc) and 3 B (~ 0.12 pc) are consistent with them being hot cores; 2 F is a compact source as well, but it is blended with 2 B.

Source 1 A is an embedded YSO that has started ionizing its immediate surroundings, and it is associated with an outflow (see Section 6). N 105–1 A is associated with cold CH_3OH (~ 12 K), but SO_2 has a rotational temperature of $\sim 96 \pm 20$ K. The SO_2 peak is offset from the 1 A 1.2 mm continuum peak by $\sim 0''.6$ (see Figure 9). The analysis of the spectrum extracted as a mean at half-peak of the SO_2 emission provided a similar result for the SO_2 temperature (98 ± 20 K) and slightly warmer CH_3OH (22 ± 4 K), which may be indicative of a more compact, hotter CH_3OH component centered on the hot SO_2 source. The SO_2 lines in the 1 A spectrum we analyzed may (at least partially) originate in the area offset from the continuum source and/or CH_3OH may be subthermally excited. The

region of the hot SO_2 emission may be a separate source—externally illuminated as no infrared source has been detected at this position, possibly associated with shocks from the 1 A outflow.

7.2. Hot and Cold CH_3OH and SO_2

Methanol is detected in all 12 continuum sources identified in the N 105 region. The bona fide hot cores, 2 A and 2 B, and the hot core candidates 2 C and 2 F, all contain both hot and cold CH_3OH components. Only hot CH_3OH is detected in the remaining candidate, 3 B, and only cold methanol is detected in the other seven sources. SO_2 also exhibits both hot and cold components in 2 A, 2 B, and 2 F.

The formation of CH_3OH by solid phase hydrogenation of CO ice is the only viable formation pathway in interstellar chemistry (e.g., Herbst & van Dishoeck 2009), thus all the detected CH_3OH originates from a prior cold phase when hydrogenation of CO molecules occurred on grain ice mantles. These molecular ices, containing primarily H_2O , CO, CO_2 , CH_4 , NH_3 , and CH_3OH (e.g., Boogert et al. 2015), were subsequently released, wholly or partially, into the gas. For the hot cores, the mantles can be removed by thermal desorption from dust heated by the protostar and/or sputtering in shock waves associated with outflows (e.g., Jørgensen et al. 2020). Either mechanism could account for the presence of the hot CH_3OH component, but the presence of SiO emission, resulting from the sputtering of refractory dust material (e.g., Schilke et al. 1997), confirms the role of shock waves in producing the hot CH_3OH component in 2 A–C and 2 F.

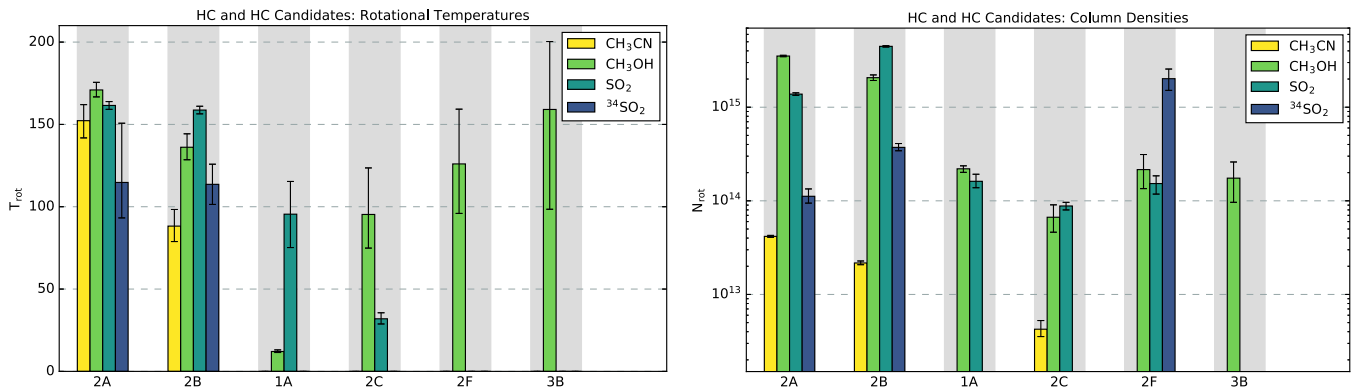
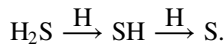
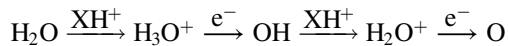


Figure 22. Rotational temperatures (left) and column densities (right) of hot cores (2 A and 2 B) and hot core candidates (1 A, 2 C, 2 F, and 3 B) in N 105 determined by spectral modeling for molecular species with the detection of multiple transitions—CH₃CN, CH₃OH, SO₂, and ³⁴SO₂ (where available; see Section 4.3 and Table 6). To calculate column densities for hot core candidates for species with no independent temperature determination, the CH₃OH temperature was assumed.

In hot cores where the chemistry is initiated by shock waves, cooling of the postshock gas is rapid, the temperature approaches that expected from thermal balance determined by protostellar radiative heating, and the long-term chemical evolution closely approaches the predictions of pure thermal desorption models (Charnley & Kaufman 2000). The derived temperatures in the N 105 hot cores, ~ 95 – 170 K, suggest that their observed composition could be explained by simple models of postevaporation chemistry. For example, H₂O and H₂S injected from grain mantles can drive the production of S-bearing molecules, such as SO and SO₂ (Charnley 1997). Hydrogen atom abstraction reactions with H₂S are endoergic but can proceed in hot gas to produce SH and atomic S



Protonation of H₂O by molecular ions (XH⁺ = H₃⁺, HCO⁺) followed by electron dissociative recombination reactions can release OH and then atomic O



and lead to SO and SO₂ through



with an additional contribution to SO formation from reaction of atomic S with OH. Reformation of H₂O and H₂S in reactions of H₂, with each of O, OH, S and SH, is inhibited below about 250 K (Charnley 1997).

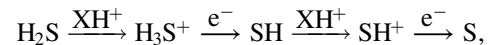
In 2 D, SiO is also detected but the cold CH₃OH gas is accompanied by a warm component (~ 31 K), significantly less abundant and much cooler than in higher-temperature cores. However, the SiO abundance is ~ 8 – 30 times less abundant than in the hot CH₃OH cores, perhaps indicating the presence of lower sputtering yields in weaker shocks. Less efficient sputtering of ices means less H₂S and H₂O injected into the gas, lower abundances of SH and OH, and hence may also account for the nondetection of SO₂ in 2 D.

Molecular desorption from ice mantles is most probably also the origin of the cold gas detected in CH₃OH and, indirectly, in SO₂. However, it is less clear exactly how these ice mantles were deposited into the gas, considering that the inferred dust temperatures are far too low (~ 10 – 17 K) to allow thermal desorption. The same unresolved issue arises in Galactic dark clouds, where emission from water, methanol, and other complex molecules is detected in dense clumps at locations far

from protostars or any outflows (e.g., Bacmann et al. 2012; Cernicharo et al. 2012; Vastel et al. 2014; Wirström et al. 2014; Taquet et al. 2017; Soma et al. 2018; Agúndez et al. 2021).

Several desorption mechanisms have been proposed and include photodesorption, explosion of UV-irradiated ices, grain heating following cosmic-ray impact (Leger et al. 1985), cosmic-ray sputtering (Wakelam et al. 2021), as well as “reactive desorption” in which the energy released in exothermic grain-surface reactions is sufficient to overcome the physisorption binding energy (Minissale et al. 2016; Chuang et al. 2018). Alternatively, a localized kinematic origin has been proposed for the origin of methanol and other putative ice-mantle molecules in Galactic dark clouds. This involves transient heating of dust grains in low-velocity grain–grain collisions. The center-of-mass kinetic energy resulting from drift velocities of $\lesssim 1$ km s^{−1} heats the grains, which then cool by evaporation of surface molecules. Relative grain–grain streaming could occur through wave motions (Markwick et al. 2001), in merging collisions between small clumps or filaments (Dickens et al. 2001; Buckle et al. 2006; V. Taquet 2022, in preparation), or in fluid dynamical instabilities (Harju et al. 2020).

These mechanisms could also lead indirectly to SO and SO₂ in cold gas via the neutral processes described above: if H₂S is also desorbed from the ices, SH and S can still be produced through protonation and dissociative electron recombination



even though H₂S destruction by H atoms is inefficient. Model calculations based on the grain-streaming picture are able to explain the observed close spatial correspondence between CH₃OH and SO in maps of several dark clouds (Buckle et al. 2006).

Thus, the origin of the cold methanol, as well as of SO and SO₂, could in principle be due to several processes. For the cold CH₃OH found in N 105, photodesorption is very unlikely due to the high visual extinctions and because ice photolysis experiments indicate that CH₃OH dissociates on desorption (Bertin et al. 2016; Martín-Doménech et al. 2016). Processes involving cosmic rays or reactive desorption may be expected to produce extended, almost homogenous, CH₃OH distributions. We find that cold CH₃OH emission is widespread in N 105–1 A relative to other sources, and this may reflect a higher cosmic-ray flux in this field. It is difficult to estimate the cosmic-ray flux necessary to explain the cold CH₃OH emission

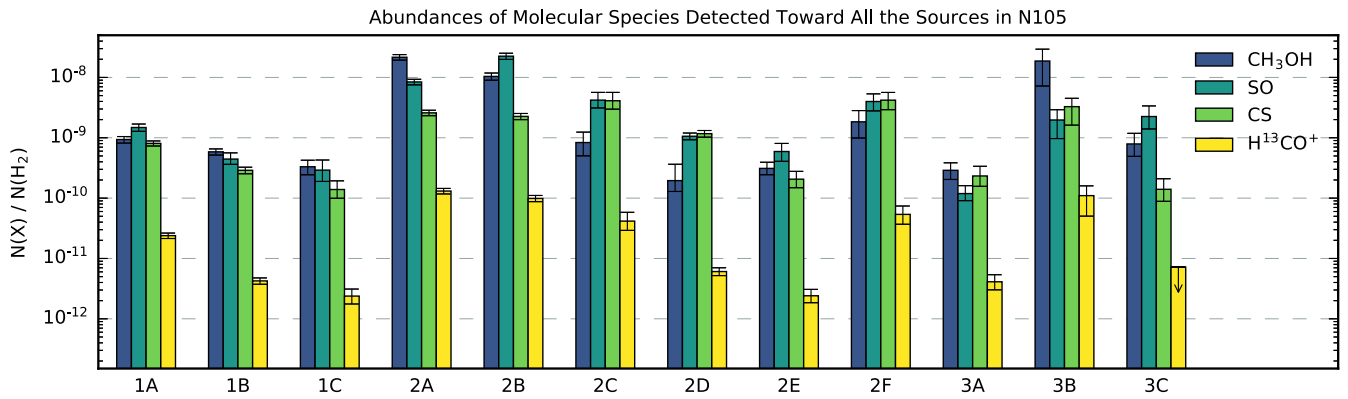


Figure 23. Comparison of the CH_3OH , SO , CS , and $H^{13}CO^+$ abundances between all the continuum sources in N 105. CH_3OH , SO , CS , and $H^{13}CO^+$ are the only molecules detected toward all the sources.

as this requires knowledge of the cosmic-ray composition, the manner in which the grain is heated (whole-grain versus spot heating), as well as whether a radical explosion can be initiated (e.g., Leger et al. 1985). A markedly higher cosmic-ray flux in N 105–1 should have consequences for other molecules. In N 105–1, we only detect simpler molecules that most likely originate in gas-phase reactions. Of these, $H^{13}CO^+$ would be most sensitive to the cosmic-ray ionization rate. The fact that the derived $H^{13}CO^+$ abundances in N105-1 are lower than toward most of the sources in N 105–2 and N 105–3 probably rules out the cosmic-ray desorption mechanism as the important contributor to the production of the cold CH_3OH emission.

If reactive desorption of CH_3OH upon surface formation produced the widespread cold CH_3OH emission in N 105–1 A, it is difficult to understand why it is also not evident in N 105–2 and N 105–3. For cores where the cold CH_3OH emission is more compact, grain collisions could be responsible for mantle desorption; evaluating this contribution will require a detailed understanding of the kinematics and higher angular resolution observations to probe structures (clumps, filaments) not resolved in our ALMA observations.

7.3. Molecular Abundances: N 105

In Figures 23 and 24, we compare the fractional abundances with respect to H_2 for all the 1.2 mm continuum sources in N 105, calculated as described in Section 5. Figure 23 shows the bar histogram for the species detected toward all the sources: CH_3OH , SO , CS , and $H^{13}CO^+$. The largest differences between the sources are observed in $H^{13}CO^+$.

In Figure 24, we separately compare fractional abundances of COMs, N-bearing species, S-/O-bearing species and SiO, and C-/S-bearing species. In general, N 105–2 is the most chemically rich region with the detection of COMs other than CH_3OH and the highest fractional abundances of other species; the only exception is SO and CS , which have comparable abundances toward the hot core candidate 3 B. The fewest number of species has been detected toward the continuum sources in N 105–3, but those detected have fractional abundances comparable to those observed toward other fields, indicating a smaller size or lower density for these sources, resulting in reduced emission line strengths. N-bearing species have lower abundances than S-bearing species in all three ALMA fields.

Sources 2 A, 2 B, and 2 C are the only sources in the N 105 ALMA fields with detection of CH_3CN . Recently, Mininni et al. (2021) analyzed the CH_3CN data for a sample of high-mass star-forming regions at different evolutionary stages (high-mass starless cores, high-mass protostellar objects, and UC H II regions) and concluded that the mean abundance of CH_3CN is a good tracer of the early stages of high-mass star formation; it shows 1 order of magnitude increase from starless cores to later evolutionary stages. In the LMC, we can use this result to investigate the relative ages of sources with the detection of CH_3CN . The lowest CH_3CN abundance was measured toward 2 C: 2 times lower than that observed toward 2 B and 5 times lower than for 2 A. Thus, 2 C appears to be the youngest of the three sources, which is consistent with its location in the optical dark lane and a lack of an IR match in the available data.

The continuum source A in N 105–1 is the only source in our ALMA fields with the detection of H recombination lines, indicating the presence of ionized gas. It is still an embedded protostar, but it has already started ionizing its surroundings. N 105–2 appears to be the site of the most vigorous ongoing star formation with multiple maser sites, a YSO with the detection of the CO_2 ice band, and the presence of COMs, hot cores, and deuterated species. In the south, hot core candidate N 105–3 B is associated with 6.7 and 12.2 GHz CH_3OH masers. These are radiatively excited Class II masers known to be tracers of a very early phase of massive star formation (e.g., Cragg et al. 1992; Ellingsen 2006). It is plausible that the source is at the early hot core phase and thus not all hot core tracers (such as SO_2) have achieved detectable levels.

7.4. Tentative Detection of Formamide in a Low-metallicity Environment

Formamide (NH_2CHO) is the simplest naturally occurring amide and has been proposed as a precursor of prebiotic molecules with a key role in the emergence of life on Earth (see López-Sepulcre et al. 2019 for a review). We detected the NH_2CHO $12_{2,10}-11_{2,9}$ transition at 260.189 GHz (the strongest NH_2CHO line in the observed spectral range) at a 3.2σ level toward hot core N 105–2 A. The statistical uncertainty of our NH_2CHO detection takes into account the uncertainty in the emission due to the contribution of the overlapping CH_2CO transition at 260.192 GHz to the detected line flux. Since our identification of NH_2CHO is based on a single, low signal-to-noise ratio transition, which is blended with another line, we

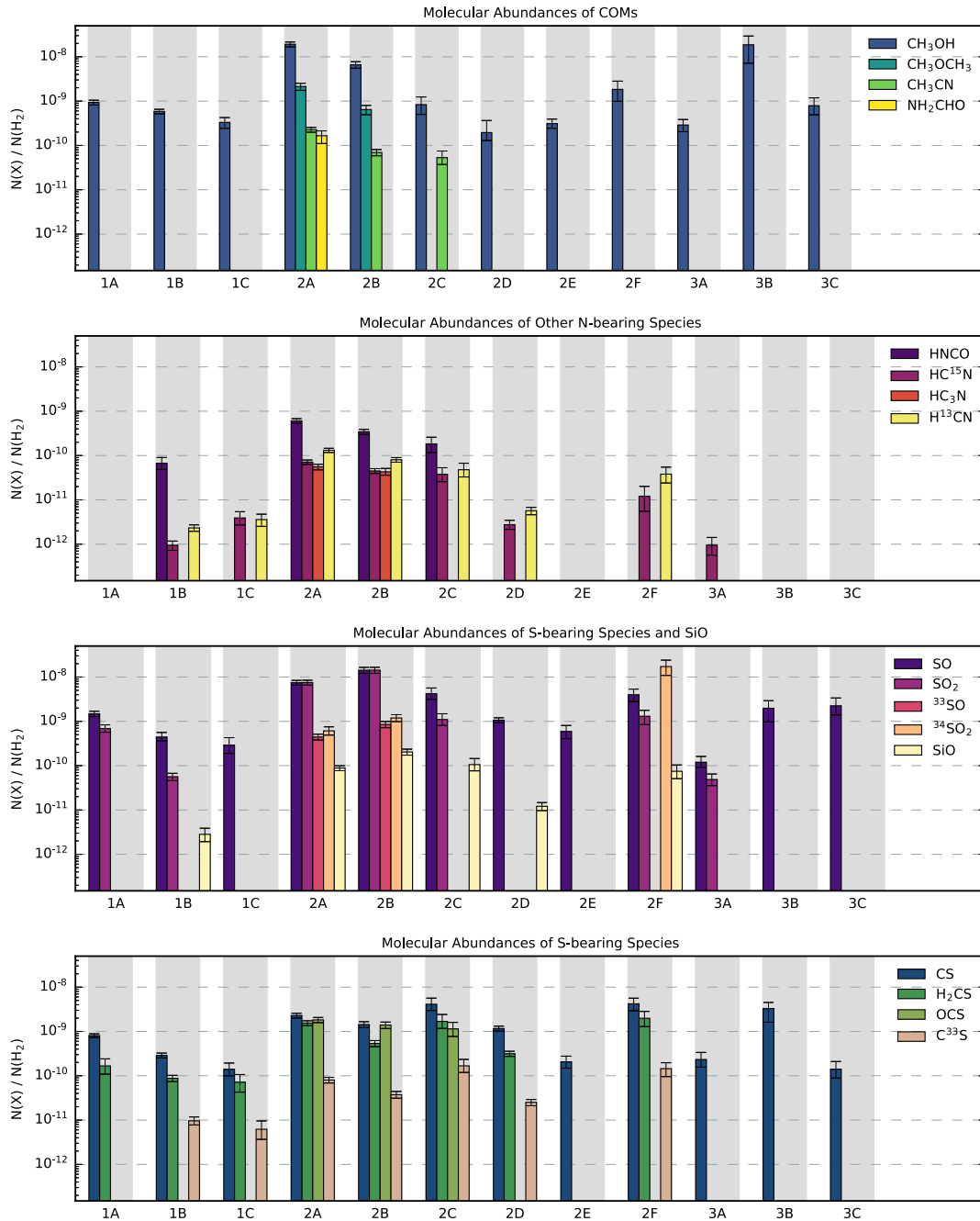


Figure 24. Comparison of molecular abundances between all the 1.2 mm continuum sources detected in N 105 with ALMA (from top to bottom): COMs (CH_3OH , CH_3OCH_3 , CH_3CN , and NH_2CHO); simple N-bearing species ($HNCO$, $HC^{15}N$, HC_3N , and $H^{13}CN$); S-bearing species (SO , SO_2 , $^{33}SO_2$, and $^{34}SO_2$) and SiO ; other S-bearing species (CS , H_2CS , OCS , $C^{33}S$). In terms of the number of detected species and molecular abundances, N 105–2 is the most chemically rich ALMA field in N 105.

can only consider this detection as tentative. If the presence of NH_2CHO in the LMC is confirmed, it will constitute the first detection of this astrobiologically relevant molecule in the extragalactic low-metallicity environment.

Based on the CH_3OH rotational temperature, N 105–2 A is the hottest of the sources observed in N 105, which is likely the reason for the detection of gas-phase NH_2CHO only in this core. NH_2CHO has one of the highest physisorption binding energies of the most common interstellar COMs (including CH_3OH ; Penteado et al. 2017). Lower maximum dust temperatures could account for its nondetection in the other sources in N 105.

The formation routes of NH_2CHO are still debated. It may proceed via gas phase pathways involving H_2CO and NH_2 (e.g., Barone et al. 2015; Skouteris et al. 2017) and/or grain surface reactions involving hydrogenation of $HNCO$ (e.g., Charnley & Rodgers 2008); although laboratory studies indicate that the latter route may not be viable (e.g., Noble et al. 2015; López-Sepulcre et al. 2019 and references therein). Observations show that NH_2CHO is most abundant in the hot parts of protostellar envelopes ($T > 100$ K; hot cores: e.g., Allen et al. 2017; Bisschop et al. 2007; hot corinos, similar to hot cores but formed around low- and intermediate-mass protostars: e.g., López-Sepulcre et al. 2015; Marcelino et al. 2018; Bianchi et al. 2019) and regions

dominated by shocks (e.g., in protostellar outflows; e.g., Yamaguchi et al. 2012; Mendoza et al. 2014; Ceccarelli et al. 2017; Codella et al. 2017). It has not been established yet whether the formation route of NH_2CHO depends on the environment, although gas-phase reactions seem to be the dominant pathway leading to NH_2CHO in the protostellar outflows (e.g., Codella et al. 2017). Observations of NH_2CHO in the LMC offer unique tests of its formation models in the metal-poor environments with lower dust content and higher UV radiation fields. While our observations do not provide enough information to draw reliable conclusions, we have attempted a preliminary investigation of the NH_2CHO formation routes in the LMC.

Our observations did not cover any H_2CO lines, but we detected HNC toward 2 A. The NH_2CHO and HNC fractional abundances with respect to H_2 for 2 A are $X(\text{NH}_2\text{CHO}) = (1.7_{-0.6}^{+0.5}) \times 10^{-10}$ and $X(\text{HNC}) = (5.4 \pm 0.7) \times 10^{-10}$, respectively (see Table 6). One of the methods used to test the dominant formation route of NH_2CHO is to investigate its abundance correlation with other molecules that are thought to be chemically linked (i.e., forming from a common precursor or one forming from the other). Almost a linear correlation over several orders of magnitude in the fractional abundances was found for NH_2CHO and HNC in the Milky Way (e.g., López-Sepulcre et al. 2019). We can test whether the fractional abundances observed toward 2 A follow the $X(\text{NH}_2\text{CHO}) - X(\text{HNC})$ correlation found for Galactic sources by estimating the expected $X(\text{NH}_2\text{CHO})$ from the observed $X(\text{HNC})$ and comparing it to the observed value (after correcting both observed values for a difference in metallicity, assuming $Z_{\text{LMC}} = 0.5 Z_{\odot}$). The observational correlation (power-law fit) that holds for sources with NH_2CHO detection (no upper limits) is available in literature: $X(\text{NH}_2\text{CHO}) = 0.04X(\text{HNC})^{0.93}$ (López-Sepulcre et al. 2015), resulting in an expected $X(\text{NH}_2\text{CHO})$ for 2 A of $\sim 1.8 \times 10^{-10}$ based on the observed, metallicity-corrected $X(\text{HNC})$. The observed, metallicity-corrected $X(\text{NH}_2\text{CHO})$ ($\sim 3.4 \times 10^{-10}$) is a factor of ~ 1.9 higher than the expected value but still within the scatter of the $X(\text{NH}_2\text{CHO}) - X(\text{HNC})$ relation. The $X(\text{NH}_2\text{CHO}) - X(\text{HNC})$ correlation observed toward Galactic sources may not come from a direct chemical link between HNC and NH_2CHO , but rather be the result of their similar response to the temperature of their environment (e.g., Quénard et al. 2018).

Using the ALMA Band 6 and Band 7 observations, Shimonishi et al. (2021) have recently detected multiple transitions of NH_2CHO toward the submillimeter continuum source SMM1 in the WB89–789 star-forming region in the extreme outer Galaxy. WB89–789 SMM1 is located at the galactocentric distance of 19 kpc where metallicity (traced by the oxygen abundance) is expected to be a factor of 4 lower than in the solar neighborhood (e.g., Fernández-Martín et al. 2017; see Shimonishi et al. 2021 and references therein). Shimonishi et al. (2021) found that even though WB89–789 SMM1 and hot cores in the LMC represent low-metallicity environments, there is no resemblance between the extreme outer Galaxy and the LMC sources. The authors suggest that the dissemblance might be a result of differences in the environments such as the strength of the interstellar radiation field, which is significantly higher in the LMC (see Section 1).

Shimonishi et al. (2021) determined $X(\text{NH}_2\text{CHO})$ of $(1.8 \pm 0.1) \times 10^{-11}$ and $X(\text{HNC})$ of $(2.7 \pm 0.8) \times 10^{-10}$ for WB89–789 SMM1 for physical scales corresponding to those

probed by the ALMA observations of the LMC hot cores (0.1 pc), which is 1 order of magnitude lower than $X(\text{NH}_2\text{CHO})$ estimated for 2 A. The expected value of $X(\text{NH}_2\text{CHO})$ based on the $X(\text{NH}_2\text{CHO}) - X(\text{HNC})$ correlation of López-Sepulcre et al. (2015) for metallicity-corrected $X(\text{HNC})$ measured toward WB89–789 SMM1 is $\sim 5.3 \times 10^{-11}$. This value is a factor of ~ 1.4 lower than the metallicity-corrected observed $X(\text{NH}_2\text{CHO})$ ($\sim 7.2 \times 10^{-11}$)—a result similar to that we obtained for 2 A.

Figure 27 shows that the abundance of NH_2CHO in 2 A is higher than those measured toward the Orion Hot Core and Sgr B2(N) in single-dish observations (see a discussion in Section 7.7). There are, however, single-dish measurements of $X(\text{NH}_2\text{CHO})$ toward Galactic hot cores, which are 1 order of magnitude higher than $X(\text{NH}_2\text{CHO})$ in 2 A. For example, Bisschop et al. (2007) measured $X(\text{NH}_2\text{CHO})$ of a few times 10^{-9} for six hot cores: G24.78+0.08, G75.78+0.34, NGC 6334 IRS1, NGC 7538 IRS1, W3(H₂O), and W33 A; these values are 1–2 orders of magnitude higher than $X(\text{NH}_2\text{CHO})$ reported in the literature for the same sources.

The NH_2CHO transition in the spectrum of 2 A is blended with a CH_2CO $13_{1,13}-12_{1,12}$ line at 260.192 GHz (a frequency/velocity shift of ~ 2.9 MHz/ ~ 3.3 km s⁻¹; see Table 3), making the measurements of the NH_2CHO column density and abundance less reliable. We have investigated the $\text{NH}_2\text{CHO}-\text{CH}_2\text{CO}$ line blending issue in detail based on other CH_2CO transitions detected in our observations: the CH_2CO line at 244.712 GHz (Table 3) and two weak lines at 242.375 and 242.398 GHz ($<3\sigma$ detections), which helped constrain the fit.

While the formation on grains is the most likely scenario for CH_2CO , a gas-phase formation route is also possible (e.g., Bisschop et al. 2007). The NH_2CHO emission peak is offset from the HNC peak in 2 A ($\sim 0''.14$ or ~ 0.034 pc/ ~ 7000 au at 50 kpc), but it is also not coincident with the CH_2CO peak. Observations of additional transitions of NH_2CHO are needed to confirm our tentative detection and to conduct a more reliable investigation of the spatial correlation between the NH_2CHO and HNC emission that would allow us to test the NH_2CHO grain-surface formation scenario in the significantly different chemical laboratory of the LMC. Observations of H_2CO and NH_2 , when compared to the NH_2CHO data, would help test the gas-phase NH_2CHO formation route proposed by Barone et al. (2015) in which H_2CO and NH_2 are its precursors. Interstellar NH_2 was detected from the ground in Sgr B2 (van Dishoeck et al. 1993) and could be observed with ALMA. In addition, the abundance ratio of the deuterated forms of NH_2CHO can provide a strong constraint on its formation route (e.g., Coutens et al. 2016; López-Sepulcre et al. 2019).

7.5. Chemical Differences between Hot Cores N 105–2 A and B

The integrated intensity images of N 105–2 and the spectra of individual continuum components reveal differences in the chemical makeup of hot cores 2 A and 2 B, which are separated by $\sim 3''.2$ (~ 0.78 pc/ $\sim 160,000$ au). N-bearing species and deuterated species have higher abundances toward 2 A (up to a factor of ~ 2 for CH_3CN and HDO), while S-bearing species and SiO have higher abundances toward source 2 B (by a factor of $\sim 3-4$). The hot SO_2 abundance is larger in 2 B than in any other LMC hot core observed to date. NH_2CHO and HDCHO have only been detected toward source 2 A. Finally, the kinematic structure observed toward 2 B is much more

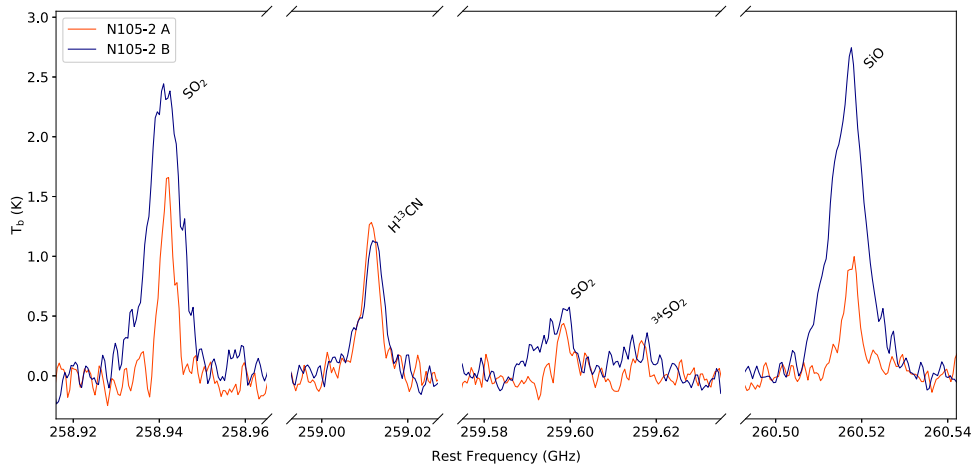


Figure 25. A comparison between the line profiles of selected S- and N-bearing species, as well as a shock tracer SiO detected toward the N 105-2 A and 2 B hot cores.

complex than that in 2 A, indicating the presence of at least two velocity structures.

In general, spectral lines for all the species are broader toward 2 B than 2 A, indicating the presence of more significant large-scale motions in this region. The difference in line widths, as well as line intensities, is particularly striking for SO, ^{33}SO , SO_2 , $^{34}\text{SO}_2$, and SiO (see Figure 25). The enhanced abundance of S-bearing species and SiO toward 2 B indicates the shock origin of some of the emission, consistent with the observed greater kinematic complexity, which is reflected in the broad line profiles. The enhanced production of the S- and Si-bearing molecules in shocks is a result of sputtering or destruction of refractory grain cores that release the Si and S atoms to the gas, making them available for chemical reactions (e.g., Schilke et al. 1997; Gusdorf et al. 2008; van Dishoeck 2018 and references therein; see also a discussion in Section 7.2).

Other species that are often detected in low-velocity outflows have broader lines toward 2 B than 2 A; these include the ice chemistry products such as CH_3OH , CH_3CN , HNCO , and HDO that can be released to the gas by shock-driven sublimation in addition to thermal sublimation in the hot core region (e.g., van Dishoeck 2018; Öberg & Bergin 2021), as well as H^{13}CN that can be produced via the hot-gas-phase chemistry in the cavity walls (e.g., Bruderer et al. 2009). Rotation of the envelope can also broaden spectral lines, but we are not able to distinguish between the outflow and rotation based on our relatively low-spatial-resolution data. Molecular species with narrower lines mostly originated in the more quiescent hot core region. All these processes most likely take place in 2 A as well but are not as much affected by complex kinematics as in 2 B; since the temperature is higher in the 2 A hot core (two times for CH_3CN), the thermal evaporation of grain ice mantles is more efficient in this region, resulting in higher or comparable fractional abundances for all molecules except the S- and Si-bearing species.

7.6. Molecular Abundances: N 105 versus Other LMC Hot Cores with COMs

In Figure 26, we compare the fractional abundances with respect to H_2 for the LMC hot cores with COMs from literature (N 113 A1 and B3, Sewilo et al. 2018; ST16, Shimonishi et al. 2020) and the newly identified hot cores in N 105: 2 A and 2 B.

We reanalyzed the spectra of N 113 A1 and B3 using the same spectral extraction and modeling techniques and the subsequent analysis for N 113 A1/B3 as for hot cores and other sources in N 105 and obtained results consistent with those reported in Sewilo et al. (2018); the results are listed in Table 6.

As described in Section 5, we adopted $T(\text{CH}_3\text{CN})$ for hot cores N 105-2 A and 2 B to calculate $N(\text{H}_2)$. For ST16, we recalculated the molecular abundances from Shimonishi et al. (2020) by estimating $N(\text{H}_2)$ using the dust temperature of 60 K provided in the paper (consistent with $T(\text{CH}_3\text{CN})$ of 53_{-7}^{+10} K) and assuming the same LMC dust-to-gas ratio as for N 105 and N 113 (Section 5). $T(\text{CH}_3\text{OH})$ is the only temperature determination available for hot cores A1 and B3 in N 113, and it was used for the analysis.

Figure 26 compares fractional abundances of COMs detected toward at least two LMC hot cores (CH_3OH , CH_3OCH_3 , HCOOCH_3 , and CH_3CN) and simple molecules that were observed toward all of the sources (SO_2 , OCS , ^{33}SO , and SiO). N 113 A1 and B3 hot cores represent a class of “organic-rich” hot cores, while ST16 is an example of an “organic-poor” hot core as defined by Shimonishi et al. (2020); see Section 1.

It is evident from Figure 26 that N 113 A1 and B3 remain the LMC hot cores with the highest abundance of CH_3OH with respect to H_2 , the only detection of HCOOCH_3 , and the most reliable detection of CH_3OCH_3 . The CH_3OCH_3 lines detected toward N 105-2 A and 2 B have low signal-to-noise ratios, and thus the molecular abundance calculations are less reliable. As discussed above, the enhanced abundances of SiO and SO_2 toward N 105-2 B are likely the results of the strong shock activity in the region. The SiO abundance toward N 113 B3 is even higher; similarly to 2 B, the environment of this source is highly dynamic. There are no large variations in the OCS abundance between the known LMC hot cores. The local environment appears to have a significant impact on the observed molecular abundances.

Figure 26 demonstrates that N 105-2 A and 2 B are chemically more similar to the organic-rich hot cores A1 and B3 in N 113 than to ST16 and the other organic-poor hot core ST11 where no COMs were detected (Shimonishi et al. 2016b). In the following section, we compare the fractional abundances of the species detected toward N 105-2 A and 2 B to those detected toward several representative Galactic hot cores to confirm their classification as organic-rich hot cores. It is

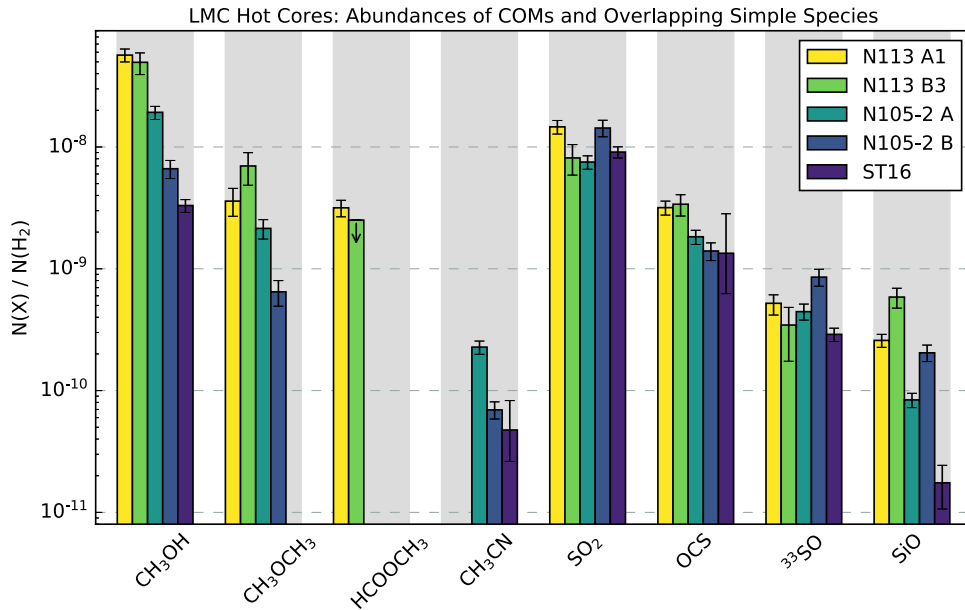


Figure 26. Comparison of COM abundances, as well as abundances of simple species detected toward hot cores N 113 A1 and B3, N 105–2 A and 2 B, and ST16. ST16 represents “organic-poor”, while the remaining sources represent the “organic-rich” hot cores (see text for details). CH_3CN lines were not covered by ALMA observations of N 113; the program was designed for a different science goal, and the detection of COMs was serendipitous.

expected that in general the fractional abundances of the molecular species observed toward the organic-rich hot cores scale with metallicity.

7.7. Comparison to Galactic Hot Cores

To compare the fractional molecular abundances derived for the LMC hot cores to those observed toward the Galactic hot cores, we first correct them for a difference in metallicity between these two galaxies. For this analysis, we adopt a mean metallicity of -0.30 ± 0.08 dex (i.e., half of that observed in the solar neighborhood; based on the abundance of O and Si) estimated by Rolleston et al. (2002) based on the analysis of all the classes of objects used to trace the chemical composition of the ISM in the LMC (e.g., H II regions, F-type supergiants, Cepheids, and B-type giants/bright giants), which is in agreement with a metallicity of -0.31 ± 0.04 they determined based on the young B-type dwarfs. This is also consistent with the metallicity determination based on the Fe abundance measured toward F-type supergiants (e.g., Russell & Dopita 1992 and references therein) and Cepheids (e.g., Luck et al. 1998). The overall conclusions presented in this section do not change for a lower value of Z_{LMC} of $0.4 Z_{\odot}$ found in some studies (see, e.g., Maeder et al. 1999 and references therein).

To correct the fractional abundances measured toward the LMC hot cores for a difference in metallicity between the LMC and the Galaxy, we have multiplied them by a factor of $1/Z_{LMC}$. This simple scaling does not take into account individual elemental abundances; in the LMC, the C, O, and N elemental abundances are lower than in the Galaxy by factors of 2.45, 2.19, and 4.83, respectively (Russell & Dopita 1992). While the individual elemental abundances matter, it is not clear without detailed physicochemical modeling (out of scope of the present paper) how multimetal species should be scaled with the metallicity. The scaling of these species by the product of their metal abundances may be correct for the molecules

formed in the gas phase; however, for those species that form on dust grains it only depends on the grain abundance (a total surface area available for chemistry) and the abundance of the least abundant atom.

The metallicity-corrected molecular abundances for N 105–2 A and 2 B, as well as hot cores in N 113, are compared to the abundances observed toward selected Galactic hot cores in Figure 27. We compare our observations to the single-dish observations of the Orion Hot Core, W3(H₂O), and Sgr B2(N) that trace similar physical scales—within a factor of a few of the physical scales probed by our LMC ALMA observations. The data for the Orion Hot Core come from Sutton et al. (1995) where available, otherwise the fractional abundances from Blake et al. (1987) are plotted (CH_3CN , HNC, and HDO). The data for W3(H₂O) and Sgr B2(N) come from Helmich & van Dishoeck (1997) and Nummelin et al. (2000), respectively. The W3(H₂O) observations are the most similar to our ALMA observations of N 105 in terms of the probed physical scales (~ 0.16 pc versus ~ 0.12 pc in N 105).

Metallicity-scaled CH_3OH abundances with respect to H_2 observed toward N 113 A1/B3 and N 105–2 A are the most similar to those observed toward Galactic hot cores, as can be seen in Figure 27; they are at the lower end of the range of those observed toward a larger Galactic hot cores sample (e.g., Mookerjee et al. 2007). The CH_3OH abundance estimated for N 105–2 B is lower than for N 105–2 A and the two hot cores in N 113 and is more similar to that of ST16, indicating that it may be an intermediate case between the organic-rich and organic-poor types of the LMC hot cores proposed by Shimonishi et al. (2020). Gerner et al. (2014) reported a low median CH_3OH abundance of 2.6×10^{-8} (for a typical hot core temperature of 100 K), comparable (within a factor of 2) to the 2 B’s metallicity-scaled CH_3OH abundance of 1.3×10^{-8} , estimated based on the IRAM 30 m telescope observations tracing the 0.02–0.4 pc spatial scales of 11 Galactic hot molecular cores (G9.62+0.19, G10.47+0.03, G29.96–0.02,

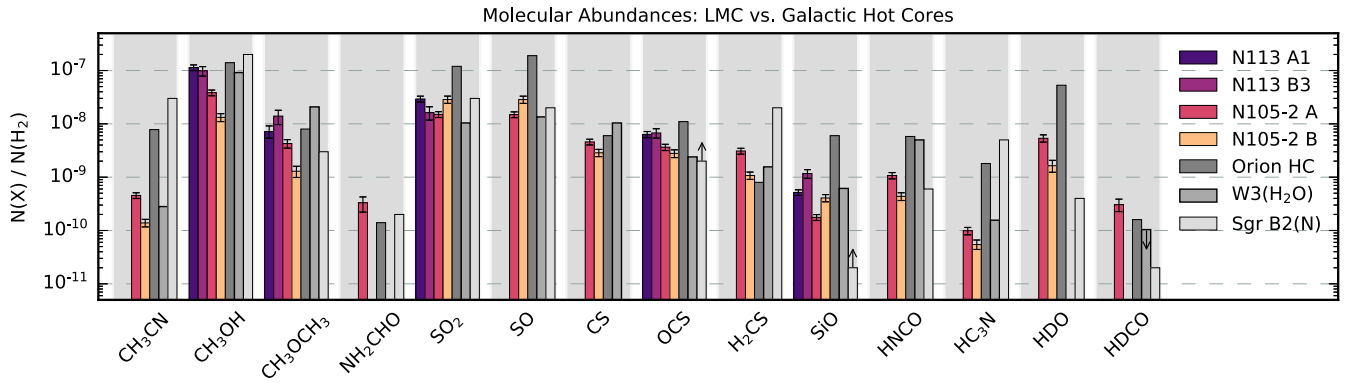


Figure 27. Comparison of the molecular abundances observed toward the organic-rich LMC (metallicity-scaled assuming $Z_{\text{LMC}} = 0.5 Z_{\odot}$) and selected Galactic hot cores. Upper and lower limits are indicated with arrows. The data for Galactic regions come from Blake et al. (1987) and Sutton et al. (1995) for Orion Hot Core (HC), from Nummelin et al. (2000) for Sgr B2(N), and from Helmich & van Dishoeck (1997) for W3(H₂O). The largest differences in molecular abundances between the LMC and Galactic hot cores are seen for N-bearing species.

G31.41+0.31, G34.26+0.15, G45.47+0.05, G75.78+0.34, NGC 7538B, Orion–KL, W31 IRS5, and W3(H₂O)); the authors acknowledge that their calculations provide CH₃OH abundances up to a factor of 10 lower than those reported in literature for the same objects.

For all hot cores in N105 and N113, the metallicity-corrected CH₃OCH₃ (N105 and N113) and HCOOCH₃ (N113) abundances are at the lower end of the range of those observed toward Galactic hot cores. The difference between the fractional abundances of the N-bearing species between the LMC (metallicity-scaled) and Galactic hot cores appears to be larger than that for COMs (e.g., CH₃CN and HC₃N; see Figure 27); however, they are still consistent with Galactic values. In Figure 27, similarly low abundances of CH₃CN, HNCO, and HC₃N as for 2 A and 2 B have been reported for the Galactic hot core W3(H₂O). The interesting result highlighted in Figure 27 is that the metallicity-corrected abundance of NH₂CHO observed toward 2 A is higher than those for the Orion and Sgr B2(N) hot cores. While intriguing, we stress that more reliable observations of NH₂CHO toward 2 A (higher sensitivity and more than one transition) are needed to draw reliable conclusions based on this result. No observations of N-bearing species exist for N113 A1/B3 hot cores (Sewilo et al. 2018).

Molecular abundances reported in the literature for a single region can vary significantly depending on the spatial scales probed and differences in the method for determining the column densities and abundances; e.g., for W3(H₂O) there is a difference of about two orders of magnitude between the measurements reported in Helmich & van Dishoeck (1997) and Bisschop et al. (2007). The measurements from Helmich & van Dishoeck (1997) that match the metallicity-scaled LMC data well (Figure 27) are based on the James Clerk Maxwell Telescope observations, which at the distance of W3 trace similar spatial scales as our ALMA observations in the LMC; also, the data analysis is similar. These examples highlight the importance of comparing the abundances observed toward the LMC hot cores with those of a carefully selected Galactic hot cores measured based on the observations sampling similar physical scales and using a similar data analysis methods. However, a comparison to a broader population of Galactic hot cores does not change our overall conclusion that hot cores 2 A and 2 B are not significantly different than Galactic hot cores.

Figure 27 shows that hot cores 2 A and 2 B indeed belong to the organic-rich category proposed by Shimonishi et al. (2020) (yet to be confirmed as a class based on a larger sample of hot cores) since the molecular abundances roughly scale with metallicity and larger COMs are detected.

Chemically distinct hot core types observed in the LMC may be explained if there are metallicity inhomogeneities in the LMC disk. The chemical composition and dynamics of part of the LMC might have been altered by a close encounter between the LMC and SMC ($Z_{\text{SMC}} = 0.1\text{--}0.2 Z_{\odot}$) about 0.2 Gyr ago as suggested by the hydrodynamical simulations (e.g., Fujimoto & Noguchi 1990; Bekki & Chiba 2007a; Yozin & Bekki 2014) and the observational evidence including a highly asymmetric distribution of the H I and CO gas in the LMC and the presence of two H I velocity components separated by $\sim 50 \text{ km s}^{-1}$ in velocity, spatially connected by bridge H I features, and showing complementary spatial distributions on a kpc scale (e.g., Luks & Rohlfs 1992). One of the H I velocity components corresponds to the gas extending over the entire LMC disk and is dubbed the “D component.” The lower velocity gas (“L component”) is more spatially confined and introduces asymmetry in the distribution of the H I gas in the LMC.

According to the model, during the tidal interaction between the LMC and SMC, the H I gas is stripped from both galaxies, and the remnant gas falls down on each galaxy. In the LMC, this infalling H I gas is observed as the H I L component and has a relative velocity of $\sim 50 \text{ km s}^{-1}$. A collision with the H I gas in the LMC disk triggered the formation of the young massive cluster R136 in 30 Dor and massive stars in the region extending south of 30 Dor–H I Ridge; it includes two major elongated CO clouds in the southeast of the LMC: the Molecular Ridge and the CO Arc (Fukui et al. 2017). A similar scenario of massive star formation triggered by the colliding H I flows as a result of the SMC–LMC interaction was recently proposed for star-forming regions N 44 and N 159 (Fukui et al. 2019; Tokuda et al. 2019; Tsuge et al. 2019).

Numerical simulations show that the gas infalling on the LMC disk contains a large amount of metal-poor gas from the SMC (Bekki & Chiba 2007b), replenishing the higher-metallicity material in the LMC with metal-poor gas and causing metallicity inhomogeneities. Fukui et al. (2017) and Tsuge et al. (2019) found that the H I L component is metal-poor in the H I Ridge and N44, confirming this model prediction. Tsuge et al. (2019) estimated the fraction of the

SMC gas in the HI Ridge (including R136) and N44 of 0.5 and 0.3, respectively. The metal content was estimated based on the correlation between the dust optical depth at 353 GHz (τ_{353} ; measured using the combined Planck and IRAS data) and the HI intensity (gas/dust $\sim W(\text{HI})/\tau_{353}$).

The differences in the physical and chemical conditions in each galaxy are likely significant enough for gas mixing to result in a range of environments that would lead to variations in the hot core COM abundances. Regions affected by tidal interactions between the LMC and SMC would be characterized by a lower dust-to-gas ratio, stronger UV radiation fields, and consequently higher dust temperatures than in the unaffected LMC gas (e.g., van Loon et al. 2010; Roman-Duval et al. 2014). The lower dust content means that there would be less dust grains for surface chemistry. Higher dust temperatures may result in less efficient formation of COMs as predicted by the warm ice chemistry model and astrochemical simulations (e.g., Shimonishi et al. 2016a; Acharyya & Herbst 2018). The number of heavy elements available for chemistry would also be lower because in the SMC the elemental abundances of gaseous (N, C, O) atoms are $\sim(3, 2, 2)$ lower than in the LMC (e.g., Russell & Dopita 1992). The cosmic-ray density in the SMC is only $\sim 15\%$ of that observed in the solar neighborhood (compared to $\sim 25\%$ in the LMC; Abdo et al. 2010b), making the cosmic-ray-induced UV radiation less effective than in the LMC.

Hot core ST11 with nondetection of COMs is located near the region thought to be affected by the interaction between the LMC and SMC, possibly in a lower-metallicity region, while all known hot cores with COMs are associated with the unaffected areas in the disk. This distribution of hot cores with and without COMs may be the result of a source selection effect; a larger sample of hot cores is needed to investigate the connection between the metallicity inhomogeneities and the properties of hot cores.

8. Summary and Conclusions

To increase the sample of hot cores in the LMC, we conducted ALMA observations toward seven fields in the LMC having common characteristics with two fields in the star-forming region N113 hosting the only hot cores with COMs known prior to our observations (association with YSOs, OH/H₂O masers, and/or the SO emission). Our ALMA observations covered four 1875 MHz spectral windows between ~ 241 GHz and ~ 261 GHz. Here, we present the analysis of the three ALMA fields located in star-forming region N105 at the western edge of the LMC bar.

We performed spectral analysis of 12 1.2 mm continuum sources in N105. We identified S-bearing species: SO, ³³SO, SO₂, ³⁴SO₂, CS, C³³S, OCS, H₂CS; N-bearing species: HNC, HC₃N, HC¹⁵N, H¹³CN; three deuterated molecules: HDO, HDCO, and HDS; as well as SiO, H¹³CO⁺, and CH₂CO. We detected COMs CH₃OH, CH₃CN, and CH₃OCH₃ and tentatively detected NH₂CHO (a 3.2σ detection of the strongest transition in the observed frequency range). If the presence of NH₂CHO in the LMC is confirmed, it will constitute the first detection of this astrobiologically relevant molecule in the extragalactic subsolar-metallicity environment, providing us insight into the metal-poor systems from the earlier cosmological epochs.

Methanol has been detected toward all the sources and shows both the extended and compact emission, while other

COMs are mainly associated with the 1.2 mm continuum sources N105–2A and 2B. Based on the spectral line modeling, we estimated rotational temperatures and column densities, as well as the fractional molecular abundances for all the continuum sources. The physical and chemical properties of 2A and 2B indicate that these sources are bona fide hot cores. We also identified sources 2C, 2F, 3B, and 1A as hot core candidates; they have high temperatures in at least one of the four species with multiple transitions.

We compared the fractional molecular abundances of hot cores 2A and 2B to those observed toward other known LMC hot cores and toward representative Galactic hot cores. We concluded that hot cores 2A and 2B are “organic-rich” as defined by Shimonishi et al. (2020) because they are associated with COMs more complex than six atoms, and the observed molecular abundances roughly scale with metallicity. Chemically distinct hot core types observed in the LMC may be explained if there are metallicity inhomogeneities in the LMC disk. Such metallicity inhomogeneities may be the result of the tidal interactions between the LMC and the SMC.

We report the detection of the CO₂ ice band at 15.2 μm in the Spitzer/IRS spectrum of the mid-IR source likely associated with both 2A and 2B, which was missed in previous studies, indicating that the source is at the early stage of the protostellar evolution, consistent with our ALMA observations. The near-IR VLT/KMOS spectroscopic observations provided us insight into the nature of three near-IR sources in N105, two found to be embedded and associated with continuum sources 1A and 2E. The third KMOS source located nearby 2B is unlikely to be associated with this ALMA source; however, the KMOS data show evidence of the presence of the extended shocked emission in the region, consistent with the ALMA data.

Our observations highlight the need for higher sensitivity observations that would allow for a more reliable detection of larger molecules (higher signal-to-noise ratio and multiple transitions).

Finally, our study further confirms that larger COMs can be formed in low-metallicity galaxies, thus a possibility of the emergence of life as it happened on Earth is open in these systems.

We thank the anonymous referee for insightful comments that helped us improve the manuscript. The material is based upon work supported by NASA under award number 80GSFC21M0002 (M.S.). A.S.M. carried out this research within the Collaborative Research Centre 956 (subproject A6), funded by the Deutsche Forschungsgemeinschaft (DFG)-project ID 184018867. A.K. acknowledges support from the First TEAM grant of the Foundation for Polish Science No. POIR.04.04.00-00-5D21/18-00. This article has been supported by the Polish National Agency for Academic Exchange under grant No. PPI/APM/2018/1/00036/U/001 (A.K.). M. S. acknowledges partial support from the NASA ADAP grant No. 80NSSC22K0168. This research is supported by NSF award 2009624 to Univ. Virginia (R.I.). S.B.C., M.A.C., and E. G.B. were supported by the NASA Planetary Science Division Internal Scientist Funding Program through the Fundamental Laboratory Research work package (FLaRe). We thank Dr. Jürgen Ott for making an unpublished list of water masers in the LMC available to us. The National Radio Astronomy Observatory is a facility of the National Science Foundation

operated under cooperative agreement by Associated Universities, Inc. This paper makes use of the following ALMA data: ADS/JAO.ALMA#2019.1.01720.S and #2017.1.00093.S. ALMA is a partnership of ESO (representing its member states), NSF (USA) and NINS (Japan), together with NRC (Canada), NSC and ASIAA (Taiwan), and KASI (Republic of Korea), in cooperation with the Republic of Chile. The Joint ALMA Observatory is operated by ESO, AUI/NRAO and NAOJ. The SAGE and HERITAGE data sets are made available by the Infrared Science Archive (IRSA) at IPAC, which is operated by the California Institute of Technology under contract with the National Aeronautics and Space Administration. This research made use of APLpy, an open-source plotting package for Python (Robitaille & Bressert 2012).

Facilities: ALMA, Spitzer, Herschel, VLT:Antu (KMOS)

Appendix A

The Results of Spectral Modeling and Fractional Abundances for Continuum Sources in N 105

Table 6 provides the results of the LTE spectral modeling described in Section 4.3 for all the ALMA 1.2 mm continuum sources in N 105–1, N 105–2, and N 105–3. It also includes fractional abundances with respect to both H₂ and CH₃OH. Table 7, Figure A1, and Figure A2 provide the results of the additional XCLASS LTE modeling of SO₂ for hot cores N 105–2 A and 2 B; the XCLASS analysis is described in Section 4.3.1.

Table 6
Results of Spectral Modeling and Fractional Abundances with Respect to H₂ and CH₃OH

Source	Species, X	$T_{\text{rot}}(X)$ (K)	$N(X)$ (cm ⁻²)	v_{LSR} (km s ⁻¹)	Δv_{FWHM} (km s ⁻¹)	$N(X)/N(\text{H}_2)$	$N(X)/N(\text{CH}_3\text{OH})$
N 105-1 A	CH ₃ OH	12.1 ^{+1.0} _{-0.6}	(2.2 ^{+0.2} _{-0.2}) × 10 ¹⁴	236.5 ^{+0.1} _{-0.1}	3.2 ^{+0.3} _{-0.3}	(9.4 ^{+1.1} _{-1.2}) × 10 ⁻¹⁰	...
	H ¹³ CO ⁺	—'—	(5.6 ^{+0.2} _{-0.2}) × 10 ¹²	237.2 ^{+0.1} _{-0.1}	4.5 ^{+0.2} _{-0.2}	(2.4 ^{+0.2} _{-0.2}) × 10 ⁻¹¹	(2.6 ^{+0.2} _{-0.2}) × 10 ⁻²
	H ¹³ CN	—'—	(1.3 ^{+0.2} _{-0.2}) × 10 ¹²	234.2 ^{+0.3} _{-0.3}	2.5 ^{+0.7} _{-0.6}	(5.6 ^{+1.1} _{-1.1}) × 10 ⁻¹²	(6.0 ^{+1.2} _{-1.1}) × 10 ⁻³
	CS	—'—	(1.90 ^{+0.03} _{-0.03}) × 10 ¹⁴	236.72 ^{+0.02} _{-0.02}	3.03 ^{+0.04} _{-0.04}	(8.1 ^{+0.8} _{-0.8}) × 10 ⁻¹⁰	(8.6 ^{+0.7} _{-0.7}) × 10 ⁻¹
	H ₂ CS	—'—	<3.9 × 10 ¹³	237.2 ^{+0.5} _{-0.5}	2.2 ^{+1.0} _{-0.7}	<1.7 × 10 ⁻¹⁰	<1.8 × 10 ⁻¹
	SO ₂	95.5 ^{+19.9} _{-20.3}	(1.6 ^{+0.3} _{-0.2}) × 10 ¹⁴	237.7 ^{+0.2} _{-0.2}	4.9 ^{+0.5} _{-0.4}	(6.9 ^{+1.5} _{-1.2}) × 10 ⁻¹⁰	(7.4 ^{+1.5} _{-1.3}) × 10 ⁻¹
	SO	—'—	(3.5 ^{+0.4} _{-0.3}) × 10 ¹⁴	237.46 ^{+0.04} _{-0.04}	4.5 ^{+0.1} _{-0.1}	(1.5 ^{+0.2} _{-0.2}) × 10 ⁻⁹	1.6 ^{+0.2} _{-0.2}
N 105-1 B	CH ₃ OH	16.1 ^{+0.3} _{-0.3}	(5.0 ^{+0.2} _{-0.2}) × 10 ¹⁴	242.00 ^{+0.03} _{-0.03}	2.6 ^{+0.1} _{-0.1}	(5.9 ^{+0.7} _{-0.7}) × 10 ⁻¹⁰	...
	H ¹³ CO ⁺	—'—	(3.7 ^{+0.2} _{-0.2}) × 10 ¹²	242.3 ^{+0.1} _{-0.1}	2.8 ^{+0.2} _{-0.1}	(4.3 ^{+0.5} _{-0.4}) × 10 ⁻¹²	(7.3 ^{+0.4} _{-0.4}) × 10 ⁻³
	H ¹³ CN	—'—	(2.0 ^{+0.3} _{-0.3}) × 10 ¹²	242.2 ^{+0.1} _{-0.1}	2.3 ^{+0.3} _{-0.3}	(2.3 ^{+0.4} _{-0.4}) × 10 ⁻¹²	(4.0 ^{+0.5} _{-0.5}) × 10 ⁻³
	HC ¹⁵ N	—'—	(8.2 ^{+1.7} _{-1.7}) × 10 ¹¹	242.2 ^a	1.9 ^{+0.6} _{-0.4}	(9.5 ^{+2.3} _{-2.2}) × 10 ⁻¹³	(1.6 ^{+0.3} _{-0.3}) × 10 ⁻³
	CS	—'—	(2.5 ^{+0.1} _{-0.1}) × 10 ¹⁴	242.18 ^{+0.01} _{-0.01}	2.43 ^{+0.04} _{-0.03}	(2.9 ^{+0.4} _{-0.4}) × 10 ⁻¹⁰	(4.9 ^{+0.3} _{-0.3}) × 10 ⁻¹
	C ³³ S	—'—	(8.3 ^{+1.6} _{-1.3}) × 10 ¹²	242.9 ^{+0.4} _{-0.4}	4.6 ^{+0.8} _{-0.9}	(9.6 ^{+2.1} _{-1.9}) × 10 ⁻¹²	(1.7 ^{+0.3} _{-0.3}) × 10 ⁻²
	HNCO	—'—	(5.8 ^{+1.9} _{-1.5}) × 10 ¹³	242.1 ^a	3.0 ^{+1.3} _{-0.9}	(6.7 ^{+2.3} _{-1.9}) × 10 ⁻¹¹	(1.2 ^{+0.4} _{-0.3}) × 10 ⁻¹
	H ₂ CS	—'—	(7.5 ^{+0.9} _{-0.9}) × 10 ¹³	242.4 ^{+0.1} _{-0.1}	2.3 ^{+0.3} _{-0.2}	(8.8 ^{+1.4} _{-1.4}) × 10 ⁻¹¹	(1.5 ^{+0.2} _{-0.2}) × 10 ⁻¹
	SiO	—'—	<2.4 × 10 ¹²	242.9 ^{+0.5} _{-0.5}	2.9 ^{+1.4} _{-1.0}	<2.8 × 10 ⁻¹²	<4.8 × 10 ⁻³
	SO ₂	24.9 ^{+3.7} _{-3.5}	(4.8 ^{+0.8} _{-0.7}) × 10 ¹³	242.9 ^{+0.2} _{-0.2}	2.1 ^{+0.4} _{-0.3}	(5.6 ^{+1.1} _{-1.1}) × 10 ⁻¹¹	(9.6 ^{+1.5} _{-1.5}) × 10 ⁻²
N 105-1 C	CH ₃ OH	17.3 ^{+2.8} _{-2.5}	(1.6 ^{+0.2} _{-0.2}) × 10 ¹⁴	239.3 ^{+0.1} _{-0.1}	2.1 ^{+0.3} _{-0.2}	(3.3 ^{+0.9} _{-0.9}) × 10 ⁻¹⁰	...
	H ¹³ CO ⁺	—'—	(1.2 ^{+0.2} _{-0.1}) × 10 ¹²	239.2 ^{+0.1} _{-0.1}	1.6 ^{+0.3} _{-0.2}	(2.4 ^{+0.7} _{-0.6}) × 10 ⁻¹²	(7.2 ^{+1.6} _{-1.3}) × 10 ⁻³
	H ¹³ CN	—'—	(1.8 ^{+0.4} _{-0.3}) × 10 ¹²	239.6 ^{+0.2} _{-0.2}	2.1 ^{+0.5} _{-0.4}	(3.6 ^{+1.2} _{-1.1}) × 10 ⁻¹²	(1.1 ^{+0.3} _{-0.2}) × 10 ⁻²
	HC ¹⁵ N	—'—	(1.9 ^{+0.6} _{-0.4}) × 10 ¹²	239.4 ^{+0.5} _{-0.5}	5.1 ^{+1.2} _{-1.3}	(3.9 ^{+1.5} _{-1.2}) × 10 ⁻¹²	(1.2 ^{+0.4} _{-0.3}) × 10 ⁻²
	CS	—'—	(6.9 ^{+2.1} _{-1.1}) × 10 ¹³	239.41 ^{+0.02} _{-0.03}	2.2 ^{+0.1} _{-0.1}	(1.4 ^{+0.5} _{-0.4}) × 10 ⁻¹⁰	(4.2 ^{+1.4} _{-0.9}) × 10 ⁻¹
	C ³³ S	—'—	<3.1 × 10 ¹²	239.6 ^{+0.3} _{-0.3}	1.4 ^{+0.9} _{-0.7}	<6.2 × 10 ⁻¹²	<1.9 × 10 ⁻²
	SO	—'—	(1.4 ^{+0.6} _{-0.4}) × 10 ¹⁴	239.3 ^{+0.1} _{-0.1}	2.1 ^{+0.2} _{-0.2}	(2.9 ^{+1.4} _{-1.0}) × 10 ⁻¹⁰	(8.8 ^{+3.7} _{-2.6}) × 10 ⁻¹
N 105-2 A	H ₂ CS	—'—	(3.6 ^{+1.5} _{-1.2}) × 10 ¹³	240.1 ^{+0.3} _{-0.3}	2.1 ^{+0.6} _{-0.6}	(7.2 ^{+0.9} _{-0.9}) × 10 ⁻¹¹	(2.2 ^{+0.9} _{-0.8}) × 10 ⁻¹
	CH ₃ CN	152.3 ^{+9.7} _{-10.5}	(4.2 ^{+0.1} _{-0.1}) × 10 ¹³	243.0 ^{+0.1} _{-0.1}	4.2 ^{+0.1} _{-0.1}	(2.3 ^{+0.3} _{-0.3}) × 10 ⁻¹⁰	(11.8 ^{+0.4} _{-0.4}) × 10 ⁻³
	H ¹³ CO ⁺	—'—	(2.14 ^{+0.03} _{-0.03}) × 10 ¹³	241.90 ^{+0.02} _{-0.02}	3.13 ^{+0.04} _{-0.04}	(1.2 ^{+0.1} _{-0.1}) × 10 ⁻¹⁰	(6.1 ^{+0.1} _{-0.1}) × 10 ⁻³
	H ¹² CN	—'—	(2.1 ^{+0.1} _{-0.1}) × 10 ¹³	242.4 ^{+0.1} _{-0.1}	5.5 ^{+0.2} _{-0.2}	(1.2 ^{+0.1} _{-0.1}) × 10 ⁻¹⁰	(6.1 ^{+0.2} _{-0.2}) × 10 ⁻³
	HC ¹⁵ N	—'—	(1.2 ^{+0.1} _{-0.1}) × 10 ¹³	242.4 ^{+0.1} _{-0.1}	4.6 ^{+0.2} _{-0.2}	(6.3 ^{+0.8} _{-0.8}) × 10 ⁻¹¹	(3.3 ^{+0.2} _{-0.2}) × 10 ⁻³
	HC ₃ N	—'—	(9.1 ^{+0.8} _{-0.8}) × 10 ¹²	242.5 ^{+0.2} _{-0.2}	4.3 ^{+0.5} _{-0.5}	(5.0 ^{+0.7} _{-0.7}) × 10 ⁻¹¹	(2.6 ^{+0.2} _{-0.3}) × 10 ⁻³
	CS	—'—	(4.21 ^{+0.01} _{-0.01}) × 10 ¹⁴	241.55 ^{+0.01} _{-0.01}	3.88 ^{+0.01} _{-0.01}	(2.3 ^{+0.3} _{-0.3}) × 10 ⁻⁹	(12.0 ^{+0.2} _{-0.2}) × 10 ⁻²
	C ³³ S	—'—	(1.5 ^{+0.1} _{-0.1}) × 10 ¹³	241.2 ^{+0.1} _{-0.1}	3.0 ^{+0.3} _{-0.3}	(8.0 ^{+1.2} _{-1.2}) × 10 ⁻¹¹	(4.2 ^{+0.4} _{-0.3}) × 10 ⁻³
	H ₂ CS	—'—	(2.8 ^{+0.1} _{-0.1}) × 10 ¹⁴	241.9 ^{+0.1} _{-0.1}	3.6 ^{+0.1} _{-0.1}	(1.6 ^{+0.2} _{-0.2}) × 10 ⁻⁹	(8.1 ^{+0.3} _{-0.3}) × 10 ⁻²
	OCS	—'—	(3.4 ^{+0.2} _{-0.2}) × 10 ¹⁴	242.9 ^{+0.1} _{-0.1}	4.0 ^{+0.3} _{-0.3}	(1.8 ^{+0.2} _{-0.2}) × 10 ⁻⁹	(9.5 ^{+0.5} _{-0.6}) × 10 ⁻²
	SiO	—'—	(1.6 ^{+0.1} _{-0.1}) × 10 ¹³	242.5 ^{+0.1} _{-0.1}	5.5 ^{+0.3} _{-0.2}	(8.8 ^{+1.1} _{-1.1}) × 10 ⁻¹¹	(4.6 ^{+0.2} _{-0.2}) × 10 ⁻³
	NH ₂ CHO	—'—	(3.0 ^{+0.8} _{-0.8}) × 10 ¹³	243.3 ^{+0.5} _{-0.6}	4.0 ^{+1.3} _{-1.0}	(1.7 ^{+0.5} _{-0.5}) × 10 ⁻¹⁰	(8.6 ^{+2.3} _{-2.3}) × 10 ⁻³
	HNCO	—'—	(9.9 ^{+0.6} _{-0.6}) × 10 ¹³	243.8 ^a	4.2 ^a	(5.4 ^{+0.7} _{-0.7}) × 10 ⁻¹⁰	(2.8 ^{+0.3} _{-0.2}) × 10 ⁻²
	HDCO	—'—	(2.8 ^{+0.7} _{-0.6}) × 10 ¹³	242.2 ^{+0.4} _{-0.4}	3.4 ^{+1.0} _{-0.8}	(1.5 ^{+0.4} _{-0.4}) × 10 ⁻¹⁰	(8.0 ^{+1.9} _{-1.8}) × 10 ⁻³
	CH ₃ OCH ₃	—'—	(3.9 ^{+0.5} _{-0.5}) × 10 ¹⁴	242.9 ^{+0.3} _{-0.2}	3.4 ^{+0.8} _{-0.5}	(2.1 ^{+0.4} _{-0.4}) × 10 ⁻⁹	(1.1 ^{+0.2} _{-0.1}) × 10 ⁻¹
	CH ₂ CO	—'—	(4.8 ^{+0.9} _{-0.9}) × 10 ¹³	242.7 ^{+0.3} _{-0.3}	3.4 ^{+0.7} _{-0.6}	(2.6 ^{+0.6} _{-0.6}) × 10 ⁻¹⁰	(1.4 ^{+0.2} _{-0.3}) × 10 ⁻²
	HDO	—'—	(4.9 ^{+0.5} _{-0.4}) × 10 ¹⁴	242.7 ^{+0.2} _{-0.2}	4.2 ^{+0.4} _{-0.4}	(2.7 ^{+0.4} _{-0.4}) × 10 ⁻⁹	(1.4 ^{+0.2} _{-0.1}) × 10 ⁻¹
CH ₃ OH (hot)	170.9 ^{+4.6} _{-4.2}	(3.5 ^{+0.1} _{-0.1}) × 10 ¹⁵	242.83 ^{+0.04} _{-0.05}	4.3 ^{+0.1} _{-0.1}	(1.9 ^{+0.2} _{-0.2}) × 10 ⁻⁸	...	
CH ₃ OH (cold)	14.2 ^{+1.3} _{-1.0}	(3.9 ^{+0.2} _{-0.2}) × 10 ¹⁴	241.3 ^{+0.1} _{-0.1}	3.1 ^{+0.2} _{-0.1}	(2.1 ^{+0.3} _{-0.3}) × 10 ⁻⁹	(11.2 ^{+0.6} _{-0.6}) × 10 ⁻²	
SO ₂ (hot)	176.0 ^{+5.6} _{-4.9}	(1.38 ^{+0.04} _{-0.04}) × 10 ¹⁵	242.82 ^{+0.05} _{-0.04}	4.7 ^{+0.1} _{-0.1}	(7.5 ^{+0.9} _{-1.0}) × 10 ⁻⁹	(3.9 ^{+0.1} _{-0.1}) × 10 ⁻¹	
SO	—'—	(1.37 ^{+0.03} _{-0.02}) × 10 ¹⁵	242.07 ^{+0.01} _{-0.01}	4.24 ^{+0.03} _{-0.03}	(7.5 ^{+0.9} _{-0.9}) × 10 ⁻⁹	(3.9 ^{+0.1} _{-0.1}) × 10 ⁻¹	
³³ SO	—'—	(8.2 ^{+0.8} _{-0.7}) × 10 ¹³	243.3 ^{+0.2} _{-0.2}	3.2 ^{+0.6} _{-0.4}	(4.5 ^{+0.7} _{-0.7}) × 10 ⁻¹⁰	(2.3 ^{+0.2} _{-0.2}) × 10 ⁻²	
SO ₂ (cold)	24.2 ^{+1.5} _{-1.7}	(3.1 ^{+0.2} _{-0.2}) × 10 ¹⁴	242.4 ^{+0.1} _{-0.1}	3.8 ^{+0.1} _{-0.1}	(1.7 ^{+0.2} _{-0.2}) × 10 ⁻⁹	(8.8 ^{+0.5} _{-0.5}) × 10 ⁻²	
³⁴ SO ₂	114.8 ^{+36.0} _{-21.5}	(1.1 ^{+0.2} _{-0.2}) × 10 ¹⁴	243.1 ^{+0.1} _{-0.1}	2.6 ^{+0.3} _{-0.3}	(6.1 ^{+1.4} _{-1.2}) × 10 ⁻¹⁰	(3.2 ^{+0.6} _{-0.5}) × 10 ⁻²	
N 105-2 B	CH ₃ CN	88.2 ^{+10.1} _{-9.4}	(2.2 ^{+0.1} _{-0.1}) × 10 ¹³	243.2 ^{+0.2} _{-0.2}	6.7 ^{+0.5} _{-0.4}	(6.9 ^{+1.2} _{-1.1}) × 10 ⁻¹¹	(10.5 ^{+0.9} _{-0.8}) × 10 ⁻³
	H ¹³ CO ⁺	—'—	(1.96 ^{+0.02} _{-0.02}) × 10 ¹³	243.32 ^{+0.02} _{-0.02}	3.49 ^{+0.04} _{-0.04}	(6.3 ^{+1.0} _{-0.7}) × 10 ⁻¹¹	(9.5 ^{+0.7} _{-0.7}) × 10 ⁻³
	H ¹³ CN	—'—	(1.59 ^{+0.04} _{-0.04}) × 10 ¹³	243.3 ^{+0.1} _{-0.1}	7.1 ^{+0.3} _{-0.2}	(5.1 ^{+0.8} _{-0.8}) × 10 ⁻¹¹	(7.7 ^{+0.6} _{-0.6}) × 10 ⁻³
	HC ¹⁵ N	—'—	(8.9 ^{+0.4} _{-0.4}) × 10 ¹²	243.3 ^{+0.1} _{-0.1}	5.9 ^{+0.3} _{-0.2}	(2.9 ^{+0.5} _{-0.4}) × 10 ⁻¹¹	(4.3 ^{+0.3} _{-0.3}) × 10 ⁻³
	HC ₃ N	—'—	(8.5 ^{+1.3} _{-1.0}) × 10 ¹²	242.9 ^{+0.4} _{-0.3}	4.8 ^{+0.8} _{-0.6}	(2.7 ^{+0.6} _{-0.5}) × 10 ⁻¹¹	(4.1 ^{+0.7} _{-0.5}) × 10 ⁻³
	CS	—'—	(4.48 ^{+0.01} _{-0.01}) × 10 ¹⁴	242.8 ^a	4.09 ^{+0.01} _{-0.01}	(1.4 ^{+0.2} _{-0.2}) × 10 ⁻⁹	(2.2 ^{+0.2} _{-0.1}) × 10 ⁻¹
	C ³³ S	—'—	(1.2 ^{+0.1} _{-0.1}) × 10 ¹³	242.8 ^{+0.1} _{-0.1}	3.3 ^{+0.3} _{-0.3}	(3.7 ^{+0.7} _{-0.6}) × 10 ⁻¹¹	(5.7 ^{+0.7} _{-0.6}) × 10 ⁻³
H ₂ CS	—'—	(1.7 ^{+0.1} _{-0.1}) × 10 ¹⁴	242.8 ^{+0.1} _{-0.1}	3.6 ^{+0.1} _{-0.1}	(5.4 ^{+0.9} _{-0.8}) × 10 ⁻¹⁰	(8.1 ^{+0.6} _{-0.6}) × 10 ⁻²	

Table 6
(Continued)

Source	Species, X	$T_{\text{rot}}(X)$ (K)	$N(X)$ (cm^{-2})	v_{LSR} (km s^{-1})	Δv_{FWHM} (km s^{-1})	$N(X)/N(\text{H}_2)$	$N(X)/N(\text{CH}_3\text{OH})$
N 105-2 C	OCS	—'—	$(4.4_{-0.3}^{+0.2}) \times 10^{14}$	$243.0_{-0.2}^{+0.1}$	$5.8_{-0.4}^{+0.4}$	$(1.4_{-0.2}^{+0.2}) \times 10^{-9}$	$(2.1_{-0.2}^{+0.2}) \times 10^{-1}$
	SiO	—'—	$(6.4_{-0.1}^{+0.1}) \times 10^{13}$	$244.9_{-0.1}^{+0.1}$	$11.1_{-0.1}^{+0.1}$	$(2.0_{-0.3}^{+0.3}) \times 10^{-10}$	$(3.1_{-0.2}^{+0.2}) \times 10^{-2}$
	HNCO	—'—	$(6.8_{-0.5}^{+0.4}) \times 10^{13}$	242.9^a	4.9^a	$(2.2_{-0.4}^{+0.4}) \times 10^{-10}$	$(3.3_{-0.3}^{+0.3}) \times 10^{-2}$
	HDO	—'—	$(2.6_{-0.5}^{+0.5}) \times 10^{14}$	$245.8_{-0.7}^{+0.8}$	$8.2_{-1.8}^{+2.3}$	$(8.2_{-2.0}^{+2.1}) \times 10^{-10}$	$(1.2_{-0.3}^{+0.3}) \times 10^{-1}$
	CH ₃ OCH ₃	—'—	$(2.0_{-0.4}^{+0.4}) \times 10^{14}$	$243.1_{-0.5}^{+0.6}$	$4.9_{-1.1}^{+1.3}$	$(6.5_{-1.5}^{+1.6}) \times 10^{-10}$	$(9.8_{-1.9}^{+1.9}) \times 10^{-2}$
	CH ₃ OH (hot)	$136.1_{-7.6}^{+8.2}$	$(2.1_{-0.1}^{+0.8}) \times 10^{15}$	$243.1_{-0.1}^{+0.1}$	$6.2_{-0.2}^{+0.3}$	$(6.6_{-1.1}^{+1.1}) \times 10^{-9}$...
	CH ₃ OH (cold)	$15.6_{-1.0}^{+1.1}$	$(7.1_{-0.3}^{+0.3}) \times 10^{14}$	$242.9_{-0.1}^{+0.1}$	$3.7_{-0.1}^{+0.1}$	$(2.3_{-0.4}^{+0.4}) \times 10^{-9}$	$(3.4_{-0.3}^{+0.3}) \times 10^{-1}$
	SO ₂ (hot)	$161.5_{-2.4}^{+2.4}$	$(4.5_{-0.1}^{+0.1}) \times 10^{15}$	$245.2_{-0.1}^{+0.1}$	$11.6_{-0.1}^{+0.1}$	$(1.4_{-0.2}^{+0.2}) \times 10^{-8}$	$2.2_{-0.2}^{+0.2}$
	SO	—'—	$(4.46_{-0.05}^{+0.04}) \times 10^{15}$	$243.84_{-0.01}^{+0.01}$	$7.96_{-0.02}^{+0.02}$	$(1.4_{-0.2}^{+0.2}) \times 10^{-8}$	$2.2_{-0.1}^{+0.2}$
	³³ SO	—'—	$(2.7_{-0.1}^{+0.1}) \times 10^{14}$	$244.4_{-0.2}^{+0.2}$	$8.5_{-0.4}^{+0.4}$	$(8.5_{-1.4}^{+1.4}) \times 10^{-10}$	$(1.3_{-0.1}^{+0.1}) \times 10^{-1}$
	SO ₂ (cold)	$28.2_{-0.8}^{+0.9}$	$(1.08_{-0.03}^{+0.04}) \times 10^{15}$	$243.9_{-0.1}^{+0.1}$	$7.7_{-0.1}^{+0.1}$	$(3.5_{-0.5}^{+0.6}) \times 10^{-9}$	$(5.2_{-0.4}^{+0.4}) \times 10^{-1}$
	³⁴ SO ₂	$113.6_{-12.2}^{+12.2}$	$(3.7_{-0.3}^{+0.4}) \times 10^{14}$	$245.2_{-0.2}^{+0.2}$	$9.3_{-0.5}^{+0.5}$	$(1.2_{-0.2}^{+0.2}) \times 10^{-9}$	$(1.8_{-0.2}^{+0.2}) \times 10^{-1}$
	CH ₃ OH (hot)	$95.3_{-20.4}^{+28.3}$	$(6.7_{-2.1}^{+2.4}) \times 10^{13}$	$242.5_{-0.1}^{+0.1}$	$1.0_{-0.2}^{+0.2}$	$(8.3_{-3.1}^{+4.1}) \times 10^{-10}$...
	CH ₃ CN	—'—	$(4.3_{-0.7}^{+1.0}) \times 10^{12}$	242.8^a	$3.9_{-0.7}^{+1.0}$	$(5.3_{-1.6}^{+2.3}) \times 10^{-11}$	$(6.4_{-2.2}^{+2.7}) \times 10^{-2}$
	H ¹³ CO ⁺	—'—	$(3.3_{-0.5}^{+0.7}) \times 10^{12}$	$242.3_{-0.1}^{+0.1}$	$3.1_{-0.2}^{+0.2}$	$(4.2_{-1.2}^{+1.7}) \times 10^{-11}$	$(5.0_{-1.7}^{+2.1}) \times 10^{-2}$
	H ¹³ CN	—'—	$(3.8_{-0.7}^{+0.9}) \times 10^{12}$	$243.1_{-0.2}^{+0.3}$	$4.6_{-0.5}^{+0.5}$	$(4.8_{-1.5}^{+1.9}) \times 10^{-11}$	$(5.7_{-2.1}^{+2.4}) \times 10^{-2}$
	HC ¹⁵ N	—'—	$(3.0_{-0.6}^{+0.7}) \times 10^{12}$	$241.8_{-0.3}^{+0.3}$	$5.5_{-0.7}^{+0.8}$	$(3.8_{-1.2}^{+1.5}) \times 10^{-11}$	$(4.5_{-1.7}^{+1.9}) \times 10^{-2}$
	CS	—'—	$(3.3_{-0.4}^{+0.6}) \times 10^{14}$	$242.47_{-0.01}^{+0.01}$	$4.52_{-0.04}^{+0.03}$	$(4.1_{-1.1}^{+1.5}) \times 10^{-9}$	$4.9_{-1.6}^{+1.9}$
	C ³³ S	—'—	$(1.3_{-0.2}^{+0.3}) \times 10^{13}$	$242.3_{-0.1}^{+0.1}$	$2.6_{-0.2}^{+0.2}$	$(1.7_{-0.5}^{+0.7}) \times 10^{-10}$	$(2.0_{-0.7}^{+0.8}) \times 10^{-1}$
	H ₂ CS	—'—	$(1.4_{-0.2}^{+0.4}) \times 10^{14}$	$242.33_{-0.05}^{+0.03}$	$2.8_{-0.1}^{+0.1}$	$(1.7_{-0.5}^{+0.7}) \times 10^{-9}$	$2.0_{-0.7}^{+0.9}$
	OCS	—'—	$(9.2_{-1.9}^{+2.1}) \times 10^{13}$	$243.2_{-0.3}^{+0.3}$	$3.0_{-0.6}^{+0.8}$	$(1.1_{-0.4}^{+0.5}) \times 10^{-9}$	$1.4_{-0.5}^{+0.6}$
	SiO	—'—	$(8.5_{-1.0}^{+1.4}) \times 10^{12}$	$242.1_{-0.2}^{+0.2}$	$6.4_{-0.3}^{+0.4}$	$(1.1_{-0.3}^{+0.4}) \times 10^{-10}$	$(1.3_{-0.4}^{+0.5}) \times 10^{-1}$
	HNCO	—'—	$(1.5_{-0.4}^{+0.4}) \times 10^{13}$	243.7^a	2.6^a	$(1.8_{-0.7}^{+0.8}) \times 10^{-10}$	$(2.2_{-0.9}^{+0.9}) \times 10^{-1}$
	CH ₃ OH (cold)	$10.4_{-0.1}^{+0.1}$	$(4.2_{-0.1}^{+0.1}) \times 10^{15}$	$242.39_{-0.02}^{+0.02}$	$3.53_{-0.03}^{+0.03}$	$(5.3_{-1.8}^{+1.8}) \times 10^{-8}$	$63.3_{-19.6}^{+22.6}$
	HDS	—'—	$(4.4_{-0.6}^{+0.5}) \times 10^{13}$	$242.0_{-0.1}^{+0.1}$	$2.4_{-0.3}^{+0.4}$	$(5.5_{-1.6}^{+1.9}) \times 10^{-10}$	$(6.6_{-2.2}^{+2.5}) \times 10^{-1}$
	SO ₂	$32.0_{-3.2}^{+3.7}$	$(8.8_{-0.8}^{+0.8}) \times 10^{13}$	$241.7_{-0.3}^{+0.3}$	$6.0_{-0.6}^{+0.7}$	$(1.1_{-0.3}^{+0.4}) \times 10^{-9}$	$1.3_{-0.4}^{+0.5}$
	SO	—'—	$(3.4_{-0.2}^{+0.3}) \times 10^{14}$	$242.24_{-0.02}^{+0.03}$	$3.7_{-0.1}^{+0.1}$	$(4.2_{-1.1}^{+1.4}) \times 10^{-9}$	$5.0_{-1.6}^{+1.8}$
	CH ₃ OH (cold)	$10.0_{-0.1}^{+0.1}$	$(3.0_{-0.1}^{+0.1}) \times 10^{15}$	$243.38_{-0.01}^{+0.02}$	$2.31_{-0.03}^{+0.03}$	$(1.5_{-0.2}^{+0.2}) \times 10^{-8}$	$71.1_{-23.5}^{+63.7}$
CH ₃ OH (warm)	$31.3_{-1.1}^{+1.4}$	$(4.1_{-1.3}^{+3.5}) \times 10^{13}$	$240.6_{-0.6}^{+2.4}$	$3.2_{-1.4}^{+6.1}$	$(2.0_{-0.7}^{+1.7}) \times 10^{-10}$...	
H ¹³ CO ⁺	—'—	$(1.3_{-0.1}^{+0.1}) \times 10^{12}$	$243.7_{-0.2}^{+0.1}$	$3.5_{-0.3}^{+0.3}$	$(6.1_{-0.9}^{+0.9}) \times 10^{-12}$	$(3.1_{-1.0}^{+2.7}) \times 10^{-2}$	
H ¹³ CN	—'—	$(1.2_{-0.2}^{+0.2}) \times 10^{12}$	$242.9_{-0.2}^{+0.3}$	$3.3_{-0.6}^{+0.6}$	$(5.7_{-1.1}^{+1.1}) \times 10^{-12}$	$2.9_{-1.0}^{+2.5}$	
HC ¹⁵ N	—'—	$(5.7_{-1.0}^{+1.3}) \times 10^{11}$	$243.3_{-0.2}^{+0.2}$	$2.0_{-0.4}^{+0.6}$	$(2.8_{-0.6}^{+0.7}) \times 10^{-12}$	$1.4_{-0.5}^{+1.3} \times 10^{-2}$	
CS	—'—	$(2.4_{-0.1}^{+0.1}) \times 10^{14}$	243.2^a	$2.96_{-0.03}^{+0.03}$	$(1.2_{-0.1}^{+0.2}) \times 10^{-9}$	$6.0_{-1.9}^{+5.1}$	
C ³³ S	—'—	$(5.2_{-0.6}^{+0.5}) \times 10^{12}$	$243.3_{-0.1}^{+0.2}$	$2.6_{-0.3}^{+0.3}$	$(2.5_{-0.4}^{+0.4}) \times 10^{-11}$	$(1.3_{-0.4}^{+1.1}) \times 10^{-1}$	
H ₂ CS	—'—	$(6.5_{-0.3}^{+0.3}) \times 10^{13}$	$243.3_{-0.1}^{+0.1}$	$2.5_{-0.1}^{+0.1}$	$(3.2_{-0.4}^{+0.4}) \times 10^{-10}$	$1.6_{-0.5}^{+1.4}$	
SO	—'—	$(2.2_{-0.1}^{+0.1}) \times 10^{14}$	$243.40_{-0.02}^{+0.02}$	$2.8_{-0.1}^{+0.1}$	$(1.1_{-0.1}^{+0.1}) \times 10^{-9}$	$5.5_{-1.7}^{+4.7}$	
SiO	—'—	$(2.5_{-0.4}^{+0.4}) \times 10^{12}$	$244.1_{-0.5}^{+0.5}$	$7.0_{-1.1}^{+1.5}$	$(1.2_{-0.2}^{+0.3}) \times 10^{-11}$	$(6.2_{-2.2}^{+5.4}) \times 10^{-2}$	
CH ₃ OH	$13.5_{-1.1}^{+1.5}$	$(1.9_{-0.3}^{+0.3}) \times 10^{14}$	$241.4_{-0.1}^{+0.1}$	$2.1_{-0.3}^{+0.3}$	$(3.1_{-0.7}^{+0.8}) \times 10^{-10}$...	
H ¹³ CO ⁺	—'—	$(1.5_{-0.2}^{+0.3}) \times 10^{12}$	$241.2_{-0.2}^{+0.1}$	$1.5_{-0.2}^{+0.3}$	$(2.4_{-0.6}^{+0.7}) \times 10^{-12}$	$(7.8_{-1.7}^{+2.0}) \times 10^{-3}$	
CS	—'—	$(1.3_{-0.4}^{+0.4}) \times 10^{14}$	$241.27_{-0.02}^{+0.02}$	$1.9_{-0.1}^{+0.1}$	$(2.1_{-0.6}^{+0.7}) \times 10^{-10}$	$(6.6_{-1.7}^{+2.7}) \times 10^{-1}$	
SO	—'—	$(3.7_{-1.0}^{+1.1}) \times 10^{14}$	$241.2_{-0.1}^{+0.1}$	$1.8_{-0.2}^{+0.2}$	$(5.9_{-1.9}^{+2.1}) \times 10^{-10}$	$1.9_{-0.6}^{+0.7}$	
CH ₃ OH (hot)	$126.0_{-30.1}^{+33.3}$	$(2.2_{-0.8}^{+1.0}) \times 10^{14}$	$242.8_{-0.6}^{+0.6}$	$2.8_{-1.0}^{+1.0}$	$(1.8_{-0.8}^{+0.9}) \times 10^{-9}$...	
SO ₂ (hot)	—'—	$(1.5_{-0.4}^{+0.3}) \times 10^{14}$	$243.5_{-0.6}^{+0.7}$	$6.4_{-1.6}^{+1.7}$	$(1.3_{-0.5}^{+0.5}) \times 10^{-9}$	$(7.1_{-3.1}^{+3.5}) \times 10^{-1}$	
H ¹³ CO ⁺	—'—	$(6.3_{-1.0}^{+1.5}) \times 10^{12}$	$242.0_{-0.1}^{+0.1}$	$2.8_{-0.2}^{+0.3}$	$(5.4_{-1.7}^{+2.0}) \times 10^{-11}$	$(2.9_{-1.2}^{+1.5}) \times 10^{-2}$	
H ¹³ CN	—'—	$(4.5_{-1.1}^{+1.5}) \times 10^{12}$	$242.0_{-0.2}^{+0.2}$	$2.3_{-0.4}^{+0.5}$	$(3.8_{-1.4}^{+1.7}) \times 10^{-11}$	$(2.1_{-0.9}^{+1.1}) \times 10^{-2}$	
HC ¹⁵ N	—'—	$<1.4 \times 10^{12}$	$241.5_{-0.6}^{+0.7}$	$2.4_{-1.0}^{+1.9}$	$<1.2 \times 10^{-11}$	$(6.6_{-4.0}^{+4.9}) \times 10^{-3}$	
CS	—'—	$(4.9_{-0.7}^{+0.9}) \times 10^{14}$	$241.9_{-0.1}^{+0.1}$	$3.6_{-0.1}^{+0.1}$	$(4.2_{-1.3}^{+1.4}) \times 10^{-9}$	$2.3_{-0.9}^{+1.1}$	
C ³³ S	—'—	$(1.7_{-0.3}^{+0.4}) \times 10^{13}$	$241.9_{-0.3}^{+0.3}$	$4.2_{-0.7}^{+0.7}$	$(1.5_{-0.5}^{+0.5}) \times 10^{-10}$	$(7.9_{-3.4}^{+3.9}) \times 10^{-2}$	
H ₂ CS	—'—	$(2.3_{-0.5}^{+0.7}) \times 10^{14}$	$242.0_{-0.1}^{+0.1}$	$3.1_{-0.2}^{+0.2}$	$(2.0_{-0.7}^{+0.9}) \times 10^{-9}$	$1.1_{-0.5}^{+0.6}$	
SO	—'—	$(4.7_{-0.6}^{+0.8}) \times 10^{14}$	$241.9_{-0.1}^{+0.1}$	$3.3_{-0.1}^{+0.1}$	$(4.0_{-1.2}^{+1.4}) \times 10^{-9}$	$2.2_{-0.9}^{+1.0}$	
SiO	—'—	$(8.8_{-1.5}^{+2.2}) \times 10^{12}$	$242.5_{-0.6}^{+0.5}$	$7.6_{-1.2}^{+1.1}$	$(7.5_{-2.4}^{+2.9}) \times 10^{-11}$	$(4.1_{-1.7}^{+2.1}) \times 10^{-2}$	
CH ₃ OH (cold)	$6.9_{-0.2}^{+0.2}$	$(6.7_{-1.3}^{+1.1}) \times 10^{15}$	$241.8_{-0.1}^{+0.1}$	$2.4_{-0.1}^{+0.1}$	$(5.7_{-1.9}^{+1.9}) \times 10^{-8}$	$30.9_{-13.0}^{+14.7}$	
SO ₂ (cold)	—'—	$(3.9_{-0.9}^{+0.8}) \times 10^{14}$	$241.9_{-0.4}^{+0.4}$	$3.6_{-0.8}^{+1.1}$	$(3.3_{-1.2}^{+1.2}) \times 10^{-9}$	$1.8_{-0.8}^{+0.9}$	
³⁴ SO ₂	—'—	$(2.0_{-0.3}^{+0.5}) \times 10^{15}$	$244.0_{-0.3}^{+0.2}$	$1.7_{-0.7}^{+0.7}$	$(1.7_{-0.6}^{+0.7}) \times 10^{-8}$	$9.4_{-4.9}^{+4.9}$	
CH ₃ OH	$10.6_{-1.0}^{+1.3}$	$(1.2_{-0.3}^{+0.3}) \times 10^{14}$	$238.4_{-0.1}^{+0.1}$	$2.0_{-0.3}^{+0.3}$	$(2.9_{-0.9}^{+1.0}) \times 10^{-10}$...	
H ¹³ CO ⁺	—'—	$(1.7_{-0.3}^{+0.4}) \times 10^{12}$	$238.3_{-0.1}^{+0.1}$	$1.9_{-0.2}^{+0.2}$	$(4.1_{-1.1}^{+1.3}) \times 10^{-12}$	$(1.4_{-0.4}^{+0.4}) \times 10^{-2}$	
HC ¹⁵ N	—'—	$(4.0_{-1.4}^{+1.7}) \times 10^{11}$	238.5^a	1.3^a	$(9.5_{-3.9}^{+4.7}) \times 10^{-13}$	$(3.3_{-1.4}^{+1.6}) \times 10^{-3}$	

Table 6
(Continued)

Source	Species, X	$T_{\text{rot}}(X)$ (K)	$N(X)$ (cm^{-2})	v_{LSR} (km s^{-1})	Δv_{FWHM} (km s^{-1})	$N(X)/N(\text{H}_2)$	$N(X)/N(\text{CH}_3\text{OH})$	
N 105-3 B	CS	—'—	$(9.7^{+3.7}_{-2.6}) \times 10^{13}$	$238.43^{+0.02}_{-0.02}$	$2.0^{+0.1}_{-0.1}$	$(2.3^{+1.0}_{-0.8}) \times 10^{-10}$	$(8.0^{+3.6}_{-2.8}) \times 10^{-1}$	
	SO ₂	$30.5^{+7.1}_{-7.0}$	$(2.0^{+0.5}_{-0.4}) \times 10^{13}$	$238.8^{+0.2}_{-0.2}$	$1.8^{+0.6}_{-0.5}$	$(4.9^{+1.6}_{-1.3}) \times 10^{-11}$	$(1.7^{+0.6}_{-0.5}) \times 10^{-1}$	
	SO	—'—	$(5.0^{+1.3}_{-0.7}) \times 10^{13}$	$238.5^{+0.1}_{-0.1}$	$2.3^{+0.2}_{-0.1}$	$(1.2^{+0.4}_{-0.3}) \times 10^{-10}$	$(4.1^{+1.5}_{-1.1}) \times 10^{-1}$	
	CH ₃ OH	$159.1^{+41.3}_{-60.6}$	$(1.8^{+0.9}_{-0.8}) \times 10^{14}$	$238.1^{+0.3}_{-0.2}$	$2.3^{+0.6}_{-0.5}$	$(1.9^{+1.1}_{-1.2}) \times 10^{-8}$...	
	H ¹³ CO ⁺	—'—	$(1.0^{+0.3}_{-0.4}) \times 10^{12}$	$237.4^{+0.2}_{-0.2}$	$1.8^{+0.5}_{-0.3}$	$(1.1^{+0.5}_{-0.6}) \times 10^{-10}$	$(5.9^{+3.5}_{-3.3}) \times 10^{-3}$	
N 105-3 C	CS	—'—	$(3.1^{+0.7}_{-0.5}) \times 10^{13}$	$237.46^{+0.02}_{-0.02}$	$1.61^{+0.05}_{-0.04}$	$(3.3^{+1.2}_{-1.7}) \times 10^{-9}$	$(1.8^{+0.9}_{-0.9}) \times 10^{-1}$	
	SO	—'—	$(1.9^{+0.7}_{-0.5}) \times 10^{13}$	237.8 ^a	$1.8^{+0.5}_{-0.4}$	$(2.0^{+0.9}_{-1.0}) \times 10^{-9}$	$(1.1^{+0.6}_{-0.6}) \times 10^{-1}$	
	CH ₃ OH	$10.8^{+3.1}_{-2.1}$	$(1.7^{+0.2}_{-0.2}) \times 10^{14}$	$238.9^{+0.2}_{-0.1}$	$1.8^{+0.3}_{-0.3}$	$(7.9^{+4.0}_{-3.0}) \times 10^{-10}$...	
	H ¹³ CO ⁺	—'—	$<1.6 \times 10^{12}$	$239.2^{+0.5}_{-0.4}$	$3.7^{+1.5}_{-0.9}$	$<7.2 \times 10^{-12}$	$(9.1^{+1.9}_{-2.2}) \times 10^{-3}$	
	CS	—'—	$(3.1^{+0.2}_{-0.2}) \times 10^{13}$	$239.0^{+0.1}_{-0.1}$	$1.6^{+0.2}_{-0.2}$	$(1.4^{+0.7}_{-0.5}) \times 10^{-10}$	$(1.8^{+0.2}_{-0.3}) \times 10^{-1}$	
N 113 A1	SO	—'—	$(5.0^{+0.5}_{-0.6}) \times 10^{14}$	$238.5^{+0.2}_{-0.2}$	$3.6^{+0.6}_{-0.5}$	$(2.3^{+1.1}_{-0.9}) \times 10^{-9}$	$2.8^{+0.4}_{-0.5}$	
	CH ₃ OH	$133.2^{+6.6}_{-6.8}$	$(1.5^{+0.1}_{-0.1}) \times 10^{16}$	$239.4^{+0.1}_{-0.1}$	$4.9^{+0.3}_{-0.2}$	$(5.7^{+0.7}_{-0.7}) \times 10^{-8}$...	
	HCOOCH ₃	—'—	$(8.5^{+0.8}_{-1.0}) \times 10^{14}$	239.4 ^a	4.9 ^a	$(3.2^{+0.5}_{-0.5}) \times 10^{-9}$	$(5.6^{+0.6}_{-0.9}) \times 10^{-2}$	
	CH ₃ OCH ₃	—'—	$(9.7^{+2.4}_{-2.1}) \times 10^{14}$	239.4 ^a	4.9 ^a	$(3.6^{+1.0}_{-0.9}) \times 10^{-9}$	$(6.3^{+1.6}_{-1.4}) \times 10^{-2}$	
	³³ SO	—'—	$(1.4^{+0.2}_{-0.2}) \times 10^{14}$	239.4 ^a	4.9 ^a	$(5.2^{+0.9}_{-1.0}) \times 10^{-10}$	$(9.2^{+1.3}_{-1.5}) \times 10^{-3}$	
	SO ₂	—'—	$(3.9^{+0.3}_{-0.2}) \times 10^{15}$	$238.9^{+0.2}_{-0.2}$	$8.1^{+0.6}_{-0.4}$	$(1.5^{+0.2}_{-0.2}) \times 10^{-8}$	$(2.6^{+0.2}_{-0.2}) \times 10^{-1}$	
	H ₂ S	—'—	$(1.2^{+0.1}_{-0.1}) \times 10^{15}$	$238.7^{+0.2}_{-0.2}$	$5.7^{+0.5}_{-0.4}$	$(4.5^{+0.6}_{-0.6}) \times 10^{-9}$	$(7.8^{+0.7}_{-0.7}) \times 10^{-2}$	
	SiO	—'—	$(7.0^{+0.3}_{-0.3}) \times 10^{13}$	$238.3^{+0.1}_{-0.1}$	$6.5^{+0.2}_{-0.2}$	$(2.6^{+0.3}_{-0.3}) \times 10^{-10}$	$(4.6^{+0.3}_{-0.3}) \times 10^{-3}$	
	DCN	—'—	$(1.1^{+0.2}_{-0.2}) \times 10^{13}$	$238.8^{+0.4}_{-0.4}$	$4.4^{+1.0}_{-0.8}$	$(3.9^{+0.8}_{-1.2}) \times 10^{-11}$	$(6.9^{+1.3}_{-1.2}) \times 10^{-4}$	
	OCS	—'—	$(8.5^{+0.5}_{-0.5}) \times 10^{14}$	$239.2^{+0.2}_{-0.2}$	$5.2^{+0.4}_{-0.3}$	$(3.2^{+0.4}_{-0.4}) \times 10^{-9}$	$(5.6^{+0.5}_{-0.4}) \times 10^{-2}$	
	¹³ CS	—'—	$(6.4^{+0.5}_{-0.4}) \times 10^{13}$	$238.9^{+0.2}_{-0.1}$	$4.4^{+0.3}_{-0.3}$	$(2.4^{+0.3}_{-0.3}) \times 10^{-10}$	$(4.2^{+0.4}_{-0.3}) \times 10^{-3}$	
	c-C ₃ H ₂	$12.5^{+3.1}_{-2.1}$	$(2.0^{+0.7}_{-0.5}) \times 10^{13}$	$237.6^{+0.3}_{-0.3}$	$3.7^{+0.7}_{-0.8}$	$(7.4^{+2.9}_{-2.0}) \times 10^{-11}$	$(1.3^{+0.5}_{-0.3}) \times 10^{-3}$	
	N 113 B3	CH ₃ OH	$132.9^{+15.1}_{-16.4}$	$(6.2^{+0.7}_{-0.8}) \times 10^{15}$	$231.8^{+0.5}_{-0.5}$	$7.9^{+0.2}_{-0.2}$	$(5.0^{+1.0}_{-1.0}) \times 10^{-8}$...
		HCOOCH ₃	—'—	$<3.1 \times 10^{14}$	231.9 ^a	7.9 ^a	$<2.5 \times 10^{-9}$	$<5.1 \times 10^{-2}$
		CH ₃ OCH ₃	—'—	$(8.7^{+1.6}_{-2.1}) \times 10^{14}$	231.9 ^a	7.9 ^a	$(7.0^{+2.0}_{-2.1}) \times 10^{-9}$	$(1.4^{+0.4}_{-0.4}) \times 10^{-1}$
		³³ SO	—'—	$(4.3^{+1.6}_{-2.0}) \times 10^{13}$	231.9 ^a	7.9 ^a	$(3.5^{+1.4}_{-1.7}) \times 10^{-10}$	$(7.0^{+2.7}_{-3.4}) \times 10^{-3}$
		SO ₂	—'—	$(1.0^{+0.2}_{-0.2}) \times 10^{15}$	$232.1^{+1.4}_{-1.1}$	$11.3^{+3.2}_{-2.7}$	$(8.2^{+2.3}_{-2.3}) \times 10^{-9}$	$(1.6^{+0.4}_{-0.4}) \times 10^{-1}$
H ₂ S		—'—	$(5.7^{+0.9}_{-0.7}) \times 10^{14}$	$233.3^{+0.2}_{-0.2}$	$3.8^{+0.5}_{-0.4}$	$(4.6^{+1.0}_{-0.9}) \times 10^{-9}$	$(9.3^{+1.9}_{-1.6}) \times 10^{-2}$	
SiO		—'—	$(7.3^{+0.7}_{-0.6}) \times 10^{13}$	$234.0^{+0.2}_{-0.2}$	$14.4^{+0.5}_{-0.4}$	$(5.9^{+1.1}_{-1.1}) \times 10^{-10}$	$(1.2^{+0.2}_{-0.2}) \times 10^{-2}$	
DCN		—'—	$(1.8^{+0.3}_{-0.2}) \times 10^{13}$	$233.0^{+0.2}_{-0.2}$	$5.0^{+0.5}_{-0.5}$	$(1.5^{+0.3}_{-0.3}) \times 10^{-10}$	$(3.0^{+0.6}_{-0.5}) \times 10^{-3}$	
OCS		—'—	$(4.2^{+0.5}_{-0.5}) \times 10^{14}$	$232.6^{+0.4}_{-0.5}$	$6.8^{+1.2}_{-0.8}$	$(3.4^{+0.7}_{-0.7}) \times 10^{-9}$	$(6.8^{+1.2}_{-1.2}) \times 10^{-2}$	
¹³ CS		—'—	$(4.2^{+0.6}_{-0.4}) \times 10^{13}$	$233.4^{+0.2}_{-0.2}$	$4.6^{+0.4}_{-0.4}$	$(3.4^{+0.7}_{-0.6}) \times 10^{-10}$	$(6.8^{+1.3}_{-1.1}) \times 10^{-3}$	
c-C ₃ H ₂		$26.3^{+18.6}_{-8.0}$	$(1.9^{+0.4}_{-0.2}) \times 10^{13}$	$234.3^{+0.3}_{-0.3}$	$4.8^{+0.8}_{-0.6}$	$(1.5^{+0.4}_{-0.3}) \times 10^{-10}$	$(3.1^{+0.7}_{-0.5}) \times 10^{-3}$	

Note.

^a For some molecules with noisy or tentative line detections, reliable parameter error estimates could not be obtained using the Monte Carlo resampling method. In these cases, v_{LSR} or both v_{LSR} and Δv_{FWHM} were held fixed at the value given by the initial least-squares fit, with the other parameters allowed to vary freely (see Section 4.3 for details).

Table 7
Results of XCLASS LTE SO₂ Fitting for Hot Cores N 105-2 A and 2 B^{a,b}

Component	Source Size ($''$)	$T_{\text{rot}}(\text{SO}_2)$ (K)	$N(\text{SO}_2)$ (cm^{-2})	v_{LSR} (km s^{-1})	Δv_{FWHM} (km s^{-1})
N105-2 A					
1	1.00 [0.58, 1.70]	47 [83, 207]	$(3.0 [0.6, 9.4]) \times 10^{14}$	242.2 [241.7, 243.6]	5.6 [2.3, 4.5]
2	0.05 [0.04, 0.15]	102 [40, 178]	$(2.0 [0.1, 2.0]) \times 10^{17}$	242.6 [241.9, 243.4]	2.1 [2.6, 5.1]
N105-2 B					
1	1.24 [0.34, 1.68]	46 [43, 76]	$(8.4 [9.7, 21.3]) \times 10^{14}$	241.7 [242.9, 245.8]	8.1 [8.7, 10.0]
2	0.05 [0.07, 0.84]	139 [105, 275]	$(5.8 [0.01, 2.5]) \times 10^{17}$	244.8 [241.2, 247.7]	10.5 [8.2, 12.3]

Notes.

^a For each parameter, the best χ^2 value is given, as well as the Bayesian credibility intervals calculated by an MCMC error estimate (orange and black dashed lines in Figures A1–A2, respectively).

^b For comparison, we provide the results of the SO₂ single-component rotational diagram analysis for N105-2 A and 2 B: $[T_{\text{rot}}, N] = [134.1^{+2.1}_{-2.1}, (1.61 \pm 0.05) \times 10^{15}]$ for 2 A and $[122.9 \pm 1.0, (3.53 \pm 0.05) \times 10^{15}]$ for 2 B (see Section 4.3).

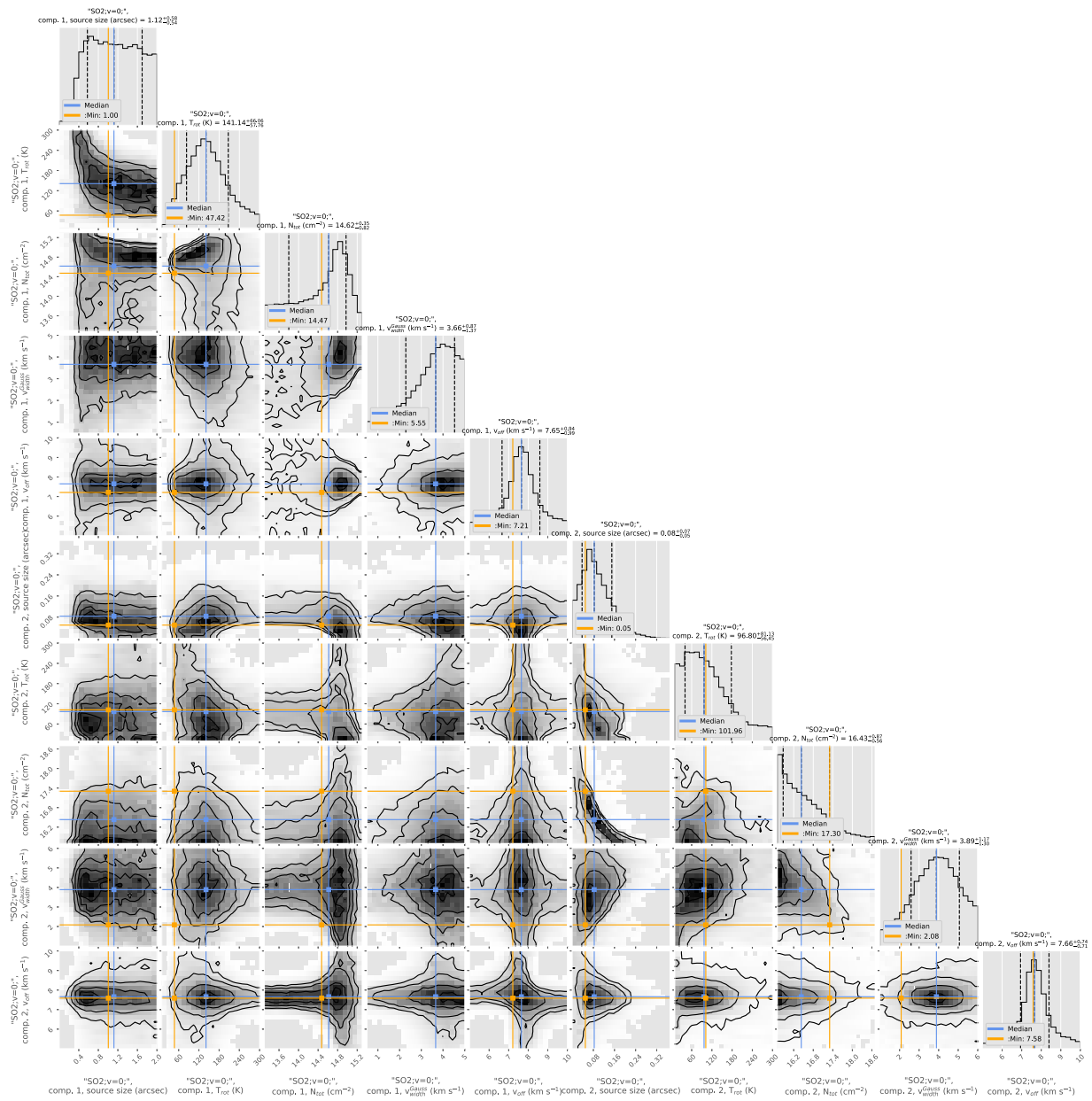
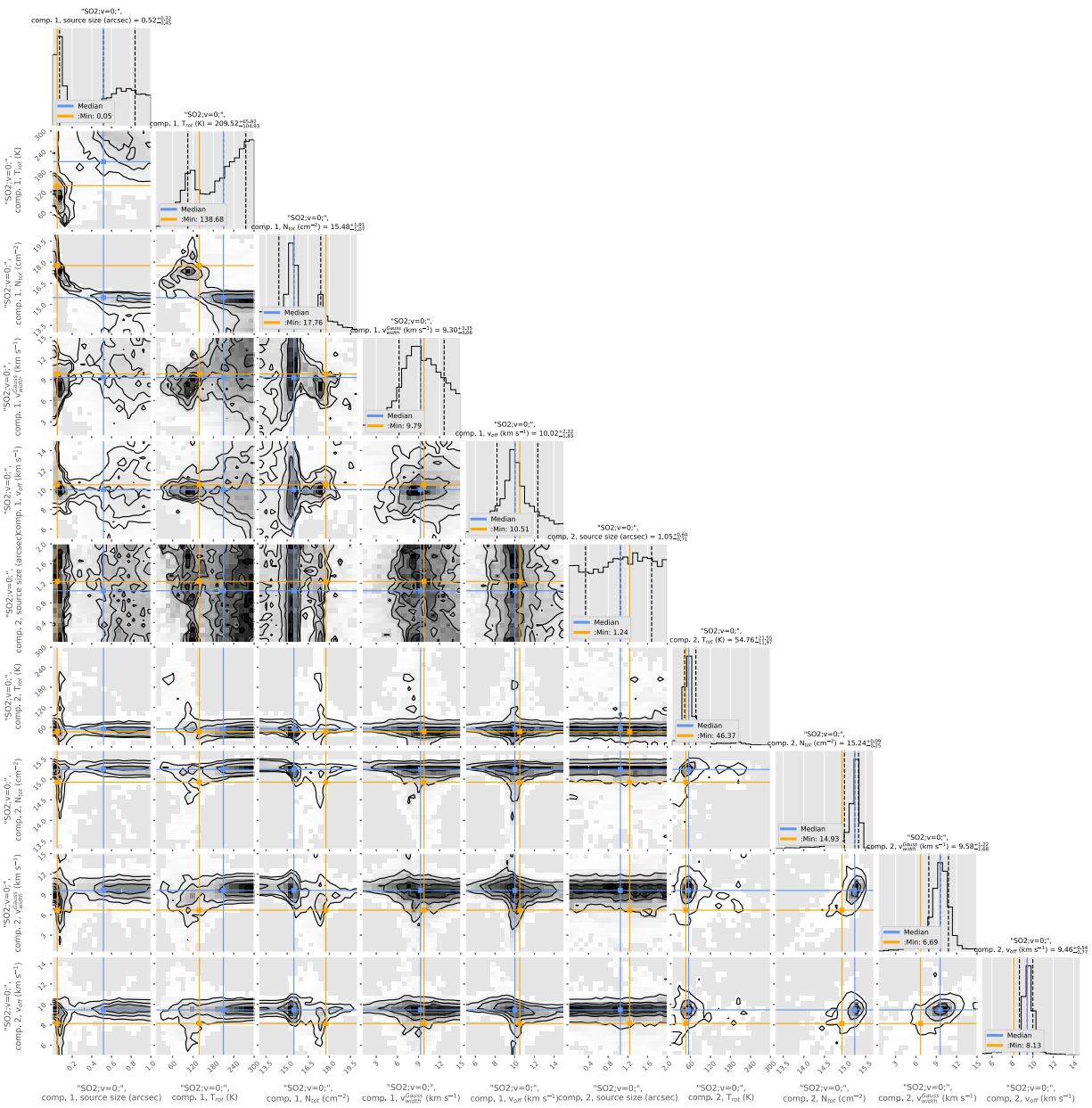


Figure A1. Corner plot of the MCMC error estimate for the XCLASS LTE SO₂ fit for N 105–2 A. The 16% and 84% quantiles are plotted as black dashed lines, the 50% quantile (median) is shown in blue, while the lowest χ^2 value is shown in orange. For very asymmetric distributions, the lowest χ^2 value is at quite some distance from the median, at or even beyond the limits of the credibility interval.



Appendix B Observed Spectra and Model Fits

In Figures B2–B15, we present the ALMA Band 6 spectra from all four spectral windows covered by our observations (1 A–1 C, 2 A–2 D, 2 F) or selected subwindows with line detections (2 E, 3 A–3 C) for each continuum source analyzed in this paper. The spectra of hot cores 2 A and 2 B are shown first (Figures B2–B5). The spectral extraction method is described in Section 4, and Figure B1 shows the spectral

extraction regions overlaid on the 1.2 mm continuum images. The synthetic spectra are overlaid on the observed spectra in Figures B2–B15. The spectral line modeling method and the fitting results are discussed in Section 4.3. Figure B16 shows the ALMA spectra of the N 113 A1 and B3 hot cores for two spectral windows in Band 6, first reported in Sewiło et al. (2018). Here, we present the synthetic spectra obtained in the reanalysis of the data following the methods used for N 105 (see Section 4.3).

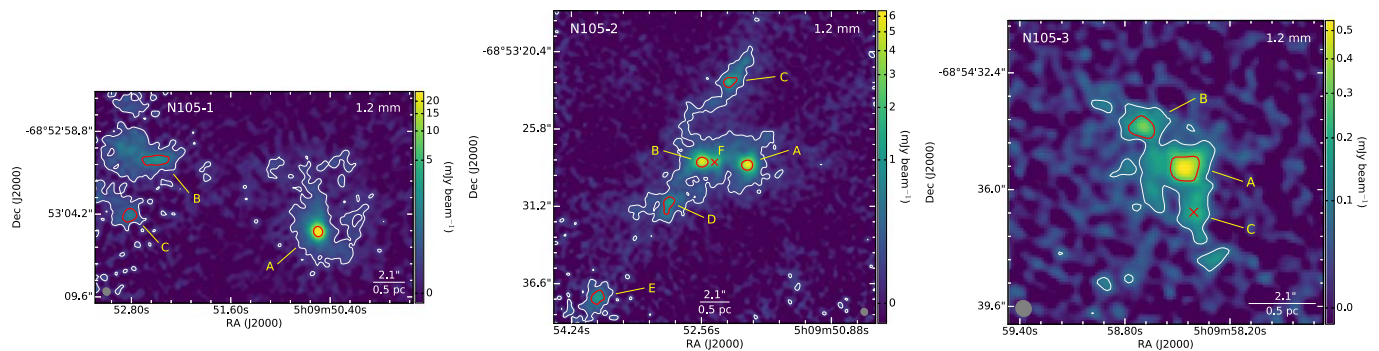


Figure B1. The 1.2 mm continuum images of N 105–1 (left), N 105–2 (center), and N 105–3 (right) with spectral extraction regions indicated in red; they are contours corresponding to 50% of the 1.2 mm continuum peak of individual sources (see Section 4 for details). White contours represent the 3σ -level continuum emission (as in Figure 3).

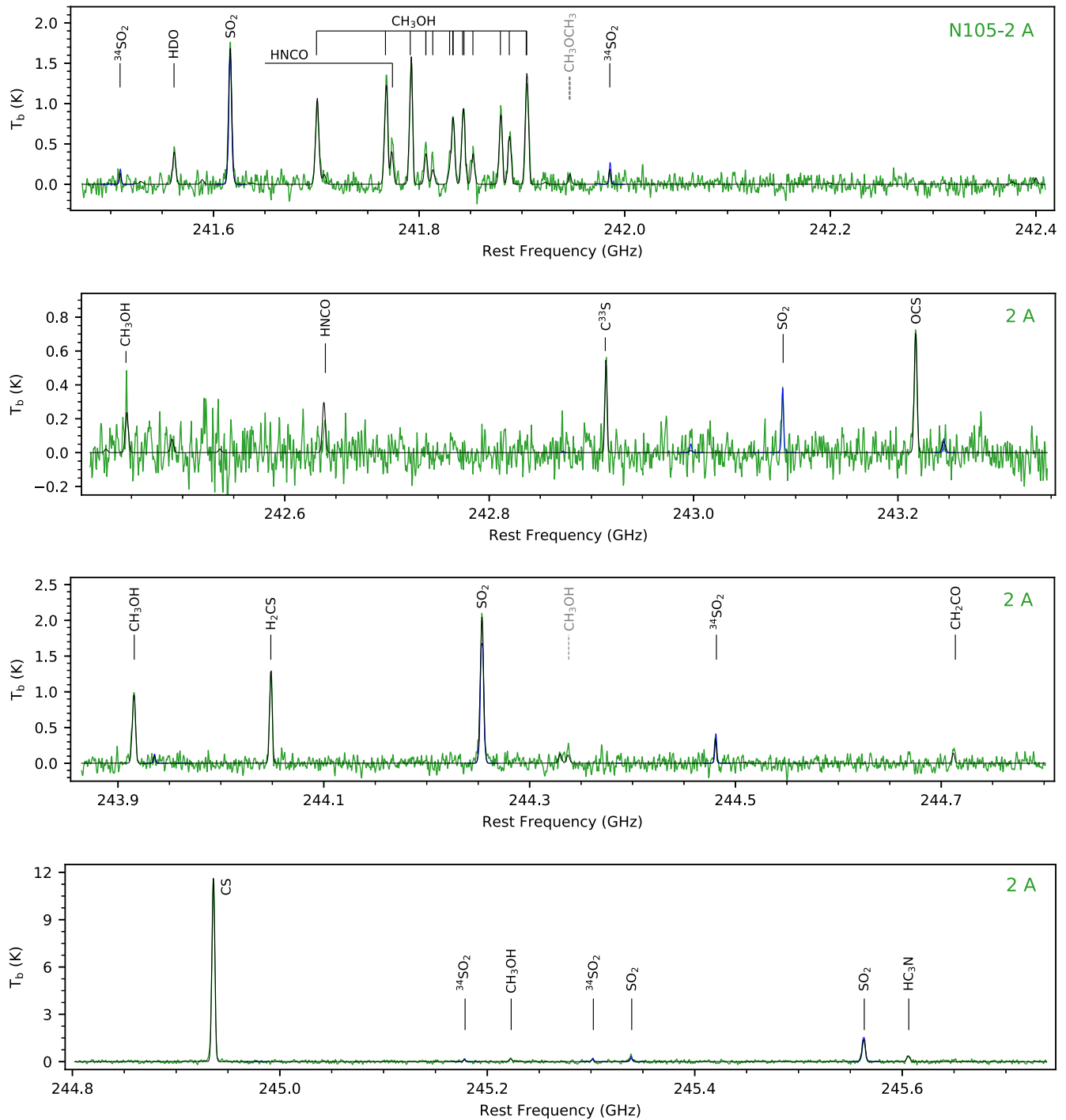


Figure B2. ALMA Band 6 spectra of the N 105-2 A hot core in the ~ 242 GHz (top two panels) and ~ 245 GHz (bottom two panels) spectral windows. The detected (black) and tentatively detected (gray) spectral lines are labeled (see also Table 1). The LTE synthetic spectra including all species and described in Section 4.3 are shown in black. The SO_2 transition at ~ 243.09 GHz is not present in these models because it was not possible to achieve a satisfactory fit to this line; it was excluded from the analysis to improve the overall fit. The XCLASS LTE synthetic spectra of SO_2 and $^{34}\text{SO}_2$ are shown in blue and include the SO_2 transition at ~ 243.09 GHz (see Section 4.3.1).

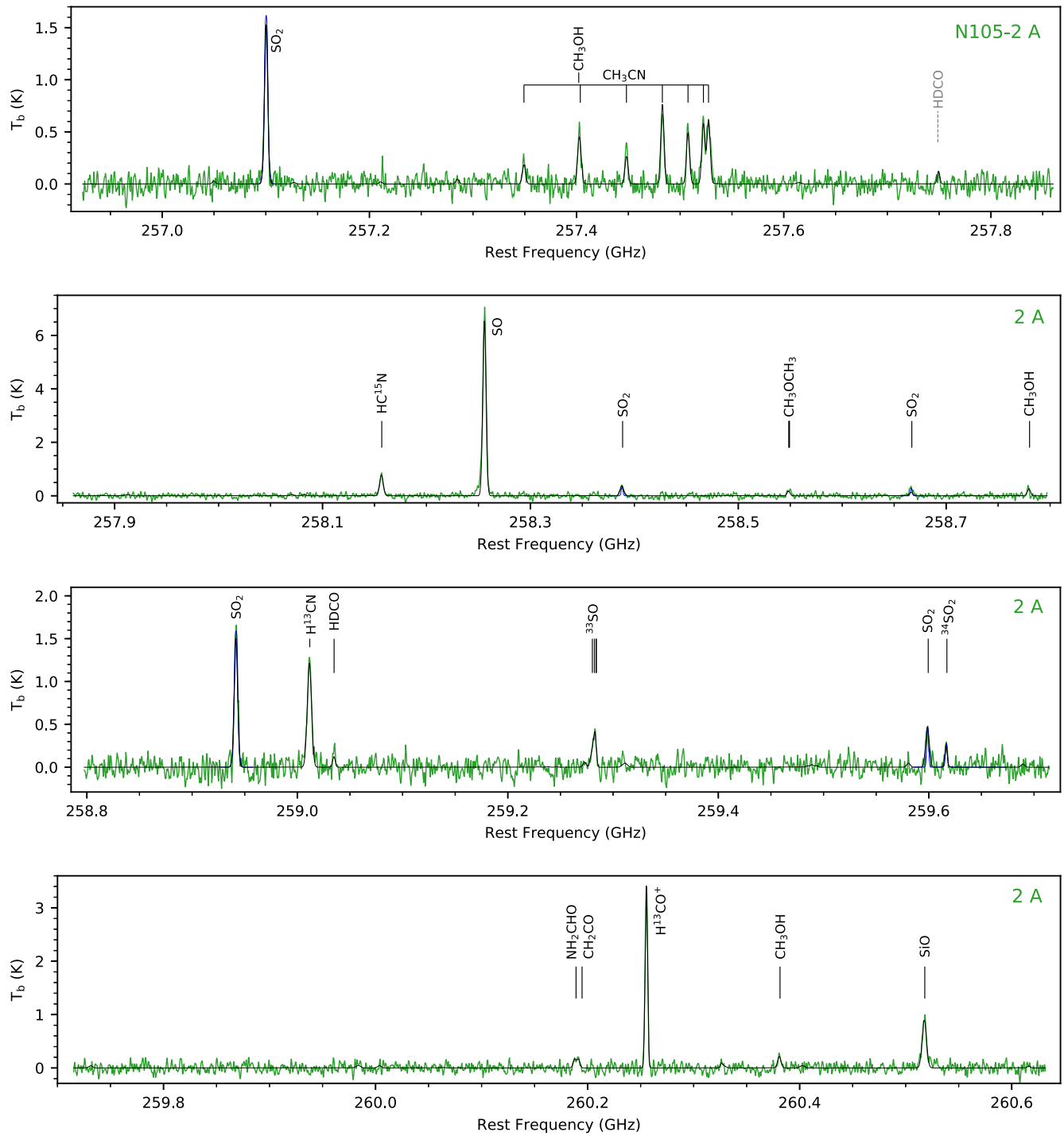


Figure B3. Same as Figure B2 but for the ~258 GHz (top two panels) and ~260 GHz (bottom two panels) spectral windows.

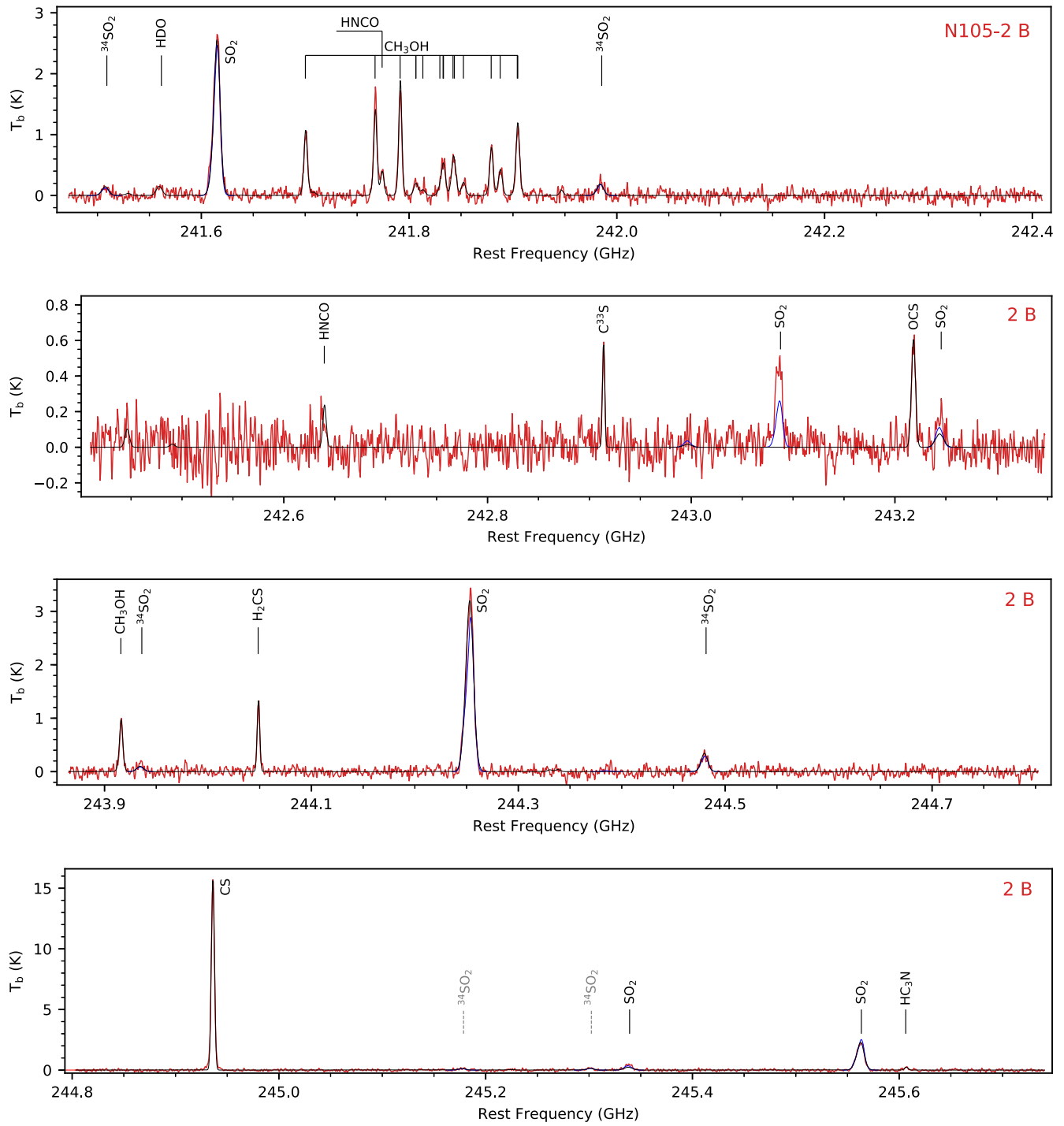


Figure B4. Same as Figure B2 but for the N 105-2 B hot core.

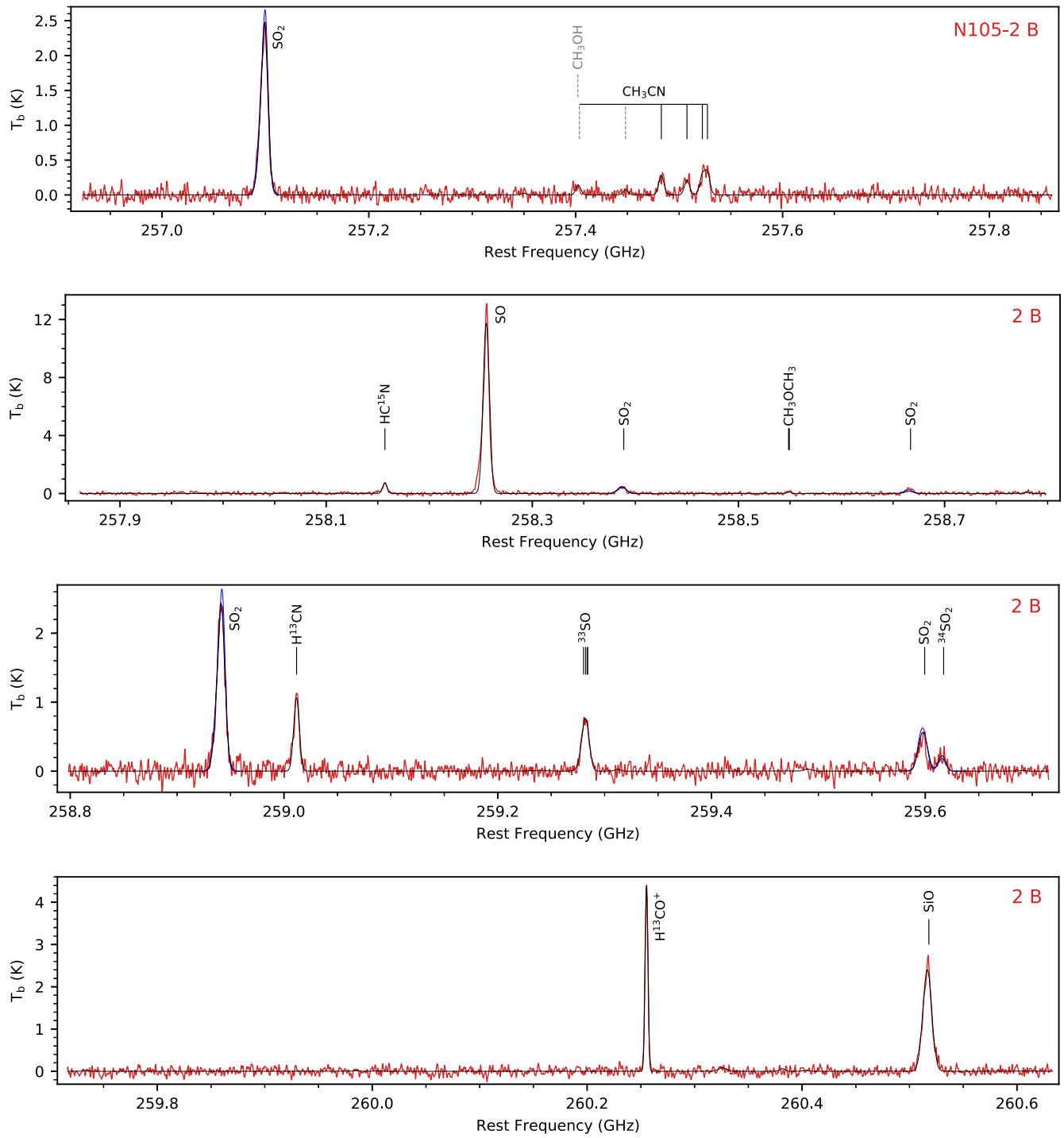


Figure B5. Same as Figure B3 but for the N 105–2 B hot core.

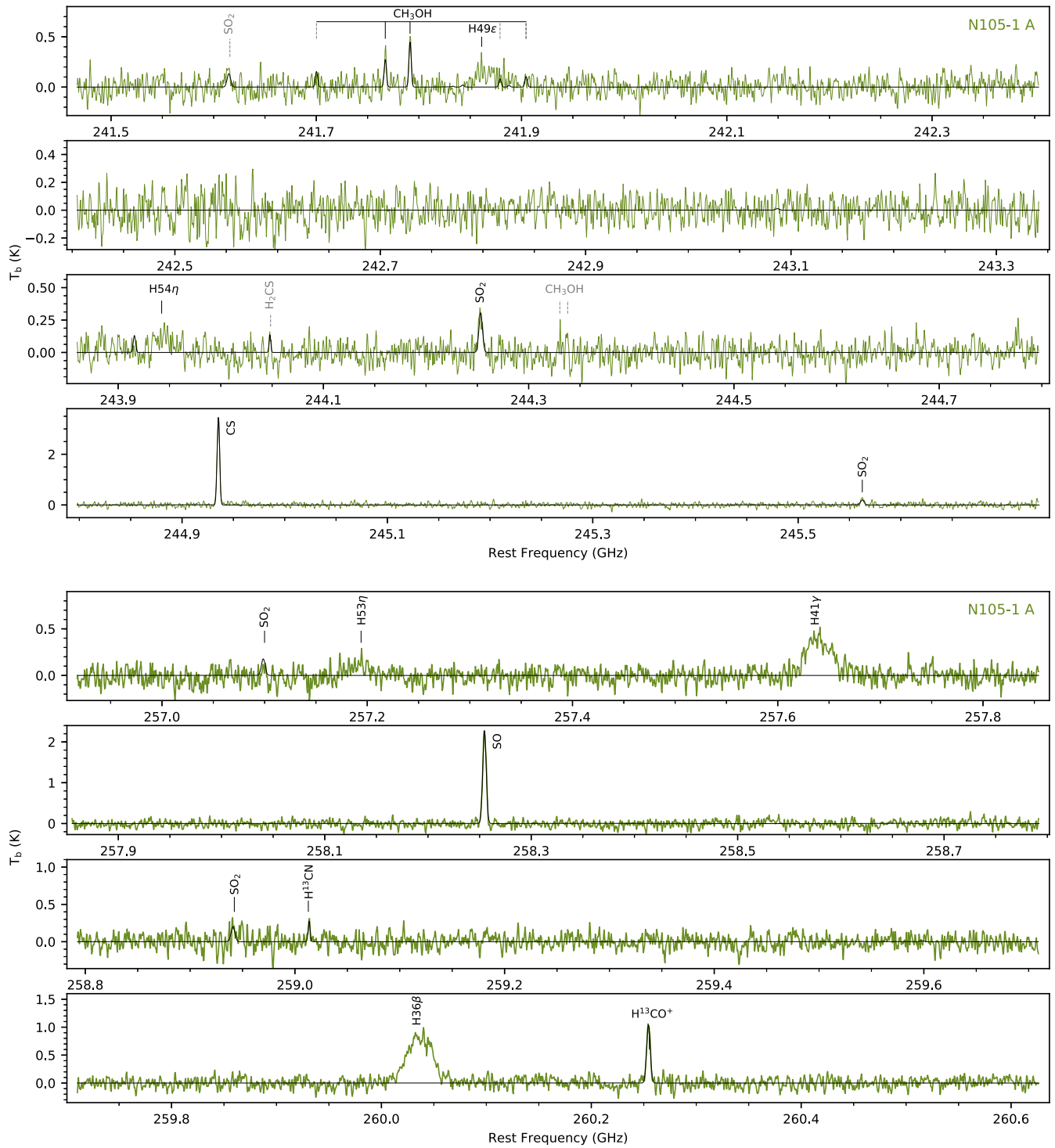


Figure B6. Same as Figure B2 (top) and Figure B3 (bottom) but for source N 105-1 A.

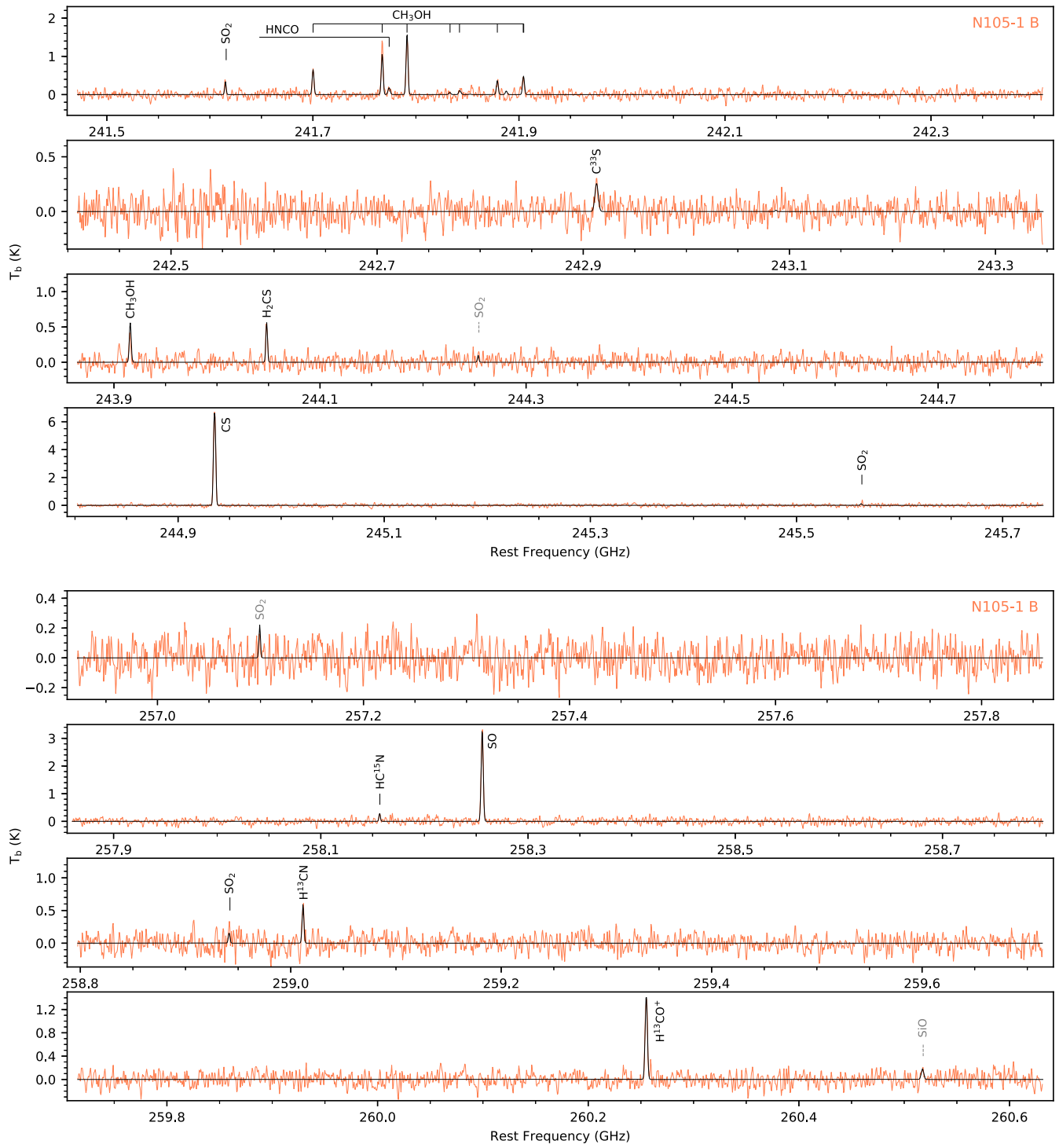


Figure B7. Same as Figure B2 (top) and Figure B3 (bottom) but for source N 105-1 B.

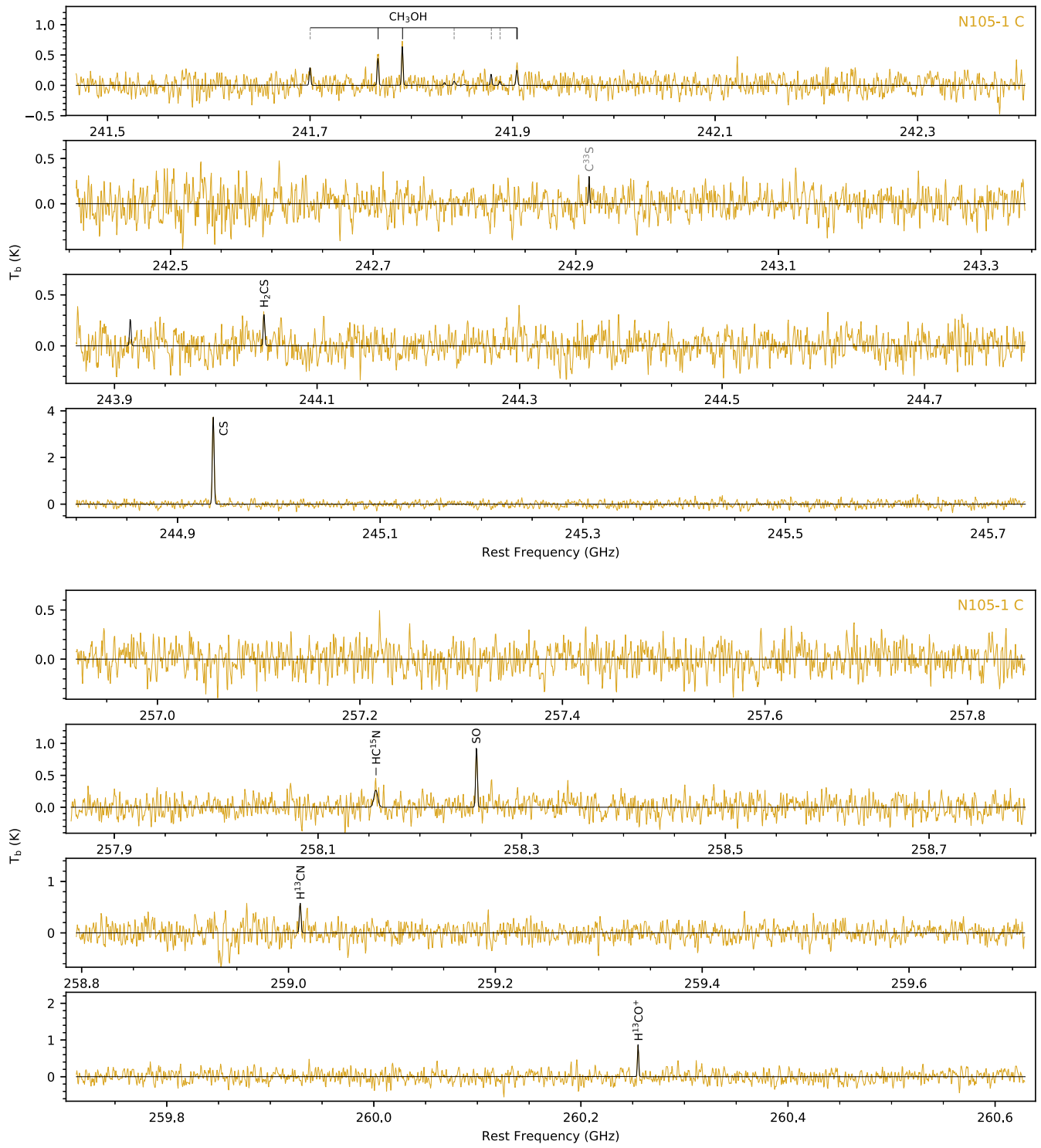


Figure B8. Same as Figure B2 (top) and Figure B3 (bottom) but for source N 105-1 C.

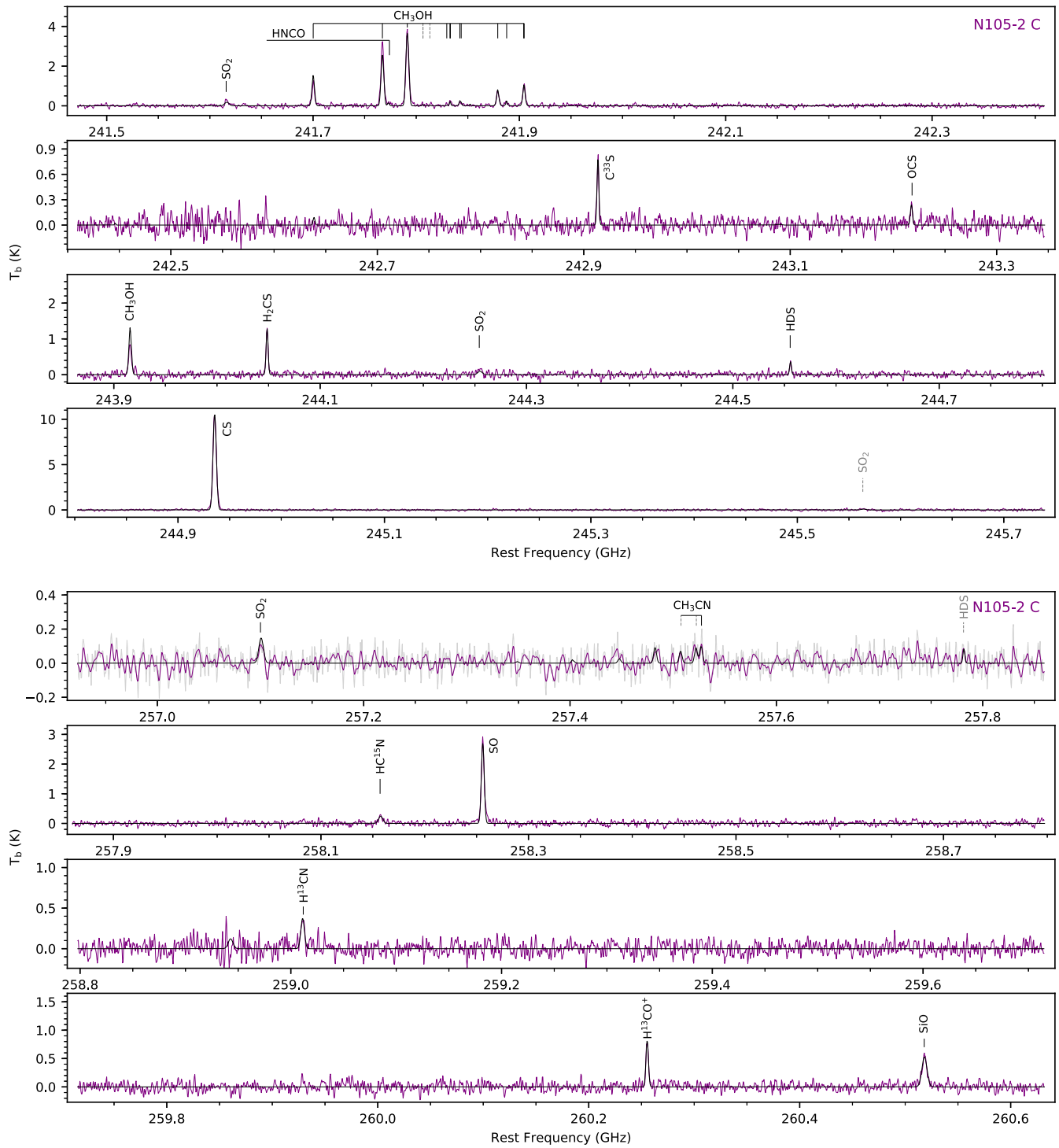


Figure B9. Same as Figure B2 (top) and Figure B3 (bottom) but for source N105-2 C. In the plot at the top of the lower panel, the observed spectrum is shown in gray, while the Hanning-smoothed spectrum is shown in purple to highlight the detection of the CH₃CN lines. The observed spectrum is shown in purple in all the other plots.

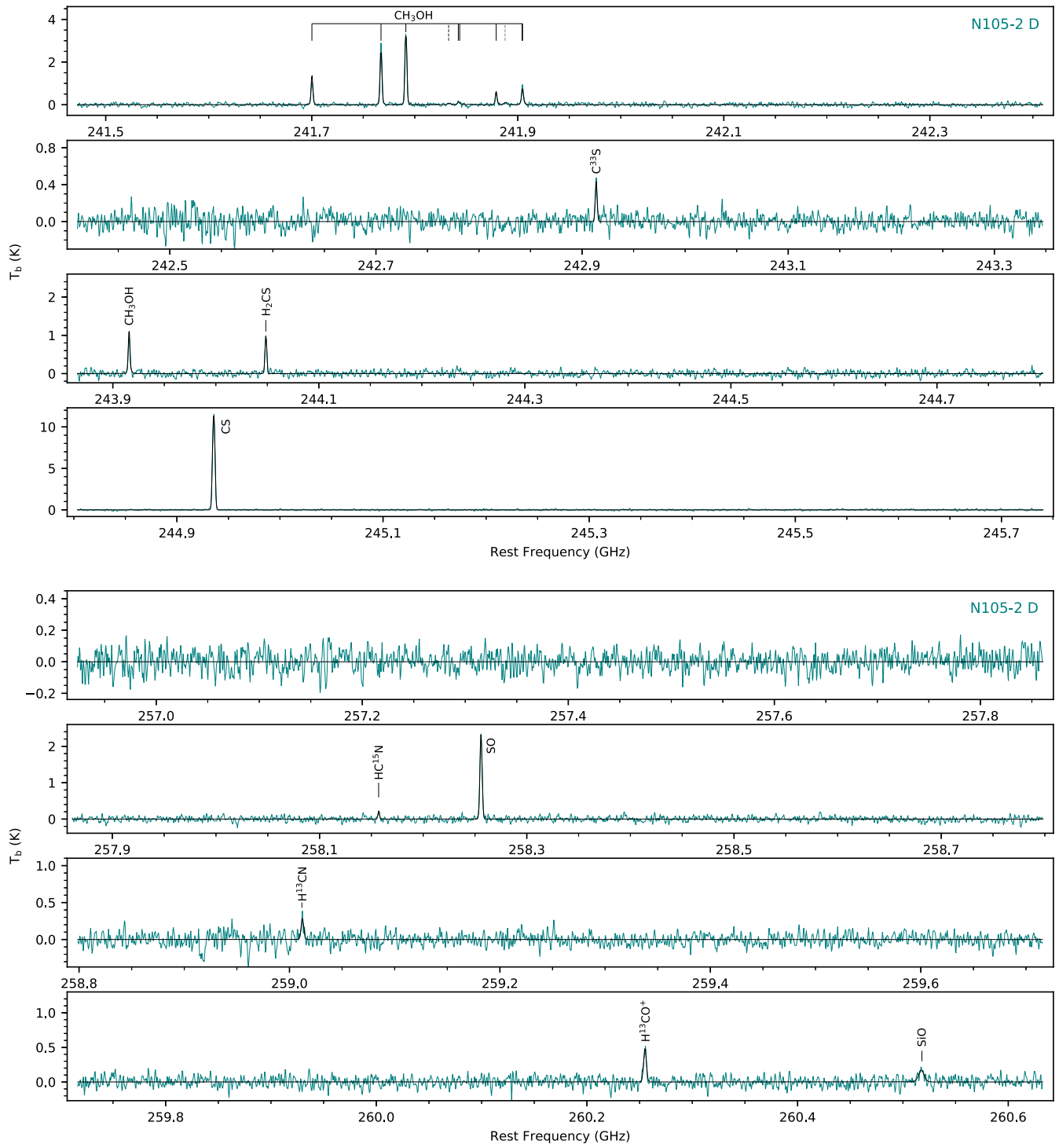


Figure B10. Same as Figure B2 (top) and Figure B3 (bottom) but for source N 105-2 D.

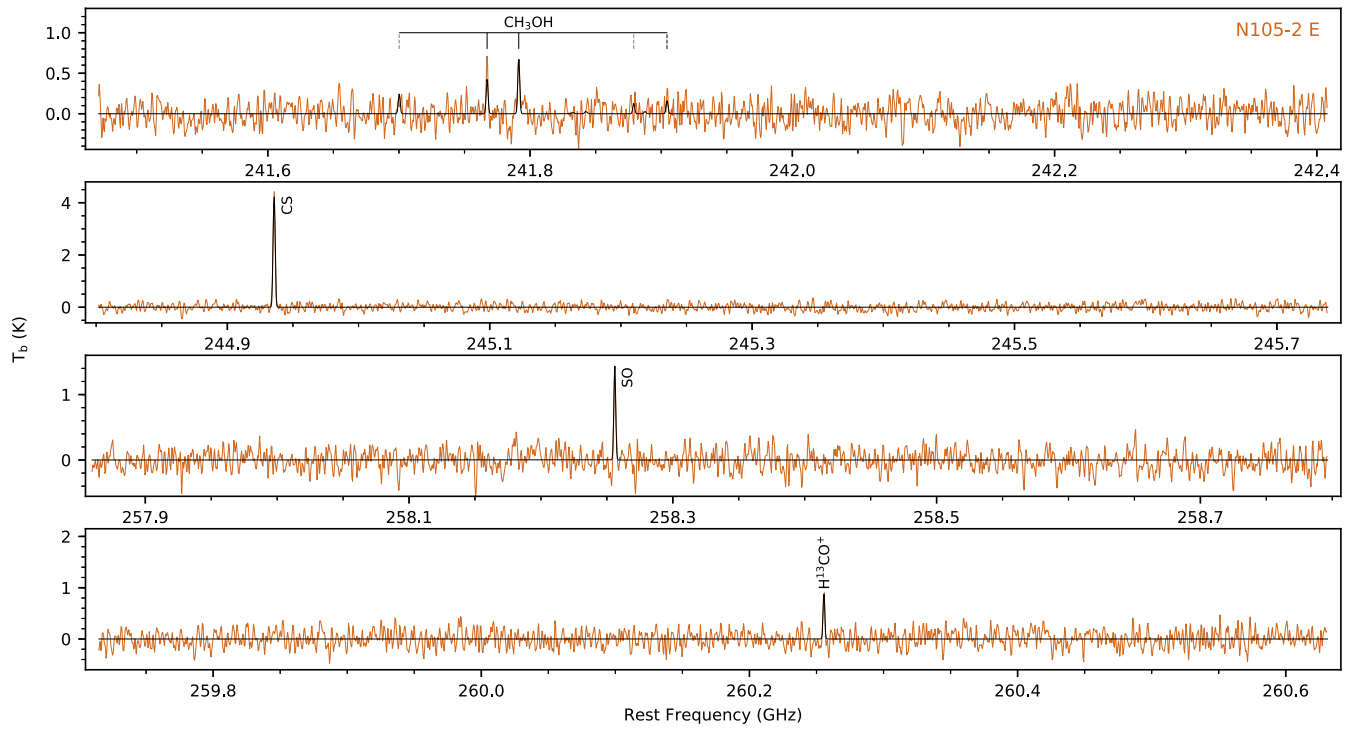


Figure B11. Subset of plots shown in Figures B2 and B3 for 2 A but for source N 105–2 E; only spectral ranges with line detections are shown.

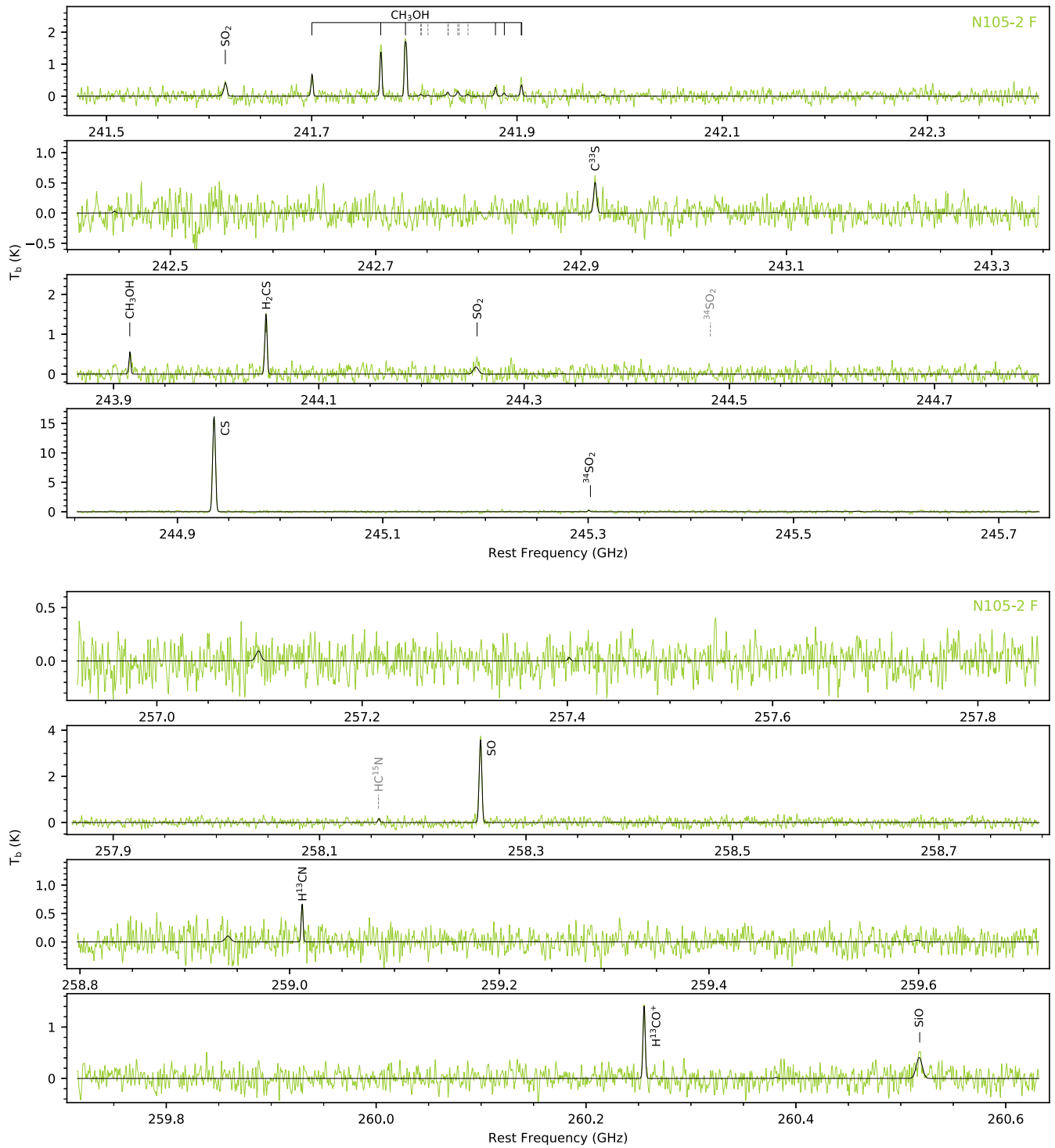


Figure B12. Subset of plots shown in Figures B2 and B3 for 2 A but for source N 105–2 E; only spectral ranges with line detections are shown.

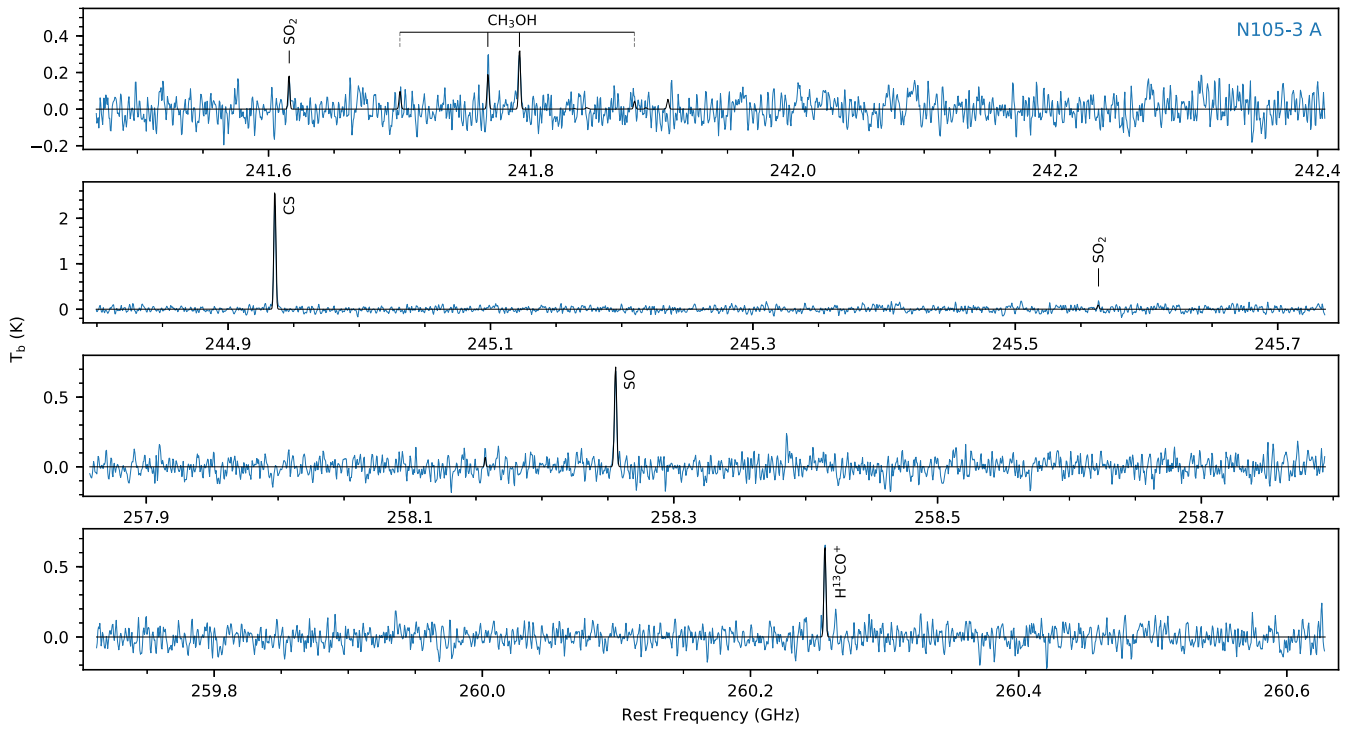


Figure B13. Same as Figure B11 but for source N 105-3 A.

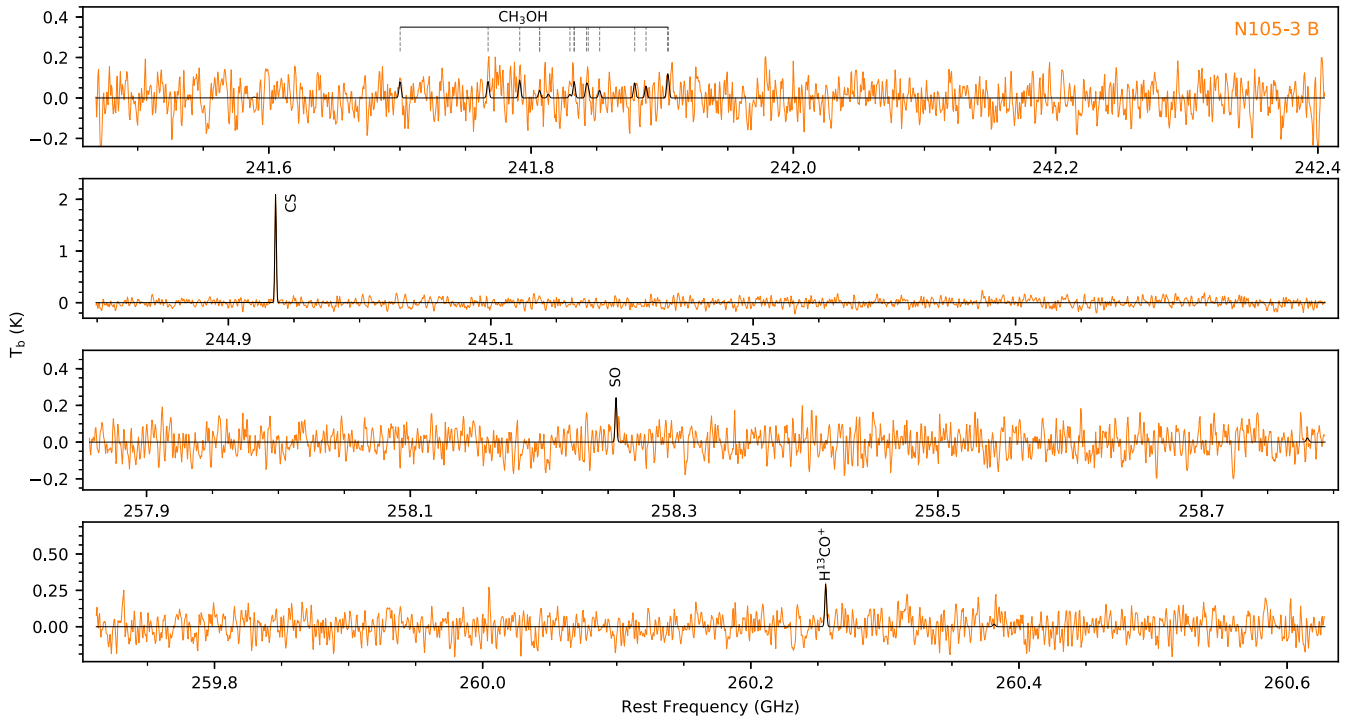


Figure B14. Same as Figure B11 but for source N 105-3 B.

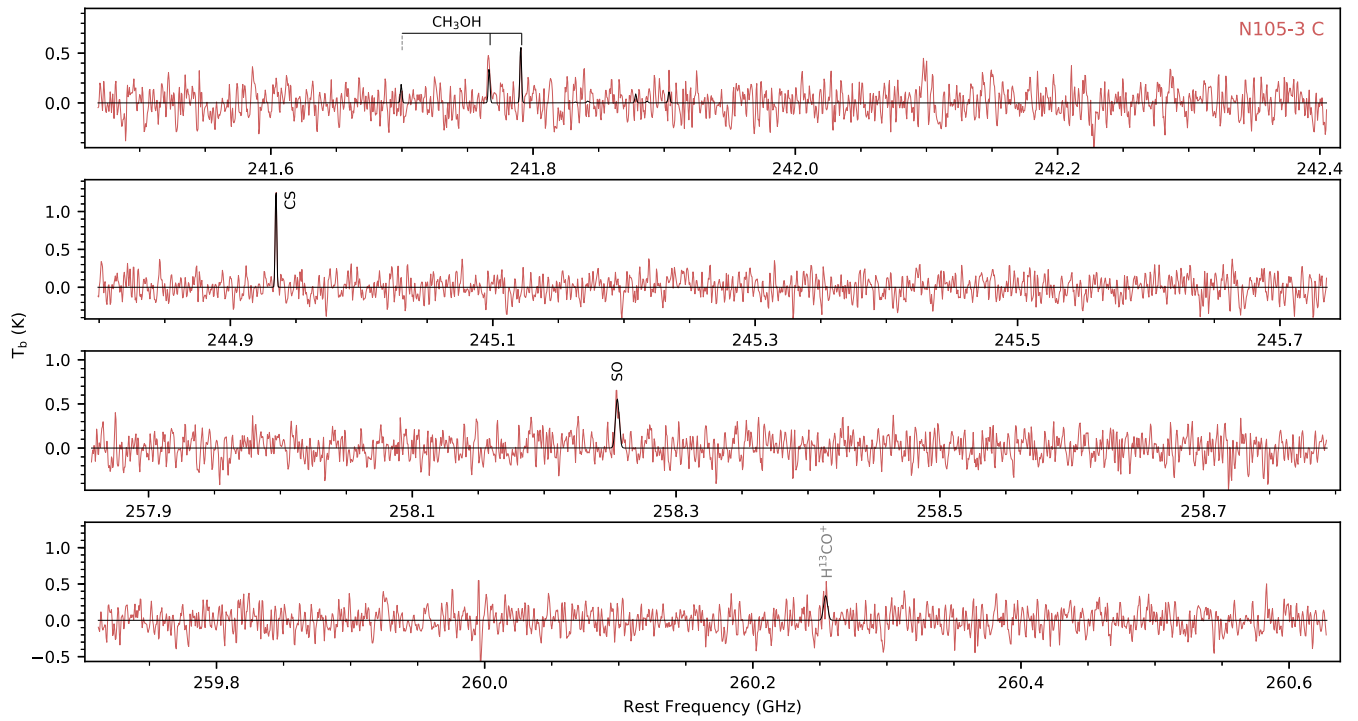


Figure B15. Same as Figure B11 but for source N 105-3 C.

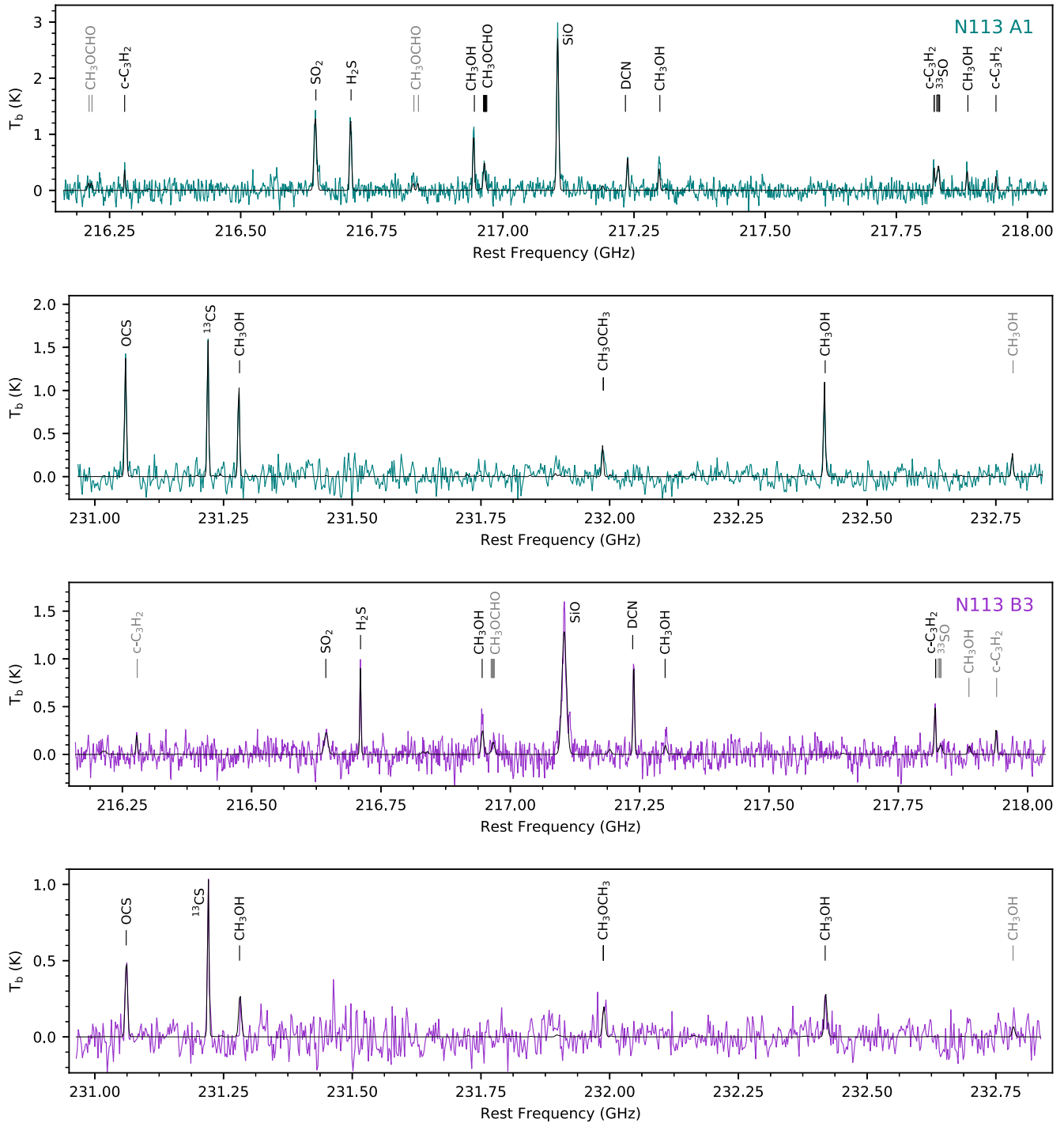


Figure B16. ALMA spectra of the N 113 A1 (top two panels) and B3 (bottom two panels) hot cores for two spectral windows in Band 6. The spectra were first reported in Sewilo et al. (2018). Here, we present the synthetic spectra (shown in black) obtained in the reanalysis of the data following the methods used for N 105 (see Section 4.3). The detected (black) and tentatively detected (gray) spectral lines are labeled (see also Table 1 in Sewilo et al. 2018).

Appendix C N 105 Star-forming Region at Far-infrared and Radio Wavelengths

In Figure C1, we present a three-color mosaic combining the longer wavelength images of N 105: Spitzer/SAGE Multiband Imaging Photometer for Spitzer (MIPS) $24\ \mu\text{m}$ (Meixner et al. 2006; SAGE Team 2006), Herschel Inventory of the Agents of Galaxy Evolution (HERITAGE) Photoconductor Array

Camera and Spectrometer (PACS) $100\ \mu\text{m}$, and Spectral and Photometric Imaging Receiver (SPIRE) $250\ \mu\text{m}$ images (Meixner et al. 2013; HERITAGE Team 2013); the observed ALMA fields N 105–1, N 105–2, and N 105–3 are indicated. Figure C2 shows each image separately with the 3σ 1.2 mm continuum contour overlaid. The ATCA 4.8 and 8.6 GHz radio images from Indebetouw et al. (2004) covering the ALMA N 105–1 and N 105–2 fields are presented in Figure C3.

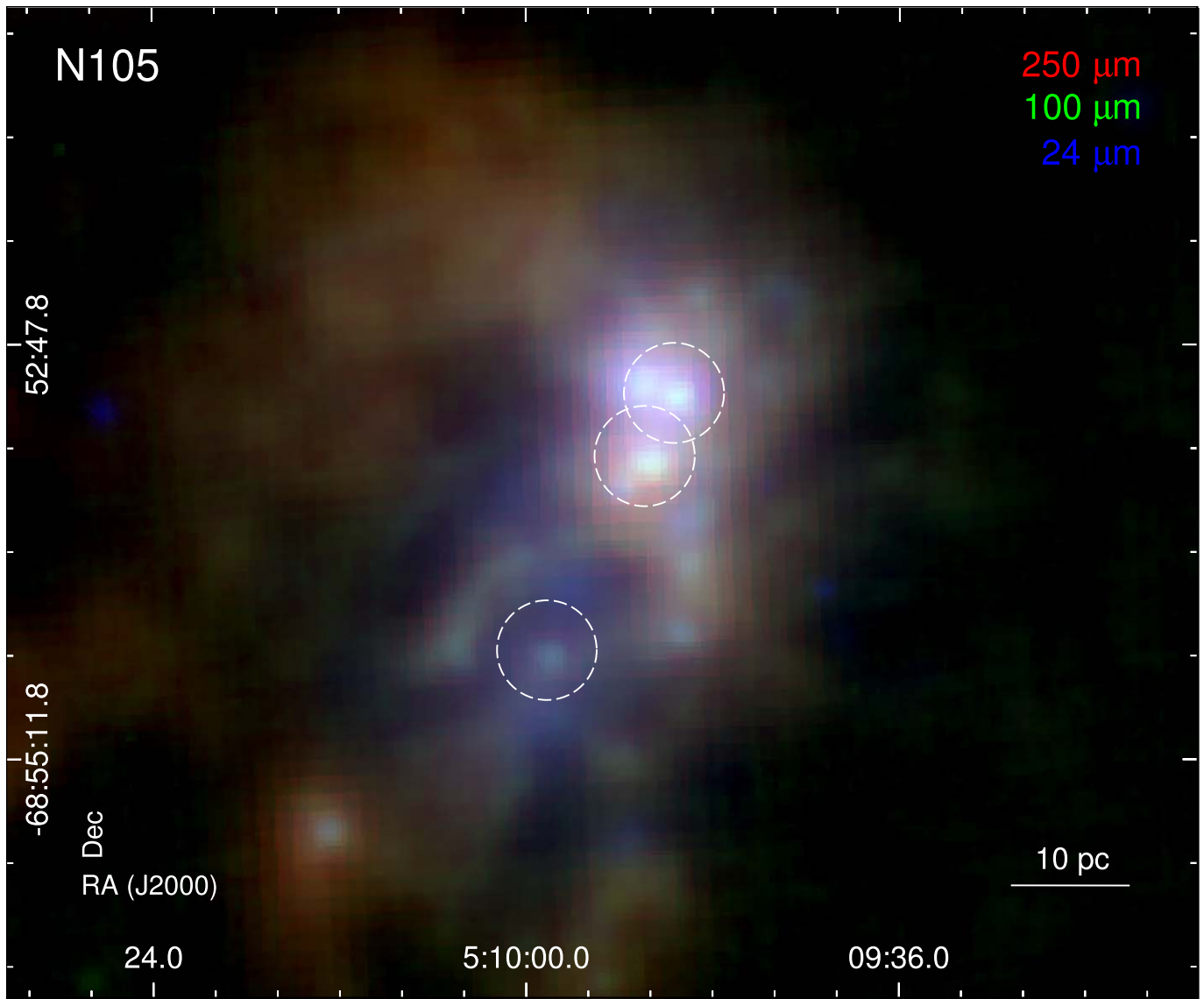


Figure C1. Three-color mosaic of N 105 combining the Spitzer/SAGE MIPS 24 μm (blue), Herschel/HERITAGE PACS 100 μm (green), and SPIRE 250 μm (red) images. Three ALMA pointings are indicated (from northwest to southeast): N 105-1, N 105-2, and N 105-3.

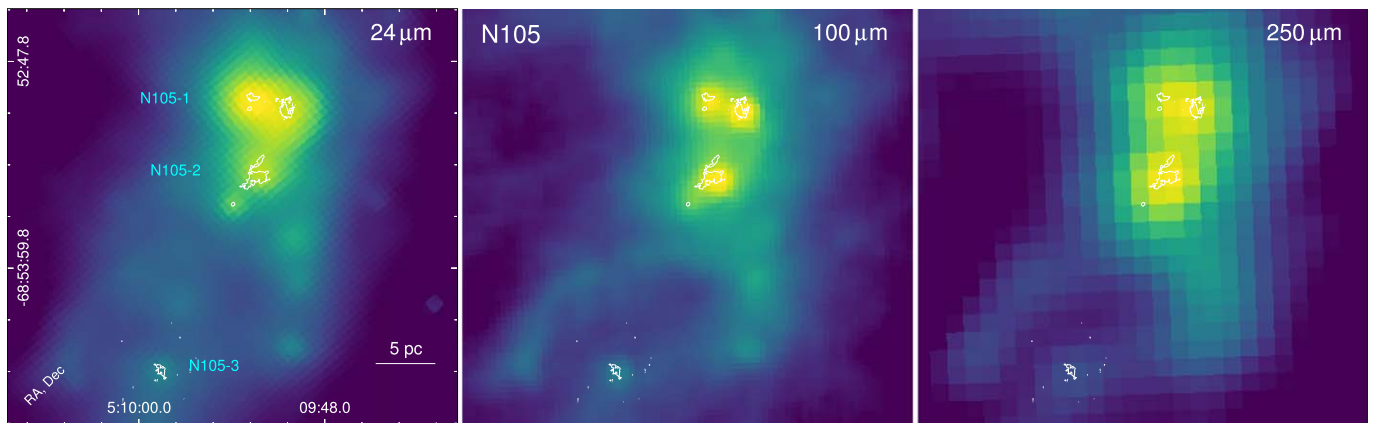


Figure C2. The Spitzer/SAGE MIPS 24 μm (left), Herschel/HERITAGE PACS 100 μm (center), and SPIRE 250 μm (right) images of the N 105 star-forming region. The 3σ ALMA contours are overlaid for reference.

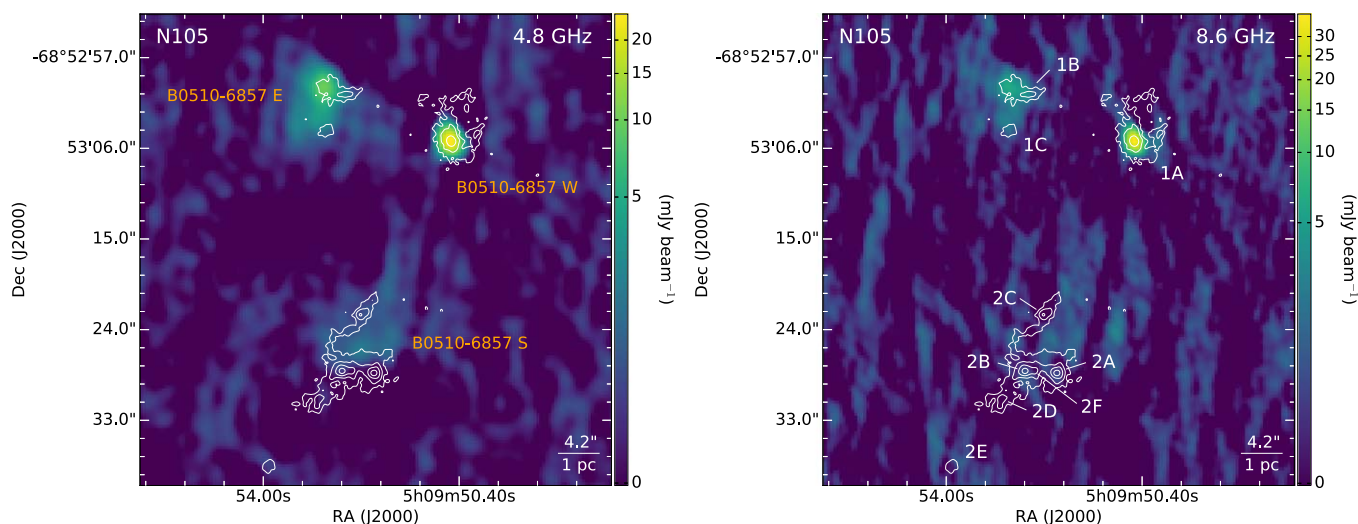


Figure C3. The ATCA 4.8 GHz (6 cm; left) and 8.6 GHz (3 cm; right) images of N 105 (Indebetouw et al. 2004) covering the ALMA N 105–1 (sources 1 A–1 C) and N 105–2 (sources 2 A–2 F) fields. The 1.2 mm continuum contours are overlaid with contour levels of (3, 10, 100) σ_1 with $\sigma_1 = 6.8 \times 10^{-5}$ Jy beam $^{-1}$ for N 105–1 and (3, 10, 30, 80) σ_2 with $\sigma_2 = 5.0 \times 10^{-5}$ Jy beam $^{-1}$ for N 105–2. The ATCA 4.8 GHz/ 8.6 GHz radio continuum sources and ALMA 1.2 mm continuum sources are labeled in the left and right panel, respectively. The synthesized beam sizes are $2''.19 \times 1''.70$ and $1''.82 \times 1''.24$ for 4.8 GHz and 8.6 GHz images, respectively.

ORCID iDs

Marta Sewilo <https://orcid.org/0000-0003-2248-6032>
 Martin Cordiner <https://orcid.org/0000-0001-8233-2436>
 Steven B. Charnley <https://orcid.org/0000-0001-6752-5109>
 Joana M. Oliveira <https://orcid.org/0000-0002-0861-7094>
 Emmanuel Garcia-Berrios <https://orcid.org/0000-0002-1069-2931>
 Peter Schilke <https://orcid.org/0000-0003-2141-5689>
 Jacob L. Ward <https://orcid.org/0000-0003-3656-3713>
 Jennifer Wiseman <https://orcid.org/0000-0002-1143-6710>
 Remy Indebetouw <https://orcid.org/0000-0002-4663-6827>
 Kazuki Tokuda <https://orcid.org/0000-0002-2062-1600>
 Jacco Th. van Loon <https://orcid.org/0000-0002-1272-3017>
 Álvaro Sánchez-Monge <https://orcid.org/0000-0002-3078-9482>
 Veronica Allen <https://orcid.org/0000-0002-8021-0344>
 C.-H. Rosie Chen <https://orcid.org/0000-0002-3925-9365>
 Roya Hamedani Golshan <https://orcid.org/0000-0003-1993-2302>
 Agata Karska <https://orcid.org/0000-0001-8913-925X>
 Lars E. Kristensen <https://orcid.org/0000-0003-1159-3721>
 Stan E. Kurtz <https://orcid.org/0000-0003-4444-5602>
 Thomas Möller <https://orcid.org/0000-0002-9277-8025>
 Toshikazu Onishi <https://orcid.org/0000-0001-7826-3837>
 Sarolta Zahorecz <https://orcid.org/0000-0001-6149-1278>

References

- Abdo, A. A., Ackermann, M., Ajello, M., et al. 2010a, *A&A*, 512, A7
 Abdo, A. A., Ackermann, M., Ajello, M., et al. 2010b, *A&A*, 523, A46
 Acharyya, K., & Herbst, E. 2015, *ApJ*, 812, 142
 Acharyya, K., & Herbst, E. 2018, *ApJ*, 859, 51
 Agúndez, M., Marcelino, N., Tercero, B., et al. 2021, *A&A*, 649, L4
 Alcaino, G., & Liller, W. 1986, *MmSAI*, 57, 491
 Allen, V., van der Tak, F. F. S., Sánchez-Monge, Á., Cesaroni, R., & Beltrán, M. T. 2017, *A&A*, 603, A133
 Ambrocio-Cruz, P., Laval, A., Marcelin, M., Amram, P., & Comeron, F. 1998, *A&A*, 339, 173
 Aota, T., Inoue, T., & Aikawa, Y. 2015, *ApJ*, 799, 141
 Arce, H. G., Santiago-García, J., Jørgensen, J. K., Tafalla, M., & Bachiller, R. 2008, *ApJL*, 681, L21
 Armand, C., Baluteau, J. P., Joubert, M., Gry, C., & Cox, P. 1996, *A&A*, 306, 593
 Asplund, M., Grevesse, N., Sauval, A. J., & Scott, P. 2009, *ARA&A*, 47, 481
 Bacmann, A., Taquet, V., Faure, A., Kahane, C., & Ceccarelli, C. 2012, *A&A*, 541, L12
 Barone, V., Latouche, C., Skouteris, D., et al. 2015, *MNRAS*, 453, L31
 Bekki, K., & Chiba, M. 2007a, *PASA*, 24, 21
 Bekki, K., & Chiba, M. 2007b, *MNRAS*, 381, L16
 Bertin, M., Romanzin, C., Doronin, M., et al. 2016, *ApJL*, 817, L12
 Bianchi, E., Codella, C., Ceccarelli, C., et al. 2019, *MNRAS*, 483, 1850
 Bica, E., Claria, J. J., Dottori, H., Santos, J. F. C., J., & Piatti, A. E. 1996, *ApJS*, 102, 57
 Bisschop, S. E., Jørgensen, J. K., van Dishoeck, E. F., & de Wachter, E. B. M. 2007, *A&A*, 465, 913
 Blake, G. A., Sutton, E. C., Masson, C. R., & Phillips, T. G. 1987, *ApJ*, 315, 621
 Boogert, A. C. A., Gerakines, P. A., & Whittet, D. C. B. 2015, *ARA&A*, 53, 541
 Breysacher, J. 1981, *A&AS*, 43, 203
 Brooks, K. J., & Whiteoak, J. B. 1997, *MNRAS*, 291, 395
 Browning, M. K., Tumlinson, J., & Shull, J. M. 2003, *ApJ*, 582, 810
 Bruderer, S., Benz, A. O., Bourke, T. L., & Doty, S. D. 2009, *A&A*, 503, L13
 Brunetti, N., & Wilson, C. D. 2019, *MNRAS*, 483, 1624
 Buckle, J. V., Rodgers, S. D., Wirstrom, E. S., et al. 2006, *FaDi*, 133, 63
 Calvet, N., Muzerolle, J., Briceño, C., et al. 2004, *AJ*, 128, 1294
 Carlson, L. R., Sewilo, M., Meixner, M., Romita, K. A., & Lawton, B. 2012, *A&A*, 542, A66
 Caselli, P., & Ceccarelli, C. 2012, *A&ARv*, 20, 56
 Ceccarelli, C., Caselli, P., Fontani, F., et al. 2017, *ApJ*, 850, 176
 Ceccarelli, C., Hollenbach, D. J., & Tielens, A. G. G. M. 1996, *ApJ*, 471, 400
 Cernicharo, J., Marcelino, N., Roueff, E., et al. 2012, *ApJL*, 759, L43
 Cesaroni, R. 2005, *IAUS*, 227, 59
 Charnley, S. B. 1997, *ApJ*, 481, 396
 Charnley, S. B., & Kaufman, M. J. 2000, *ApJL*, 529, L111
 Charnley, S. B., & Rodgers, S. D. 2008, *SSRv*, 138, 59
 Chernin, L. M., Masson, C. R., & Fuller, G. A. 1994, *ApJ*, 436, 741
 Chin, Y. N., Henkel, C., Millar, T. J., Whiteoak, J. B., & Mauersberger, R. 1996, *A&A*, 312, L33
 Chin, Y.-N., Henkel, C., Whiteoak, J. B., et al. 1997, *A&A*, 317, 548
 Chuang, K. J., Fedoseev, G., Qasim, D., et al. 2018, *ApJ*, 853, 102
 Cioni, M.-R. L., Clementini, G., Girardi, L., et al. 2011, *A&A*, 527, A116
 Codella, C., Ceccarelli, C., Caselli, P., et al. 2017, *A&A*, 605, L3
 Cordiner, M. A., Charnley, S. B., Kisiel, Z., McGuire, B. A., & Kuan, Y. J. 2017, *ApJ*, 850, 187
 Coutens, A., Jørgensen, J. K., van der Wiel, M. H. D., et al. 2016, *A&A*, 590, L6
 Cox, A. N. 2000, in *Allen's Astrophysical Quantities*, ed. N. Cox. Arthur (4th ed.; New York: AIP)

- Cragg, D. M., Johns, K. P., Godfrey, P. D., & Brown, R. D. 1992, *MNRAS*, **259**, 203
- Cross, N. J. G., Collins, R. S., Mann, R. G., et al. 2012, *A&A*, **548**, A119
- Crowther, P. A. 2007, *ARA&A*, **45**, 177
- Cyganowski, C. J., Brogan, C. L., Hunter, T. R., Churchwell, E., & Zhang, Q. 2011, *ApJ*, **729**, 124
- Davies, R. D., Elliott, K. H., & Meaburn, J. 1976, *MNRAS*, **81**, 89
- Davies, R. I., Agudo Berbel, A., Wiezorrek, E., et al. 2013, *A&A*, **558**, A56
- Dickens, J. E., Langer, W. D., & Velusamy, T. 2001, *ApJ*, **558**, 693
- Dufour, R. J. 1975, *ApJ*, **195**, 315
- Dufour, R. J. 1984, in IAU Symp. 108, Structure and Evolution of the Magellanic Clouds, ed. S. van den Bergh & K. S. D. de Boer (Dordrecht: Reidel), 353
- Dunne, B. C., Points, S. D., & Chu, Y.-H. 2001, *ApJS*, **136**, 119
- Ehrenfreund, P., & Charnley, S. B. 2000, *ARA&A*, **38**, 427
- Ellingsen, S. P. 2006, *ApJ*, **638**, 241
- Ellingsen, S. P., Breen, S. L., Caswell, J. L., Quinn, L. J., & Fuller, G. A. 2010, *MNRAS*, **404**, 779
- Ellingsen, S. P., Whiteoak, J. B., Norris, R. P., Caswell, J. L., & Vaile, R. A. 1994, *MNRAS*, **269**, 1019
- Epchtein, N., Braz, M. A., & Sevre, F. 1984, *A&A*, **140**, 67
- Fernández-Martín, A., Pérez-Montero, E., Vilchez, J. M., & Mampaso, A. 2017, *A&A*, **597**, A84
- Filipovic, M. D., Jones, P. A., White, G. L., & Haynes, R. F. 1998, *A&AS*, **130**, 441
- Fujimoto, M., & Noguchi, M. 1990, *PASJ*, **42**, 505
- Fukui, Y., Kawamura, A., Minamidani, T., et al. 2008, *ApJS*, **178**, 56
- Fukui, Y., Mizuno, N., Yamaguchi, R., et al. 1999, *PASJ*, **51**, 745
- Fukui, Y., Tokuda, K., Saigo, K., et al. 2019, *ApJ*, **886**, 14
- Fukui, Y., Tsuge, K., Sano, H., et al. 2017, *PASJ*, **69**, L5
- Galliano, F., Galametz, M., & Jones, A. P. 2018, *ARA&A*, **56**, 673
- Galliano, F., Hony, S., Bernard, J.-P., et al. 2011, *A&A*, **536**, A88
- Garay, G., & Lizano, S. 1999, *PASP*, **111**, 1049
- Gardner, F. F., & Whiteoak, J. B. 1985, *MNRAS*, **215**, 103
- Gerakines, P. A., Schutte, W. A., Greenberg, J. M., & van Dishoeck, E. F. 1995, *A&A*, **296**, 810
- Gerner, T., Beuther, H., Semenov, D., et al. 2014, *A&A*, **563**, A97
- Goldsmith, P. F., & Langer, W. D. 1978, *ApJ*, **222**, 881
- Goldsmith, P. F., & Langer, W. D. 1999, *ApJ*, **517**, 209
- Gordon, K. D., Roman-Duval, J., Bot, C., et al. 2014, *ApJ*, **797**, 85
- Green, J. A., Caswell, J. L., Fuller, G. A., et al. 2008, *MNRAS*, **385**, 948
- Gruendl, R. A., & Chu, Y. 2009, *ApJS*, **184**, 172
- Gusdorf, A., Cabrit, S., Flower, D. R., & Pineau Des Forêts, G. 2008, *A&A*, **482**, 809
- Harju, J., Pineda, J. E., Vasyunin, A. I., et al. 2020, *ApJ*, **895**, 101
- Haynes, R. F., & Caswell, J. L. 1981, *MNRAS*, **197**, 23P
- Heikkilä, A., Johansson, L. E. B., & Olofsson, H. 1997, *A&A*, **319**, L21
- Helmich, F. P., & van Dishoeck, E. F. 1997, *A&AS*, **124**, 205
- Henize, K. G. 1956, *ApJS*, **2**, 315
- Herbst, E., & van Dishoeck, E. F. 2009, *ARA&A*, **47**, 427
- HERITAGE Team 2013, Herschel Inventory of the Agents of Galaxy Evolution (IPAC), <https://catcopy.ipac.caltech.edu/doi/doi.php?id=IRSA76/IRSA76>
- Hildebrand, R. H. 1983, *QJRAS*, **24**, 267
- Imai, H., Katayama, Y., Ellingsen, S. P., & Hagiwara, Y. 2013, *MNRAS*, **432**, L16
- Indebetouw, R., Johnson, K. E., & Conti, P. 2004, *AJ*, **128**, 2206
- Israel, F. P., Johansson, L. E. B., Lequeux, J., et al. 1993, *A&A*, **276**, 25
- Jones, O. C., Woods, P. M., Kemper, F., et al. 2017, *MNRAS*, **470**, 3250
- Jørgensen, J. K., Belloche, A., & Garrod, R. T. 2020, *ARA&A*, **58**, 727
- Kauffmann, J., Bertoldi, F., Bourke, T. L., Evans, N. J., I., & Lee, C. W. 2008, *A&A*, **487**, 993
- Kaufman, M. J., Hollenbach, D. J., & Tielens, A. G. G. M. 1998, *ApJ*, **497**, 276
- Knödseder, J. 2013, Cosmic Rays in Star-Forming Environments (Cham: Springer), 169
- Koornneef, J. 1984, in IAU Symp. 108, Structure and Evolution of the Magellanic Clouds, ed. S. van den Bergh & K. S. D. de Boer (Dordrecht: Reidel), 333
- Kurtz, S. 2002, in ASP Conf Ser. 267, Hot Star Workshop III: The Earliest Phases of Massive Star Birth, ed. P. Crowther (San Francisco, CA: ASP), 81
- Kurtz, S. 2005, in IAU Symp. 227, Massive Star Birth: A Crossroads of Astrophysics, ed. R. Cesaroni et al. (Cambridge: Cambridge Univ. Press), 111
- Kurtz, S., Cesaroni, R., Churchwell, E., Hofner, P., & Walmsley, C. M. 2000, Protostars and Planets IV (Tucson, AZ: Univ. Arizona Press.), 299
- Lazendic, J. S., Whiteoak, J. B., Klammer, I., Harbison, P. D., & Kuiper, T. B. H. 2002, *MNRAS*, **331**, 969
- Leger, A., Jura, M., & Omont, A. 1985, *A&A*, **144**, 147
- López-Sepulcre, A., Balucani, N., Ceccarelli, C., et al. 2019, *ESC*, **3**, 2122
- López-Sepulcre, A., Jaber, A. A., Mendoza, E., et al. 2015, *MNRAS*, **449**, 2438
- Luck, R. E., Moffett, T. J., Barnes, Thomas G., I., & Gieren, W. P. 1998, *AJ*, **115**, 605
- Lucke, P. B., & Hodge, P. W. 1970, *AJ*, **75**, 171
- Luks, T., & Rohlfs, K. 1992, *A&A*, **263**, 41
- Madau, P., & Dickinson, M. 2014, *ARA&A*, **52**, 415
- Maeder, A., Grebel, E. K., & Mermilliod, J.-C. 1999, *A&A*, **346**, 459
- Marcelino, N., Gerin, M., Cernicharo, J., et al. 2018, *A&A*, **620**, A80
- Markwick, A. J., Chamley, S. B., & Millar, T. J. 2001, *A&A*, **376**, 1054
- Martín, S., Mauersberger, R., Martín-Pintado, J., Henkel, C., & García-Burillo, S. 2006, *ApJS*, **164**, 450
- Martín-Doménech, R., Muñoz Caro, G. M., & Cruz-Díaz, G. A. 2016, *A&A*, **589**, A107
- Mathis, J. S., Rumpl, W., & Nordsieck, K. H. 1977, *ApJ*, **217**, 425
- McGee, R. X., Brooks, J. W., & Batchelor, R. A. 1972, *AuJPh*, **25**, 581
- McMullin, J. P., Waters, B., Schiebel, D., Young, W., & Golap, K. 2007, in ASP Conf. Ser. 376, Astronomical Data Analysis Software and Systems XVI, ed. R. A. Shaw, F. Hill, & D. J. Bell (San Francisco, CA: ASP), 127
- Mehlert, D., Noll, S., Appenzeller, I., et al. 2002, *A&A*, **393**, 809
- Meixner, M., Gordon, K. D., Indebetouw, R., et al. 2006, *AJ*, **132**, 2268
- Meixner, M., Panuzzo, P., Roman-Duval, J., et al. 2013, *AJ*, **146**, 62
- Mendoza, E., Lefloch, B., López-Sepulcre, A., et al. 2014, *MNRAS*, **445**, 151
- Mininni, C., Fontani, F., Sánchez-Monge, A., et al. 2021, *A&A*, **653**, A87
- Minissale, M., Moudens, A., Baouche, S., Chaabouni, H., & Dulieu, F. 2016, *MNRAS*, **458**, 2953
- Miura, H., Yamamoto, T., Nomura, H., et al. 2017, *ApJ*, **839**, 47
- Möller, T., Endres, C., & Schilke, P. 2017, *A&A*, **598**, A7
- Moorejja, B., Casper, E., Mundy, L. G., & Looney, L. W. 2007, *ApJ*, **659**, 447
- Müller, H. S. P., Schlöder, F., Stutzki, J., & Winnewisser, G. 2005, *JMoSt*, **742**, 215
- Müller, H. S. P., Thorwirth, S., Roth, D. A., & Winnewisser, G. 2001, *A&A*, **370**, L49
- Muller, S., Roueff, E., Black, J. H., et al. 2020, *A&A*, **637**, A7
- Mumma, M. J., & Charnley, S. B. 2011, *ARA&A*, **49**, 471
- Newville, M., Stensitzki, T., Allen, D. B., & Ingargiola, A. 2014, LMFIT: Non-Linear Least-Square Minimization and Curve-Fitting for Python, v0.8.0, Zenodo, doi:10.5281/zenodo.11813
- Nishimura, Y., Shimonishi, T., Watanabe, Y., et al. 2016, *ApJ*, **818**, 161
- Noble, J. A., Theule, P., Congiu, E., et al. 2015, *A&A*, **576**, A91
- Nummelin, A., Bergman, P., Hjalmarsen, Å., et al. 2000, *ApJS*, **128**, 213
- Oberg, K. I. 2016, *ChRv*, **116**, 9631
- Öberg, K. I., & Bergin, E. A. 2021, *PhR*, **893**, 1
- Oliveira, J. M., van Loon, J. T., Chen, C.-H. R., et al. 2009, *ApJ*, **707**, 1269
- Oliveira, J. M., van Loon, J. T., Sewilo, M., et al. 2019, *MNRAS*, **490**, 3909
- Oliveira, J. M., van Loon, J. T., Sloan, G. C., et al. 2011, *MNRAS*, **411**, L36
- Oliveira, J. M., van Loon, J. T., Sloan, G. C., et al. 2013, *MNRAS*, **428**, 3001
- Oliveira, J. M., van Loon, J. T., Stanimirović, S., & Zijlstra, A. A. 2006, *MNRAS*, **372**, 1509
- Ossenkopf, V., & Henning, T. 1994, *A&A*, **291**, 943
- Pagel, B. E. J. 2003, in ASP Conf. Ser. 304, CNO in the Universe, ed. C. Charbonnel, D. Schaerer, & G. Meynet (San Francisco, CA: ASP), 187
- Palau, A., Fuente, A., Girart, J. M., et al. 2011, *ApJL*, **743**, L32
- Pauly, T., & Garrod, R. T. 2018, *ApJ*, **854**, 13
- Pei, Y. C., Fall, S. M., & Hauser, M. G. 1999, *ApJ*, **522**, 604
- Pennock, C. M., van Loon, J. T., Filipović, M. D., et al. 2021, *MNRAS*, **506**, 3540
- Penteado, E. M., Walsh, C., & Cuppen, H. M. 2017, *ApJ*, **844**, 71
- Pickett, H. M., Poynter, R. L., Cohen, E. A., et al. 1998, *JQSR*, **60**, 883
- Pietrzyński, G., Graczyk, D., Gieren, W., et al. 2013, *Natur*, **495**, 76
- Quénard, D., Jiménez-Serra, I., Viti, S., Holdship, J., & Coutens, A. 2018, *MNRAS*, **474**, 2796
- Rémy-Ruyer, A., Madden, S. C., Galliano, F., et al. 2014, *A&A*, **563**, A31
- Rémy-Ruyer, A., Madden, S. C., Galliano, F., et al. 2015, *A&A*, **582**, A121
- Robitaille, T., & Bressert, E. 2012, APLpy: Astronomical Plotting Library in Python, Astrophysics Source Code Library, ascl:1208.017
- Robitaille, T. P., Whitney, B. A., Indebetouw, R., Wood, K., & Denzmore, P. 2006, *ApJS*, **167**, 256
- Rolleston, W. R. J., Trundle, C., & Dufton, P. L. 2002, *A&A*, **396**, 53
- Roman-Duval, J., Gordon, K. D., Meixner, M., et al. 2014, *ApJ*, **797**, 86
- Russell, S. C., & Dopita, M. A. 1992, *ApJ*, **384**, 508

- SAGE Team 2006, Surveying the Agents of a Galaxy's Evolution (IPAC), <https://catcopy.ipac.caltech.edu/doi/doi.php?id=IRSA76/IRSA404>
- Scalise, E. J., & Braz, M. A. 1982, *AJ*, **87**, 528
- Schilke, P., Walmsley, C. M., Pineau des Forets, G., & Flower, D. R. 1997, *A&A*, **321**, 293
- Schwarz, K. R., Ott, J., Meier, D., & Claussen, M. 2012, AAS Meeting, **219**, 341.04
- Seale, J. P., Looney, L. W., Chen, C. H. R., Chu, Y.-H., & Gruendl, R. A. 2011, *ApJ*, **727**, 36
- Seale, J. P., Looney, L. W., Chu, Y.-H., et al. 2009, *ApJ*, **699**, 150
- Seale, J. P., Looney, L. W., Wong, T., et al. 2012, *ApJ*, **751**, 42
- Seale, J. P., Meixner, M., Sewilo, M., et al. 2014, *AJ*, **148**, 124
- Sewilo, M., Charnley, S. B., Schilke, P., et al. 2019, *ESC*, **3**, 2088
- Sewilo, M., Churchwell, E., Kurtz, S., Goss, W. M., & Hofner, P. 2004, *ApJ*, **605**, 285
- Sewilo, M., Indebetouw, R., Carlson, L. R., et al. 2010, *A&A*, **518**, L73
- Sewilo, M., Indebetouw, R., Charnley, S. B., et al. 2018, *ApJL*, **853**, L19
- Sharples, R., Bender, R., Agudo Berbel, A., et al. 2013, *Msngr*, **151**, 21
- Shimonishi, T., Dartois, E., Onaka, T., & Boulanger, F. 2016a, *A&A*, **585**, A107
- Shimonishi, T., Das, A., Sakai, N., et al. 2020, *ApJ*, **891**, 164
- Shimonishi, T., Izumi, N., Furuya, K., & Yasui, C. 2021, *ApJ*, **922**, 206
- Shimonishi, T., Onaka, T., Kato, D., et al. 2008, *ApJL*, **686**, L99
- Shimonishi, T., Onaka, T., Kawamura, A., & Aikawa, Y. 2016b, *ApJ*, **827**, 72
- Shirley, Y. L., Evans, N. J., II, Rawlings, J. M. C., & Gregersen, E. M. 2000, *ApJS*, **131**, 249
- Sinclair, M. W., Carrad, G. J., Caswell, J. L., Norris, R. P., & Whiteoak, J. B. 1992, *MNRAS*, **256**, 33P
- Skouteris, D., Vazart, F., Ceccarelli, C., et al. 2017, *MNRAS*, **468**, L1
- Smith, R. C. & MCELS Team 1998, *PASA*, **15**, 163
- Soma, T., Sakai, N., Watanabe, Y., & Yamamoto, S. 2018, *ApJ*, **854**, 116
- Sutton, E. C., Peng, R., Danchi, W. C., et al. 1995, *ApJS*, **97**, 455
- Taquet, V., Wirstrom, E. S., & Charnley, S. B. 2016, *ApJ*, **821**, 46
- Taquet, V., Wirstrom, E. S., Charnley, S. B., et al. 2017, *A&A*, **607**, A20
- Tokuda, K., Fukui, Y., Harada, R., et al. 2019, *ApJ*, **886**, 15
- Tsuge, K., Sano, H., Tachihara, K., et al. 2019, *ApJ*, **871**, 44
- Turner, B. E. 1991, *ApJS*, **76**, 617
- Vallenari, A., Aparicio, A., Fagotto, F., et al. 1994, *A&A*, **284**, 447
- van Dishoeck, E. F. 2014, *FaDi*, **168**, 9
- van Dishoeck, E. F. 2018, in IAU Symp 332, Astrochemistry VII: Through the Cosmos from Galaxies to Planets, ed. M. Cunningham et al. (Cambridge: Cambridge Univ. Press), 3
- van Dishoeck, E. F., Jansen, D. J., Schilke, P., & Phillips, T. G. 1993, *ApJL*, **416**, L83
- van Gelder, M. L., Kaper, L., Japelj, J., et al. 2020, *A&A*, **636**, A54
- van Loon, J. T., Oliveira, J. M., Gordon, K. D., Sloan, G. C., & Engelbracht, C. W. 2010, *AJ*, **139**, 1553
- Vastel, C., Ceccarelli, C., Lefloch, B., & Bachiller, R. 2014, *ApJL*, **795**, L2
- Wakelam, V., Dartois, E., Chabot, M., et al. 2021, *A&A*, **652**, A63
- Wang, M., Chin, Y.-N., Henkel, C., Whiteoak, J. B., & Cunningham, M. 2009, *ApJ*, **690**, 580
- Ward, J. L., Oliveira, J. M., van Loon, J. T., & Sewilo, M. 2016, *MNRAS*, **455**, 2345
- Ward, J. L., Oliveira, J. M., van Loon, J. T., & Sewilo, M. 2017, *MNRAS*, **464**, 1512
- Welty, D. E., Federman, S. R., Gredel, R., Thorburn, J. A., & Lambert, D. L. 2006, *ApJS*, **165**, 138
- Westerlund, B. E. 1997, The Magellanic Clouds (Cambridge: Cambridge Univ. Press), 292
- Whiteoak, J. B., & Gardner, F. F. 1986, *MNRAS*, **222**, 513
- Whiteoak, J. B., Wellington, K. J., Jauncey, D. L., et al. 1983, *MNRAS*, **205**, 275
- Whitney, B. A., Sewilo, M., Indebetouw, R., et al. 2008, *AJ*, **136**, 18
- Wirstrom, E. S., Charnley, S. B., Persson, C. M., et al. 2014, *ApJL*, **788**, L32
- Wong, T., Hughes, A., Ott, J., et al. 2011, *ApJS*, **197**, 16
- Yamaguchi, T., Takano, S., Watanabe, Y., et al. 2012, *PASJ*, **64**, 105
- Yang, A. Y., Thompson, M. A., Tian, W. W., et al. 2019, *MNRAS*, **482**, 2681
- Yang, A. Y., Urquhart, J. S., Thompson, M. A., et al. 2021, *A&A*, **645**, A110
- Yozin, C., & Bekki, K. 2014, *MNRAS*, **443**, 522
- Zubko, V., Dwek, E., & Arendt, R. G. 2004, *ApJS*, **152**, 211